ALL-OPTICAL WAVEFORM RECOGNITION AND ITS APPLICATIONS IN ULTRASHORT PULSE OPTICAL CDMA SYSTEMS

A Thesis

Submitted to the Faculty

of

Purdue University

by

Zheng Zheng

In Partial Fulfillment of the

Requirements for the Degree

of

Doctor of Philosophy

December 2000

To My Family.

ACKNOWLEDGMENTS

Every time I look back at my past five years at Purdue, I realize how far I had gone beyond whom I was and what a rewarding period of time I had gone through. I should thank Prof. Weiner, without whose encouragement and guidance I would have never been able to go so far. I am also so grateful to everyone, Dan, Chang, Yongqian ..., who was or is a member of our group. What is so valuable to me is not only their direct help to me but their efforts to make our group a nice place to work in. Their excellent work always encouraged and challenged me to be a better person. My experience at Purdue wouldn't be such a memorable one without my friends here, like Jianan Yang and many more, who made a small Midwest town no longer a lonely place for me. After all, I am most deeply indebted to my parents for their immense love and support, which I will never be able to repay in my life. Though they are thousands of miles away, in my heart, we had never been apart.

TABLE OF CONTENTS

Page

LIST OF TABLES vii

LIST OF FIGURES ix

ABSTRACT xiii

1 INTRODUCTION 1

1.1 Optical CDMA 1

1.2 Ultrashort Pulse Coherent CDMA Systems 4

2 Ultrafast Two-Photon Absorption Optical Thresholders 11

2.1 Optical Thresholding for Optical CDMA 11

2.2 Two-Photon Absorption 13

2.3 Theoretical Treatment 14

2.4 Experiment with Unchirped Bandwidth Limited Pulses 15

2.5 Experiments with Chirped and Spectrally Coded Pulses 19

2.6 Conclusions 23

3 Theory of Second Harmonic Generation in Thick Crystals for Ultrashort Pulses 37

3.1 Derivation of the coupled SHG wave equations 39

3.2 SHG equations under small signal conditions 42

3.2.1 Thin nonlinear crystals and broadband SHG 43

3.2.2 Thick nonlinear crystals and narrowband SHG 44

3.3 CDMA Correlation and Coding Scheme 46

4 Experimental Studies of Spectral Code Correlator Based on SHG in Thick Crystals 51

4.1 Quasi-Phase Matching and PPLN 51

4.2 Experimental Setup 53

4.3 Generation of Spectrally Coded Pulses 55

4.4 Experimental Results Using Bulk PPLN Samples 58
4.5 Experimental Results Using PPLN SHG Waveguides 60
4.6 Summary 62
5 SHG of Femtosecond Pulses in Thick Crystal under Large Conversion Efficiency Conditions 79
5.1 Experimental Studies 81
5.2 Theoretical and Numerical Studies 93
6 Summary 111
LIST OF REFERENCES 113
VITA 121

LIST OF TABLES

Table Page

5.1 Simulation Parameters. 103

LIST OF FIGURES

Figure		Page
1.1	Illustration of various multi-access schemes.	2
1.2	Block diagram of an optical CDMA system.	4
1.3	Diagram of an ultrashort-pulse optical CDMA system.	6
2.1	Scheme of optical thresholding in a ultrashort pulse CDMA system.	12
2.2	Scheme of two-photon absorption thresholding experiment with unchirped pulses.	17
2.3	TPA GaAs waveguide.	25
2.4	Intensity dependence of TPA photocurrent of GaAs waveguide.	26
2.5	Pulsewidth dependence of TPA photocurrent.	27
2.6	Measured electrical impulse response of the waveguide on sampling oscilloscope.	28
2.7	Scheme of two-photon absorption thresholding experiments with coded pulses.	29
2.8	Pulsewidth dependence of TPA photocurrent for chirped pulses.	30
2.9	Cross-correlation traces for unchirped and chirped pulses.	31
2.10	Measured TPA photocurrent compared to theoretical estimation.	32
2.11	Cross-correlation traces for uncoded pulses and pulses coded with a pseudorandom sequence.	33
2.12	Cross-correlation traces for pulses coded with the pseudorandom sequence given in the caption of Fig. 2.11 and cyclic shift no. 8 of the code, respectively.	34
2.13	Contrast ratio of TPA photocurrent and theoretical estimation based on pulse shape measurement for coded pulses.	35
3.1	SHG of short optical pulses in thin and thick nonlinear crystals.	45
3.2	Scheme of spectral phase coding for SHG spectral correlators.	47

3.3 Scheme of optical CDMA system using SHG spectral correlators. . . . 48

4.1 Scheme of PPLN SHG experimental setup. 63

4.2 Pulse shape variation due to different state of polarization in the fiber laser. 64

4.3 Spectrum of the output from the fiber laser used in the PPLN SHG studies. 65

4.4 Gain equalization of the pump spectrum. 66

4.5 The mapping of the spectral phase coding function to the spatial modulation function of LCM. 67

4.6 Experimental intensity cross-correlation data of spectrally uncoded and coded pulses. 68

4.7 Theoretical intensity profiles and experimental intensity cross-correlation data of pulses spectrally coded with Hadamard codes. 69

4.8 Experimental intensity cross-correlation data of pulses spectrally coded with length-7 M-sequence codes. 70

4.9 Experimental intensity cross-correlation data of pulses spectrally coded with length-15 M-sequence codes. 71

4.10 SHG spectra measured under different spectral phase coding situations with C_1 and C_2 chosen from length-8 Hadamard codes. 72

4.11 SHG spectra measured under different spectral phase coding situations with C_1 and C_2 chosen from length-7 M-seq codes. 73

4.12 The influence of residual second order spectral phase distortion on the SHG spectra measured under different spectral phase coding situations. 74

4.13 Internal SHG conversion efficiency vs. internal input pump pulse energy. 75

4.14 SHG spectra of PPLN waveguides measured under different spectral phase coding situations. 76

4.15 SHG signals measured by a photodetector under different spectral phase coding situations. 77

5.1 Scheme of proposed add-drop multiplexer for CDMA systems. 81

5.2 SHG efficiency vs. pump pulse energy. 83

5.3 Comparison of different SHG saturation curves. 85

5.4 Pump spectrum variation as the pump power increases. 86

5.5 Output pump spectrum under high power conditions, as the center wavelength is varied. 88

5.6 Output pump spectrum under high power conditions, as the center wavelength is varied. The phase matching wavelength is different from that in Fig. 5.5. 89

5.7 Pump pulse temporal shape when it is not phase matched for SHG. . 90

5.8 Pump pulse temporal shape when it is phase matched for SHG. . . . 91

5.9 Spectral phase curve of the pump under the phasematched and large input condition. 92

5.10 SH spectrum shape under low pump conditions. 94

5.11 SH spectrum shape under different input pump powers. 95

5.12 Simulated and experimental SH spectrum under low input power. . . 99

5.13 Simulated SH conversion efficiency vs. input pump power, considering the effects of different physical processes. 100

5.14 Simulated pump spectrum under 10pJ input power, considering an effective varying phase mismatch. 101

5.15 Simulated pump pulse shape under 10pJ input power, considering only an effective varying phase mismatch. 102

5.16 Simulated pump spectrum under 10pJ input power, considering an effective varying phase mismatch and an effective 'NPM' term. 104

5.17 Simulated pump pulse shape under 10pJ input power, considering an effective varying phase mismatch and an effective 'NPM' term. 105

5.18 Simulated pump spectrum under large input condition and varied phase-matching conditions. 107

5.19 The simulated evolution of the pump pulse shape under 10pJ input power, considering an effective varying phase mismatch and an effective 'NPM' term. 108

ABSTRACT

Zheng, Zheng. Ph.D., Purdue University, December, 2000. All-optical waveform recognition and its applications in ultrashort pulse optical CDMA systems. Major Professor: Andrew M. Weiner.

The progress of high-speed optical communication systems will soon require signal processing capabilities beyond the limit of the electronic devices within the system. An inevitable solution to this problem is the development of all-optical signal processing technologies.

This thesis presents the detailed studies of two nonlinear optical signal processing devices for a proposed ultrashort pulse optical code-division multi-access (CDMA) system. In such a system, recognizing different short optical waveforms is required to de-multiplex different channels and is also a research challenge to be solved. We first studied a two-photon absorption waveguide nonlinear photodetector and demonstrated the pulseshape dependence of the photocurrents using various sub-picosecond optical pulses. This scheme has the advantages in terms of compactness and easiness to use. We later developed an optical spectral correlation scheme based on second harmonic generation in long nonlinear crystals. By using periodically-poled lithium niobate and waveguide structures, we realized $\sim$ 30 dB contrast ratio and sub-pJ operating power which are significant improvements over other prior schemes studied. We also first proposed a modified coding scheme for the CDMA system that would be compatible with the novel detection schemes we studied.

1. INTRODUCTION

After the successful development and deployment of high-speed long-haul optical fiber communication systems in the past two decades, which utilize the large bandwidth of optical fibers, fiber communication systems are increasingly important as a solution of providing high-bandwidth connections in the local access networks (LAN) and metropolitan area networks, where a large number of subscribers within a relatively small area require, from time to time, to communicate with others in the network at the rates of Gbit/s to tens of Gbit/s. Unlike the situation in the wide area networks (WAN), the data flow in LANs could be more bursty and the control of the network more complex. One important requirement of the potential LAN technologies is to allow the users to have easy access to the network and effectively share the bandwidth with others.

1.1 Optical CDMA

Various multi-access schemes have been studied to handle the problem of multiple users sharing a common transmission system. The three most common multi-access schemes are time-division multiplexing (TDM), wavelength-division multiplexing (WDM) and code-division multiple access (CDMA). As illustrated in Fig. 1.1, in TDM systems, different channels are separated into different time slots. Higher capacity is realized by shortening the length of each time slot, and thus synchronization between different users becomes more challenging. In WDM systems, each user is assigned a specific non-overlapping wavelength slot within the network bandwidth. To increase the number of channels in the system, narrower bandwidth slots could be required, which would put further restrictions on the performance of the laser sources and other optical components used. An alternative of TDM and WDM is CDMA,

where the transmitted data from different users overlap in both time and frequency domain, and what separates them from each other is a new dimension: code.

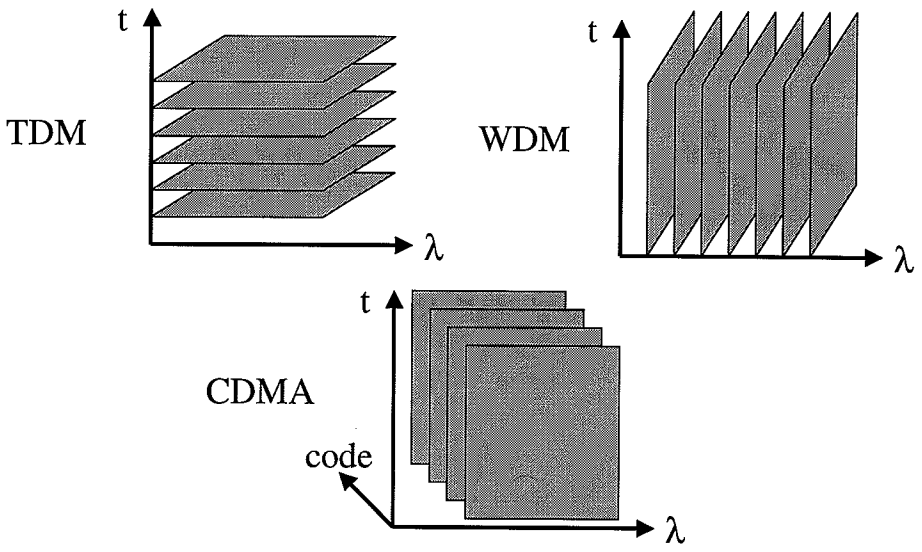

Fig. 1.1. Illustration of various multi-access schemes.

CDMA technology have realized significant success in the area of radio frequency (RF) wireless communications where a large number of users randomly connect to the network. By taking advantage of the electrical signal processing technologies that are able to cope with the relatively slow bit rates and realize strong suppression of the channel noise, high bandwidth efficiency and improved channel capacity can be realized in a noisy, narrowband channel.

To extend this idea into optical communication area, in an optical CDMA system, unique signature codes (could be temporal, spectral or even spatial codes (for free space communications instead of fiber communications) [1]) are assigned to the

corresponding optical transmitter/receiver pairs, which are used to label every data bit sent between them, so that the coded data stream can only be recognized by the correct user in the network. In such a network (as shown in Fig. 1.2, in each transmitter, a unique device called encoder uses a code to modulate every bit sent out, while, on the receiver side, before the normal detection process, the input signals from different transmitters first go through a decoder and a matched filtering device that is to compare the input coded signals with the code known to the receiver. The ideal result should be that only the input signal that is coded with a code matched to the receiver's code is allowed to pass through and then detected, while all other signals coded with unmatched codes are filtered out and suppressed. Under the more realistic situations, if the matched filtering process is not able to completely reject other signals, the concurrence of more than one active user in the network at the same time would generate multi-access interference (MAI). Unlike other communication systems, CDMA systems are interference limited systems, e. g. the effective suppression of MAI is the key to realize high system performance.

Optical CDMA, which allows asynchronous transmission and realizes some networking functionalities, like routing and addressing, at a lower physical level, could have advantages in realizing simpler and more flexible network management. It may promise better capability to handle burst traffic, as there is no hard limit on the number of users in the network. Also, since there is no need to reserve either frequency or time slots for all potential users of the network and additional users can be accommodated into the network by assigning additional codes to them, higher bandwidth efficiency may be possible. Introducing more users into the network is realized at the expense of additional interference to other users so that potentially degraded, but still acceptable, performance may be experienced by the others. Various optical CDMA schemes had been proposed and studied in the past decade [2, 3, 4, 5, 6, 7]. Different schemes can be categorized based on the light source used (laser [3, 5, 6] or incoherent light source [4]), the coding schemes (temporal [6], spectral amplitude [4] or spectral phase coding [3, 5]) and the detection schemes.

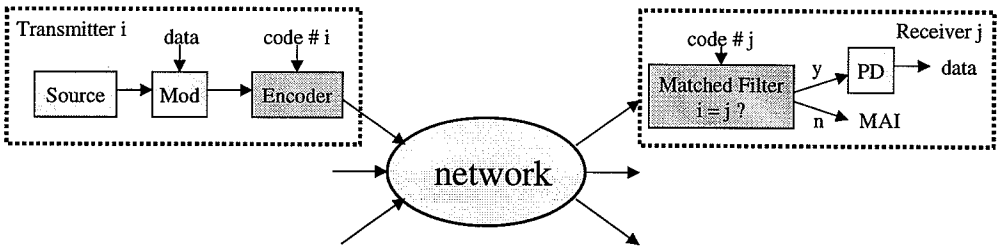

Fig. 1.2. Block diagram of an optical CDMA system.

However, while TDM and WDM had realized commercial success (especially WDM in the past few years), optical CDMA had not been able to realize the popularity of their RF CDMA counterparts, partly because of, along with many other things, the lack of the appropriate, practical high-speed optical signal processing technologies at the high bit rates required to compete with other technologies.

1.2 Ultrashort Pulse Coherent CDMA Systems

A kind of coherent optical CDMA system based on spectral phase coding/decoding of ultrashort optical pulses was first proposed in the early 90's [3]. In such a CDMA system [3, 8], as shown in Fig. 1.3, the light sources used are modelocked lasers, and multiplexing is be achieved by assigning different, minimally interfering spectral phase

codes to different transmitter-receiver pairs. At the transmitter, a spectral phase is applied to the spectrum of ultrashort optical pulses from the modelocked laser by the encoder, which stretches the ultrashort pulse into a tens of picosecond duration waveform in the temporal domain. A common fiber link connects all the users, and optical signals from the transmitters in the network are combined and sent through the dispersion compensated fiber links to the receivers. A receiver must be able to detect the data bits coded with a known code to the receiver, while rejecting others as unwanted multiple-access interference. Code recognition could be accomplished by (as seen in Fig. 1.3) first applying another spectral phase code known to the receiver to all the incoming signals by the decoder. Then a nonlinear optical device, which have the capability to recognize the different optical waveforms by giving vastly different outputs to different inputs coded with matched or unmatched codes, should be used before the optical signals are converted into data.

The ultrashort pulse CDMA system is one kind of coherent CDMA systems where the encoding and decoding of optical signals are based on the manipulation of optical fields (instead of intensities) of coherent laser sources. Because of the laser source required for such a system and other technical issues related to ultrashort pulses, the realization of such a system could be more technically challenging and costly. However, at the expense of greater complexity and costs, compared to other optical CDMA schemes, it may have a greater potential to realize higher system performance [3]. Since the coding is done in the spectral domain, it inherently doesn't need any synchronization in the encoding/decoding process, and could be significantly easier to scale into higher data rate system. In contrast to other spectral amplitude coding schemes, the coherent coding scheme could give us greater capability to suppress the MAI and reach higher performance, provided that the related optical signal processing devices are available.

The key technologies required in such a CDMA system are ultrashort pulse lasers, dispersion compensated fiber links, optical spectral encoder-decoders and nonlinear optical detection devices.

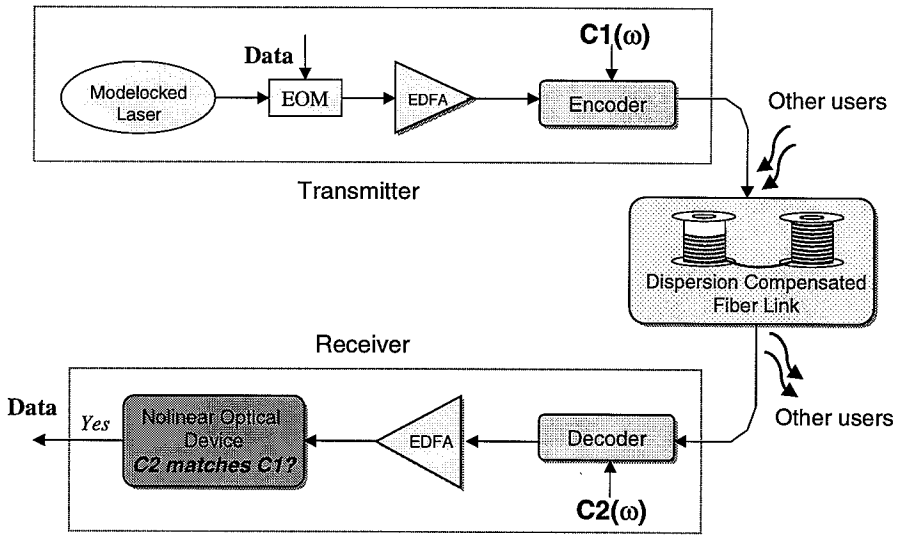

Fig. 1.3. Diagram of an ultrashort-pulse optical CDMA system.

In the past decade, the development of ultrashort laser sources not only results in the generation of pulses of just several femtoseconds in duration [9] but the availability of compact and reliable femtosecond lasers at communication wavelength. Amongst these lasers, diode-pumped solid-state lasers had been commercially available, and research work [10, 11] had led to systems with sizes and power requirements close to those in the communication applications. On the other hand, fiber lasers also emerge as another kind of compact ultrashort laser sources and offer inherent compatibility with other fiber optic technologies.

Because spectral phase codes are used in the encoding-decoding process, under the assumption that the transmission power is low enough that the process can be considered linear, chromatic dispersion in optical fiber would be the main cause to destroy the code information, if not carefully controlled. Transmission of 0.98 ps pulses over 40 km fiber had been demonstrated in 1996 [12] by using dispersion compensating fiber (DCF) [13, 14]. Nearly dispersion free transmission of 250-fs pulses over a 2.5 km fiber link and, more recently, 400-fs pulses over 10 km fiber link had been demonstrated using a combination of DCF fiber and a pulse shaper [15, 16]. Most recently nearly chirp-free transmission of 250 fs pulses over 139 km has been demonstrated in a scheme involving synchronous modulation [17].

Encoding and decoding of ultrashort pulses had been demonstrated first at visible wavelength in [18] using free-space pulse shapers. Recently programmable fiber-pigtailed pulse shapers at 1.55 μm had been demonstrated by our colleagues and it also had a loss low enough for system experiments [8, 19]. More recently, the spectral encoders based on integrated fiber optic components, like arrayed waveguide gratings (AWG) [20], fiber Bragg gratings [21, 5, 22] and the combination of synchronous temporal modulation and fiber Bragg gratings [23], are demonstrated.

As mentioned above, one of the main challenges and possible advantages of the optical CDMA system is to develop and implement novel optical signal processing components to realize optical waveform recognition at a range of parameters that are well beyond the capability of current electronic technology. The envisioned CDMA

system would be able to accommodate tens of users and each user would be able to transmit data at a speed up to several Gbit/s. The requirements of the optical signal processing devices are: The device should be able to recognize different short optical waveforms in real time based on the spectral phase coding of the pulses. It should be able to suppress the MAI with a large contrast and enable efficient detection of the intended signal. The overall operating speed of the device must be compatible with the targeted data rate per channel. Their operating power level should also be limited to the level that can be provided by current optical fiber amplifier technology. It should also enable asynchronous operations. The nonlinear optical signal processing devices naturally satisfy this requirement, unlike other schemes [6].

An ultrafast optical thresholder based on nonlinear frequency shifts in fibers had been demonstrated by a former colleague of our group [24]. The nonlinear fiber optic thresholder realized a >10% efficiency and a 30 dB contrast ratio (often defined as the ratio of the thresholder's response to correctly decoded signals to the response to the interference noise, which gives the ability of the optical thresholders to reject unwanted noise) at the power level of tens of pJ per pulse. Based on the above technologies, an optical CDMA subsystem testbed had been built and femtosecond spectral phase encoding and decoding with two fiber pigtailed pulse shapers connected through a fiber link had been successfully demonstrated [8, 19].

One potential limitation of the fiber thresholder is the high operation power requirement which is still hard to meet for current fiber communication systems. This prompts further studies into other types of nonlinear optic devices, which is the topic of this thesis.

Here, two kinds of optical signal processing devices are studied. The first is an optical thresholder based on two-photon absorption (TPA) in semiconductor photodetectors, which could have the advantages in terms of simplicity of use, small response latency, compactness and stability compared to the nonlinear fiber devices which are hundreds of meters in length. The second is a spectral phase correlator based on second harmonic generation (SHG) in long nonlinear crystals which had shown $\sim$ 30

dB contrast ratio and a potential operating power level as low as 0.1 pJ.

In the following chapters, the studies on the TPA thresholders are covered in Chapter 2.

Chapter 3-5 are about the SHG detection scheme.

Chapter 3 discusses the theoretical models of SHG process in long nonlinear crystal and presents the proposed SHG spectral phase correlation scheme and the related new CDMA coding scheme.

Chapter 4 describes the experimental studies of SHG process pumped by spectral coded pulses whose results show the potential of the spectral correlator.

Chapter 5 gives experimental studies and numerical simulation results of SHG process under large depletion conditions. The potential factors limiting the SH conversion efficiency under high powers are studied. These results have implications for the realization of a proposed optical CDMA add-drop multiplexer.

A brief conclusion is given in Chapter 6.

It should also be noted that some of the above technologies used in ultrashort pulse CDMA systems have applications also outside of this area. For example, the dispersion compensation techniques are also widely needed in the high-speed WDM systems. The spectral encoders could also find applications in WDM systems as dispersion compensators [25, 26]. All-optical signal processing techniques could potentially be used for pattern matching applications in other broadband optical networks, like the header recognition process in ultrafast TDMA networks [27, 28, 29].

2. ULTRAFAST TWO-PHOTON ABSORPTION OPTICAL THRESHOLDERS

2.1 Optical Thresholding for Optical CDMA

In the ultrashort pulse CDMA scheme proposed in [3], the spectral phase code used at the transmitter is to scramble the unchirped, high peak intensity optical pulses into low intensity pseudonoise. As shown in Fig. 2.1, the corresponding receiver applies a code that is the conjugate of the code applied by the encoder. The decoding process cancels out the previous code, and the long waveform is re-compressed into a femtosecond pulse which is considered correctly decoded. For other signals coded with different codes, the outputs of the decoder are still coded with pseudorandom codes and their temporal shapes stay as long pseudonoise bursts (but with the comparable energy per pulse).

Therefore, in such a system, the difference between the properly and improperly decoded signals lies in their different pulsewidth and peak intensity. An optical thresholder is needed to distinguish between the two kinds of signals based on the contrast in their peak power (or temporal pulse width) instead of their average power. When the input is the incorrectly decoded multi-access interference noise, the output of the optical thresholder should be negligible compared to the output for the correctly decoded signals. The ratio of the two kind of responses defines the ability of the thresholder to suppress the MAI.

Here we propose to realize optical thresholding based on two-photon absorption photoconductivity in semiconductor photodetectors. We studied the response of the TPA waveguide detector to optical excitation pulses of different shapes and demonstrate the potential MAI suppression ratio for this kind of devices. The electrical

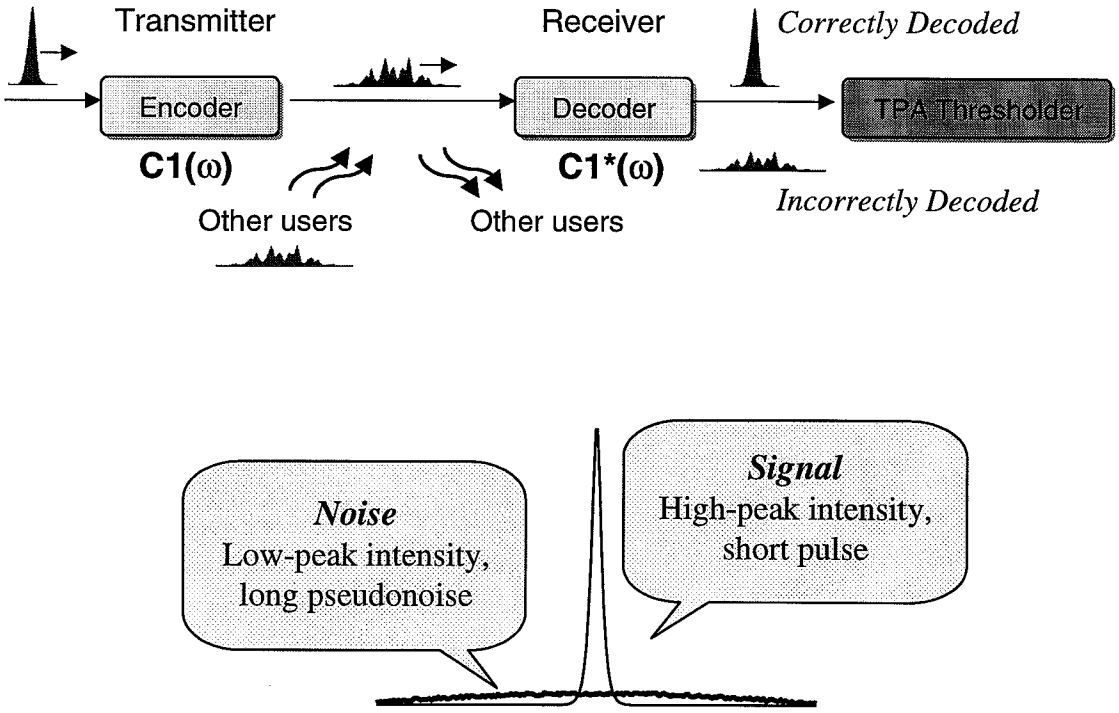

Fig. 2.1. Scheme of optical thresholding in a ultrashort pulse CDMA system.

response time of this optoelectronic device is also studied which verified the potential of the device to operate at a speed as high as $\sim$ 1 Gbit/s.

2.2 Two-Photon Absorption

In semiconductors, TPA is a nonresonant, third order nonlinear optical phenomenon in which two photons are absorbed simultaneously to generate a single electron-hole pair [30, 31, 32]. For photons with energies below the bandgap, TPA effect becomes significant when the excitation optical intensity is high, like in waveguide structures and/or when ultrashort optical pulses are used. It was considered as deleterious and one of the chief factors in limiting all-optical switching in semiconductor waveguides [33] and leading to break-up of spatial solitons in glass waveguides [34]. On the other hand, TPA has drawn interest for ultrashort optical pulse measurement as a substitute quadratic nonlinear process in place of the widely used second-harmonic generation in phase-matched nonlinear crystals. The nonlinear photoconductivity associated with TPA has been applied for autocorrelation measurements of ultrashort pulses [35, 36, 37, 38, 39, 40, 41, 42, 43]. Various devices have been used in these experiments, including GaAs/AlGaAs and InGaAsP waveguides [36, 37, 38], photodiodes [39], light-emitting diodes [40] and laser diodes [43].

TPA techniques have some advantages over their SHG counterparts, such as:

- TPA has a broader wavelength response(e. g. photon energy can vary from above half of the bandgap to close to the bandgap), while phase-matching conditions pose a much narrower response bandwidth on the SHG process [44], which will be further discussed in the next few chapters. Therefore a TPA correlator is well suited for very short optical pulses (for example, a few femtoseconds long). Also it can potentially be used at wavelengths where a suitable SHG material is hard to find, like at ultraviolet wavelengths [42];

- the nonlinear optical process and electrical detection process are integrated in these TPA devices, which makes these devices inherently compact and easy to use in optoelectronic systems;

- though the TPA process has a lower efficiency compared to the SHG, this disadvantage could be partially offset by using waveguide devices. Since there are less restrictions on the interaction length as those due to the phase matching bandwidth for SHG processes, long TPA waveguide devices can be used. The smaller mode size and the increased interaction length can increase the efficiency and lead to lower power requirements.

Because of the nonlinear dependence of the TPA effect on the excitation optical intensity, it is expected that the yield of the TPA process could be different for optical pulses with different peak intensity but similar average powers, based on which we approximate the optical thresholding function described above. Here we comprehensively investigate the dependence of TPA-induced photocurrent in GaAs waveguides on optical pulse shape. I first discuss the mathematical model we used to describe the TPA photoconductivity, and the experimental studies using bandwidth limited pulses, chirped and spectrally coded pulses in the subpicosecond region are discussed in Sec. 2.4 and 2.5. While our results confirm the feasibility of using these devices as ultrafast optical thresholders, the pros and cons of this scheme are discussed at the end of this chapter.

2.3 Theoretical Treatment

The simple model we used to describe the variation of the carrier density N (in the unit of cm^{-3}) in a waveguide is given by the rate equation [36]:

$$\frac{dN}{dt} = \frac{\alpha}{h\nu} I + \frac{\beta}{2h\nu} I^2 \tag{2.1}$$

where I is the intensity of the beam, β is the two-photon absorption coefficient, α is the one-photon absorption coefficient and $h\nu$ is the photon energy. When the absorption is relatively weak (as the case in our experiments), we can assume that the light remains undepleted so that I and N stay nearly uniform throughout the waveguide. Thus the average photocurrent i_{ave} can be found by integrating over the rate equation,

$$i_{ave} = \frac{e\Omega}{T}\int_{-\frac{T}{2}}^{\frac{T}{2}} \frac{dN}{dt}\,dt = \frac{e\Omega}{T}\int_{-\frac{T}{2}}^{\frac{T}{2}} (\frac{\alpha}{h\nu}I + \frac{\beta}{2h\nu}I^2)\,dt \tag{2.2}$$

where T is the period of the modelocked pulse stream and Ω is the volume in which carriers are generated. If we also assume the pulses have a Gaussian shape:

$$I(t) = I_{ave}\sqrt{\frac{2}{\pi}}\frac{T}{\tau}\exp\frac{-2t^2}{\tau^2} \tag{2.3}$$

where I_{ave} is the average intensity, τ is the half width at e^{-2} pulsewidth parameter. The average photocurrent in this case is given by:

$$i_{ave} = e\Omega(\frac{\alpha}{h\nu}I_{ave} + \frac{\beta T}{2\sqrt{\pi}h\nu\tau}(I_{ave})^2) \tag{2.4}$$

when T is much larger than τ.

When two-photon absorption is the dominant effect and linear absorption is negligible, TPA photocurrent is expected to vary quadratically as the input average power changes, which is a characteristic for TPA vs. other kinds of absorptions. Eq. (2.4) shows that the current linearly depends on the inverse pulsewidth ($1/\tau$) when the pulses have similar simple pulse shapes. For more complicated wavefunctions, as those we will discuss in later chapters, the current can be calculated directly from the integration Eq. (2.2), when the pulse shape is known. Thus, two pulses with equal energies but very different pulsewidths (hence different peak intensities) should generate different TPA photocurrents. A good contrast in photocurrent as a function of peak intensity would be what we look for to approximate the desired ultrafast thresholding function.

2.4 Experiment with Unchirped Bandwidth Limited Pulses

The experimental setup [45] is shown in Fig. 2.2. Our experiments used 150 fs pulses at 1.50 μm wavelength and 80 MHz repetition rate from a Spectra Physics femtosecond optical parametric oscillator (OPO) synchronously pumped by a modelocked Ti:Sapphire laser. A polarizer was used to set a horizontal input polarization, and a stepper motor driven variable attenuator wheel was used to adjust the optical

power. For some measurements, a mechanical chopper was used to enable lock-in detection. Light was coupled into a GaAs waveguide by using a 40× microscope objective. The waveguide was reverse biased by a DC power supply connected through a bias tee. A home made metal finger probe was used to provide the electrical contact to the wire-bonded waveguide. A sampling oscilloscope and a lock-in amplifier were connected to the bias tee to measure the photocurrent time response and the average photocurrent, respectively.

The TPA waveguides we used were fabricated by Prof. John H. Marsh's group at University of Glasgow. The MBE-grown GaAs ridge waveguides (see Fig. 2.3) were 1mm long and 3 μm wide and consisted of a p-i-n structure with a 0.6 μm thick GaAs (870nm bandgap) layer sandwiched between $Al_{0.15}Ga_{0.85}As$ layers. The cladding regions were undoped and thick enough to minimize optical mode leakage and free carrier absorption. For photons at >1.5 μm, there was little linear absorption but significant two-photon absorption. The dark current at a typical -5 V bias was about 90 pA, which was negligible for our experiments. The TPA waveguide used here was similar to those used in earlier autocorrelation experiments [36] using 1.06 μm and 1.3 μm pulses tens of picoseconds in duration.

In our experiments, first, the existence of TPA effect was verified by measuring the photocurrent as a function of average optical intensity, for a fixed 150 fs pulsewidth. Shown in Fig. 2.4, the currents clearly showed a quadratic dependence on the optical average power and verified that TPA was the dominant absorption effect in the waveguide.

To adjust the pulse duration for the pulsewidth dependent measurements, the beam was sent through a double-pass pulse shaper. The pulse shaper consisted of a 600 line/mm grating, an achromatic lens(f=190mm) and a planar mirror placed in the focal plane of the lens. With the pulse shaper adjusted to the zero dispersion point and a variable slit placed just before the mirror, this worked as an adjustable pulse stretcher [18]. The slit acted as a spectral window, and its width was adjusted to change the width of spectrum and hence the pulsewidth.

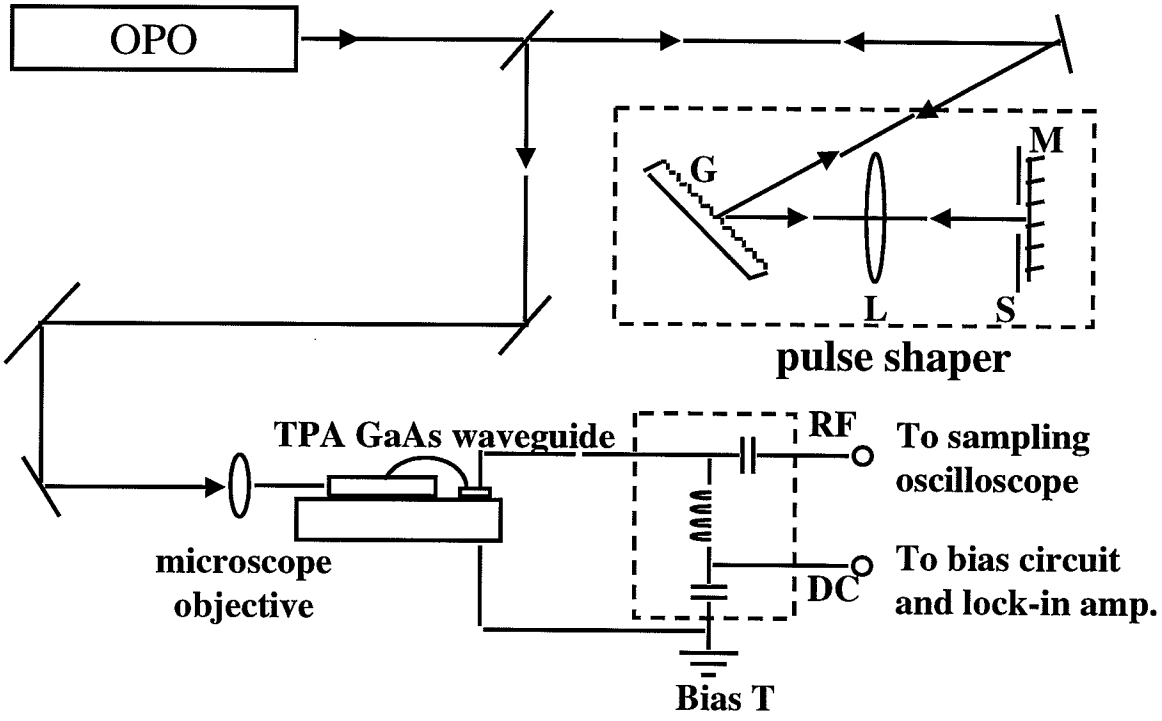

Fig. 2.2. Scheme of two-photon absorption thresholding experiment with unchirped pulses. OPO: Ti:Sapphire laser pumped femtosecond optical parametric oscillator; G: 600 line/mm grating; L: achromatic lens; S: slit; M: flat mirror.

Fig. 2.5 shows data obtained by using the pulsewidth control setup to broaden the pulses over the range from ~180 fs to ~4 ps. The attenuator was adjusted to maintain a constant average optical power of 1.4 mW. The average photocurrent decreases by about twenty times as the pulsewidth increases from ~180 fs to ~4 ps. For each setting of the adjustable slit, the pulsewidth was measured by an autocorrelator. The photocurrent data are well fitted by a τ^{-1} curve in good agreement with the theoretical prediction. There are some small deviations from the fitted curve, which may be caused by changes in the pulseshape itself (not just the pulsewidth) as the slit width is varied. To our knowledge, this was the first experimental verification of the pulsewidth dependence of TPA on a femtosecond time scale [45]. Slightly later Ref [39] also verified the existence of the expected pulsewidth dependence, in contrast to other reports, e.g. in [40], where a different pulsewidth dependence was observed in a different kind of device.

To satisfy the speed requirement of communication applications, it is also required that an optical thresholder has a fast electrical response capable to match the expected high data rate. The electrical response of the waveguide photodetector was measured in the time domain by using a sampling oscilloscope. A high-speed sampling head of the oscilloscope was placed closely after the home made finger probe through the bias tee. The trace obtained using the 80 MHz modelocked pulse train is shown in Fig. 2.6. The current pulse had a FWHM of ~400 ps. The peak voltage response on the 50 Ω oscilloscope was >50 mV at 10 mW average optical input. The results observed already show a sufficiently fast response for applications up to ~1 Gbit/s. The response time could be further reduced by reducing the RC time of the waveguide photodetector itself and/or parasitics associated with our rather crude external contacting scheme.

The conversion efficiency, under current experimental conditions, can be given as $\eta = \frac{i_{ave}}{P_{ave}} =\sim 5.2 P_{ave}/T_{FWHM} f$, where average optical input power P_{ave} is measured before the light being coupled into the waveguide and is in the unit of watts, average TPA current i_{ave} is in amp, input FWHM pulsewidth T_{FWHM} is in ps and the repeti-

tion rate f of the laser source is in MHz. The optical power in the waveguide is hard to measure accurately , and, in our setup, the coupling efficiency could be low and <10%. For example, when the pulsewidth is 150 fs, repetition rate is 80 MHz and input power is 1.5 mW, η is $\sim 6.5 \times 10^{-4}$ A/W. If we assume that a minimum 1 μA photocurrent is required for an error-free detection [46] and the optical pulse width is still 150 fs, at a repetition rate of 1 Gib/s, the input optical power would be more than 140 mW for each channel. Considering a system with $\sim$ 100 users, the overall power requirement is simply too large for any fiber systems. We note that the studies in [38, 43] showed TPA devices with about 2 orders of magnitude higher efficiency than that of ours. Therefore, it is possible to lower the above power requirement to $\sim$ 10 per channel. However, for systems with a high user counts, it could be still a challenge to implement in real systems.

2.5 Experiments with Chirped and Spectrally Coded Pulses

While the above results clearly show a $1/\tau$ dependence of TPA current under the simple situation of unchirped pulses with different bandwidths, to further verify the feasibility of applying these waveguides as optical thresholders in CDMA systems, further studies based on more complicated coded and phase modulated optical pulses have been performed. These measurements have been conducted using a fiber optic system which is a more realistic scenario for the thresholding applications. We have also compared our TPA experiments using complicated pulseshapes with SHG measurements. Our data validate the close correspondence between TPA and SHG.

The experimental setup (see Fig. 2.7) utilized part of a system that had been built as a testbed for a proposed coherent optical CDMA system [8]. A stretched-pulse mode-locked [47] Er-fiber ring laser generated 1.56 μm 65-fs pulses at $\sim$33 MHz. The laser output was passed through an interference bandpass filter, while a small portion of the unfiltered output was used as the reference beam in an SHG cross-correlator for the pulse shape measurement. Spectrally filtered pulses from the laser were amplified by a chirped pulse Er-doped fiber amplifier and then input into a fiber-pigtailed femtosecond pulse shaper. The pulse shaper consisted of a

pair of 1100 lines/mm gratings and achromatic lenses(focal length=19 cm). In pulse shaper, the first grating-lens pair spatially disperses the input optical spectrum onto the focal plane of the first lens, where a spatial modulator can modulate different optical frequency components. The modulated spectrum is then recombined into a single beam by the second grating-lens pair, and the output optical spectrum is the input one multiplied by the spatial modulation function applied to the modulator. Here the pulse shaper was adjusted to the zero-dispersion position and had a 128-element programmable liquid crystal modulator(LCM) array [19, 48] in the Fourier plane. Each pixel of the LCM can be individually programmed and provide gray-scale phase modulation. The angular frequency difference between adjacent pixels is $\sim 1.1 \times 10^{11} rad/s$. After the pulse shaper, the pulses were amplified by a second chirped pulse fiber amplifier to compensate for the loss of the pulse shaper and provide enough power for the TPA thresholder. The optical signal was then delivered to the TPA waveguide through a dispersion compensated fiber link and a fiber polarization controller(PC), which had a total length of ~8m. The light was butt-coupled into the waveguide from single mode fiber. The coupling efficiency is expected to be lower than that obtained by focusing with a lens which in turn resulted in a lower signal level compared with the previous experiments. Because of the existence of polarization dependence of TPA in this kind of waveguide photodetectors [49], the state of polarization of the input beam was adjusted to excite the TE mode in the waveguide by using the PC, in order to maximize TPA signals.

In a first experiment, the LCM was used to apply a quadratic phase function to the spectrum, which in turn chirped and broadened the output pulse in time domain. The quadratic phases applied to the ith pixel of the LCM can be described as

$$\Phi_i = \Phi_{max} \frac{(i-64)^2}{64^2} \tag{2.5}$$

where $i = 1, 2, \cdots, 128$; Φ_{max} is the maximum phase shift applied. For $\Phi_{max} > 2\pi$, the phase function is folded into the range of 0 to 2π by the relation of Φ_i modulo 2π.

For these experiments the optical pulses had pulsewidth of $\sim$ 800-900 fs immediately before being launched into the waveguide when there was only constant phase function applied to the LCM. The pulsewidth is determined most likely due to the gain narrowing effect in the EDFA and the existence of self-phase modulation leading to pulse distortion in the fiber pigtail leading to the TPA waveguide.

By linearly increasing the value of Φ_{max}, we could gradually increase the chirp of the pulses and the pulsewidth. Fig. 2.8 shows the measurements of the TPA photocurrent as the pulses were broadened from $\sim$900 fs to $\sim$2.8 ps under a constant average power of $\sim$4.7mW, where Φ_{max} was increased from 0 to 7.5π . The data show that the output was nearly inversely related to the pulsewidth as measured by SHG autocorrelation for this case of chirped optical pulses. Also shown in Fig. 2.8 is the corresponding normalized variation of peak intensity (at $\tau = 0$) in SHG autocorrelation measurements. We can see a close match between the results by the TPA measurements and by conventional SHG experiments. The high sensitivity to pulsewidth shows the ability of these devices to act as peak intensity dependent detectors even for non-bandwidth limited pulses. As the pulsewidth become larger, it is observed that the current drops slightly faster than the $1/\tau$ curve. Further study on the pulse shape was done by using a cross-correlator, where the 65-fs pulses from the laser were used as reference. It was found that as the chirp introduced in the pulse shaper increased, the pulse shape gradually deviated from the original one and had a large oscillating wings or pedestals, as seen in Fig. 2.9, which could not be reflected in the variation of the FWHM pulsewidths. This could be caused by nonlinear effects in the amplifier and fiber link after the pulse shaper.

Under such conditions, the pulse shape could no longer be described only by its FWHM width. However we can still predict the TPA current based on the cross-correlation measurements. Since the reference pulse was much narrower than signal pulses, we can assume, without introducing much error, that the cross-correlation traces are directly proportional to the signal pulse intensities. From the integration equation (2.2), it is possible to estimate the change in the TPA currents. TPA

current and cross-correlation traces were measured for various values of Φ_{max} ranging from $\Phi_{max} = 0$ to $\Phi_{max} = 15\pi$. With an initial pulsewidth of ~850 fs without spectral phase modulation applied, the pulse could be broadened to a maximum FWHM pulsewidth of ~4.4 ps. The TPA current results and the estimations based on Eq. (2.2) showed very good agreement over a range of ~10 times variation, as shown in Fig. 2.10.

To approximate the situation in CDMA systems, as well as to test the TPA response for considerably more complicated pulse shapes, we also performed experiments in which a pseudorandom M-sequence phase code was applied to the spectrum. This transformed the input pulses into low intensity pseudonoise bursts tens of picoseconds in duration. This corresponds to an encoded or incorrectly decoded signal in a CDMA system [8]. In contrast, when a constant phase is applied, the output is a bandwidth-limited short pulse, corresponding to an uncoded or correctly decoded pulse. Fig. 2.11 shows the SHG cross-correlations of uncoded and encoded pulses, demonstrating the dramatic change in intensity and pulsewidth. We measured the TPA photocurrents for spectra coded according to several different cyclic shifts of a length-63 M-sequence code, each of which corresponds to a new intensity and phase substructure under a similar broad envelope(two examples are shown in Fig. 2.12). As shown in Fig. 2.13, we observed an ~20 times drop in the TPA signal compared with the responses from uncoded pulses at the same average power level for all the shifts we applied. The contrast ratio plotted in Fig. 2.13 is defined as the ratio of the TPA signal obtained using coded input pulses to that obtained with uncoded pulses. There were only small variations from one cyclic shift to another which further validates the use of these devices as nonlinear intensity discriminators. We also estimated the contrast ratios on the basis of Eq. (2.2), using pulse shapes measured by SHG cross-correlation. The result plotted as theoretical contrast ratio in Fig. 2.13 is very close to that obtained in the TPA experiments. The excellent agreement between experimental and theoretical results, even for these extremely complicated pulse shapes, shows even more clearly the close correspondence between the TPA and

SHG experiments.

It should be noted that the overall conversion efficiency we observed in this section is about 20 times lower than that in the previous section. We believe that this is mainly due to two factors: First, the working wavelength is 1.56 instead of 1.50 μm which is further closer to the mid-bandgap, and would reduce the TPA coefficient. Second, more coupling loss could be resulted from the butt coupling setup we used here, and this could have a very significant impact on the overall efficiency because of the quadratic intensity dependence of TPA currents.

2.6 Conclusions

Our results confirm the intensity and pulsewidth dependence of the photocurrent from TPA waveguide photodetectors for ultrashort pulses with strong phase or bandwidth modulations. For both unchirped and chirped pulses, the results match closely both with the theoretical predictions and with the more traditional SHG results. These experiments demonstrate the feasibility of applying TPA devices as nonlinear detectors to retrieve peak intensity and pulsewidth related information at the communications wavelength and at high speeds.

The advantages of the proposed TPA optical thresholder are: they are very simple to use and compact, as the device used is also compatible with other current optoelectronic devices using communication systems, so that they can be relatively easily integrated with other devices. Unlike other thresholding schemes [24], the TPA thresholder would have a much small latency due to its small size.

The disadvantages of this detection scheme are: the maximum contrast ratio would be limited to the code length [3, 50], which may not be sufficient for systems with relative high number of users. This is due to the fact that this scheme is an incoherent detection scheme (e. g. it is intensity dependent instead of field dependent). Also the detection efficiency was rather low, so that the required operating power would be unrealistically high for current fiber systems. Even though by using InP-based TPA devices [38, 43] and improved waveguide structures [51] to increase the waveguide coupling efficiency, when scaled to $\sim$ 1 Gib/s bit rates and tens of user counts, we

still expect a total operating power power level around hundreds of mW.

These observations prompted us to further explore other nonlinear phenomena to realize the optical waveform recognition functionality, which lead to the work in the next few chapters.

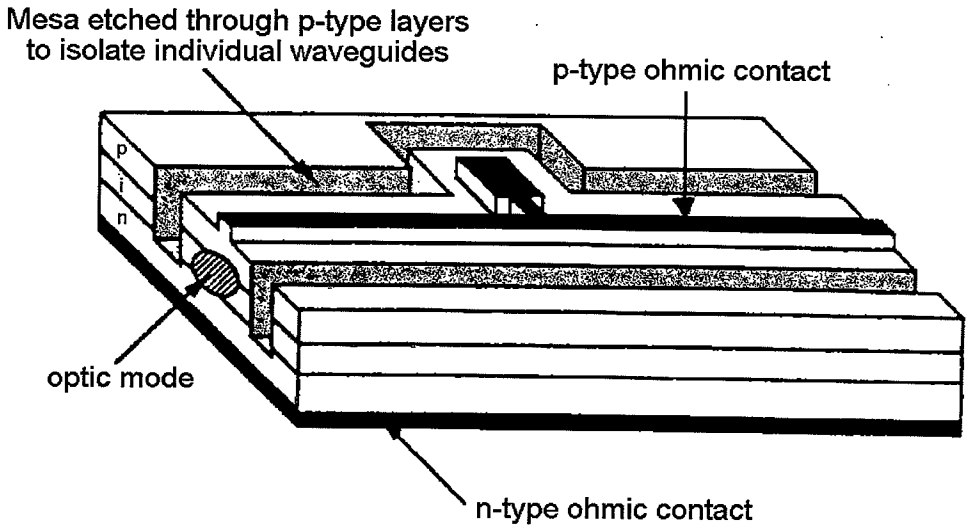

Fig. 2.3. TPA GaAs waveguide.

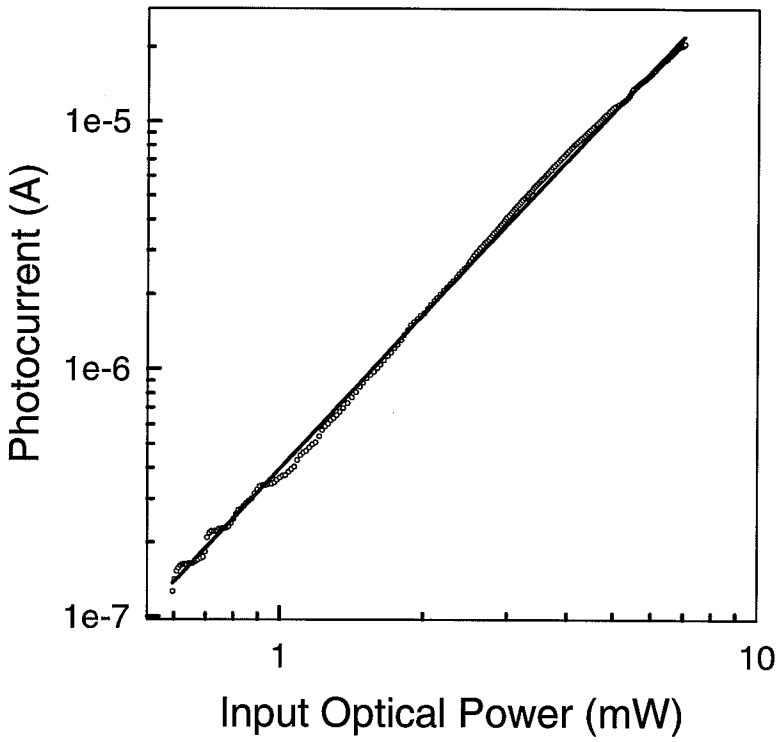

Fig. 2.4. Intensity dependence of TPA photocurrent of GaAs waveguide. o: experimental data for 150 fs OPO. —: straight line fitted to experimental points with a slope of 2.02. The precision in the slope measurement, based on several data sets, is $\sim \pm 0.12$.

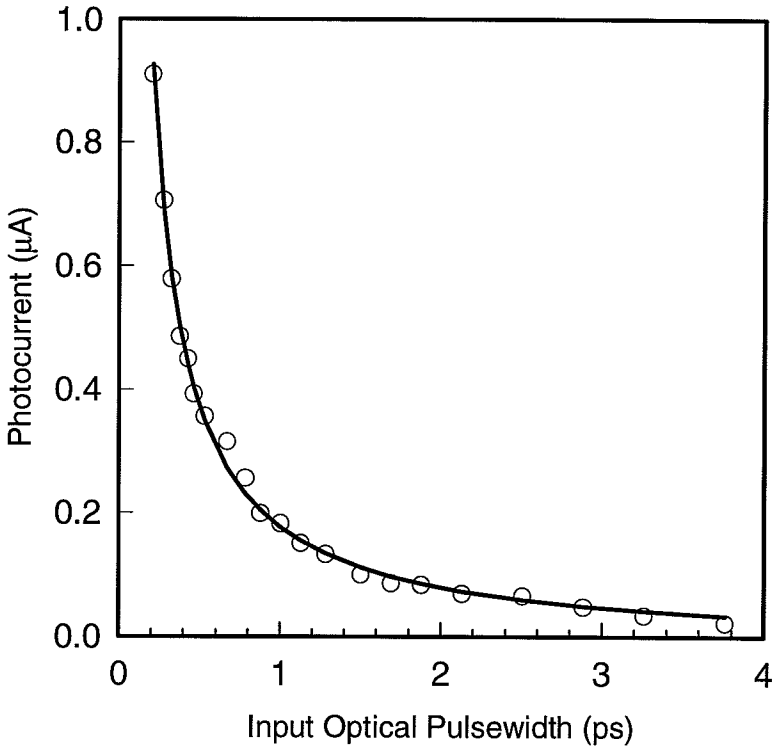

Fig. 2.5. Pulsewidth dependence of TPA photocurrent. ○: experimental data measured for different pulsewidths, with average input power held constant at 1.4 mW. —: $a\tau^{-1}$ curve fitted to the data.

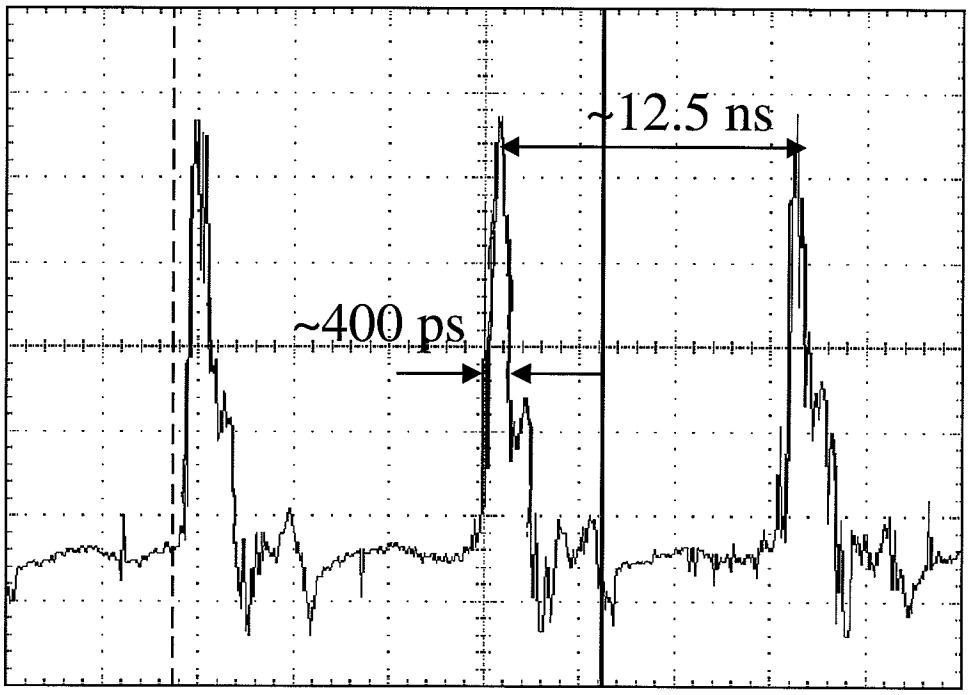

Fig. 2.6. Measured electrical impulse response of the waveguide on sampling oscilloscope. The waveguide was illuminated by 150 fs optical pulses at 80 MHz repetition rate. The FWHM of the electrical pulses is ~400 ps.

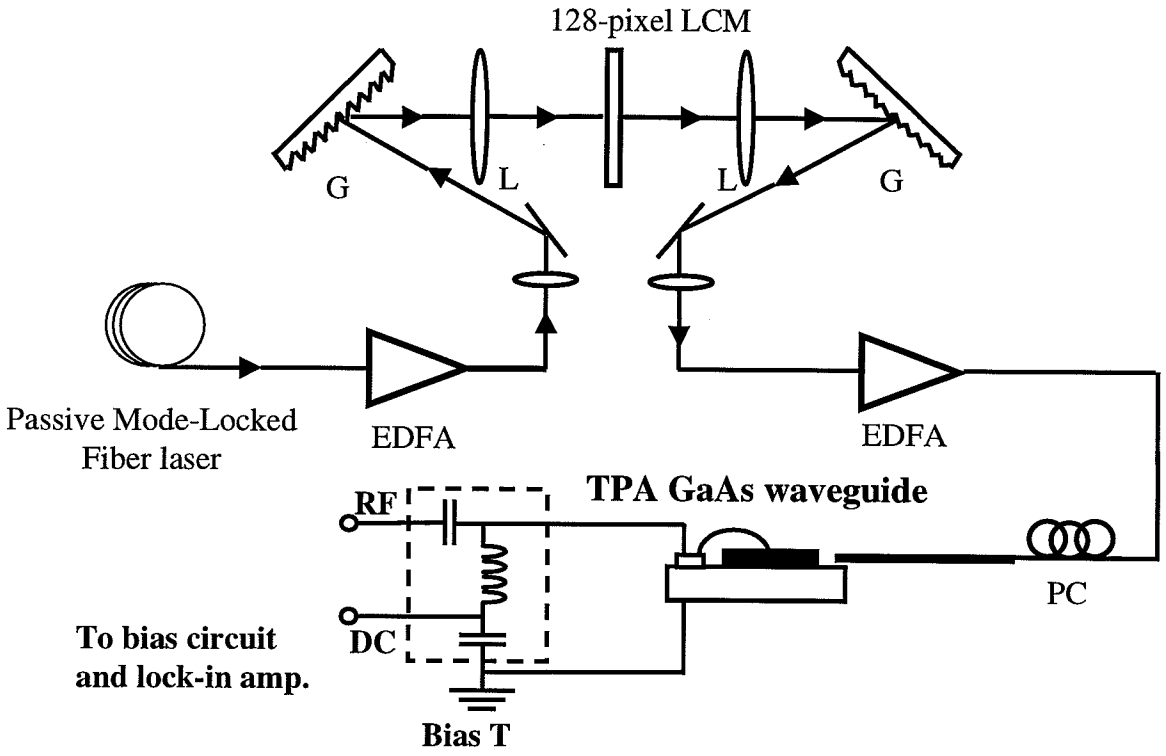

Fig. 2.7. Scheme of two-photon absorption thresholding experiments with coded pulses. G: 1100 line/mm grating; L: achromatic lens; LCM: liquid crystal modulator; EDFA: Er-doped fiber amplifier.

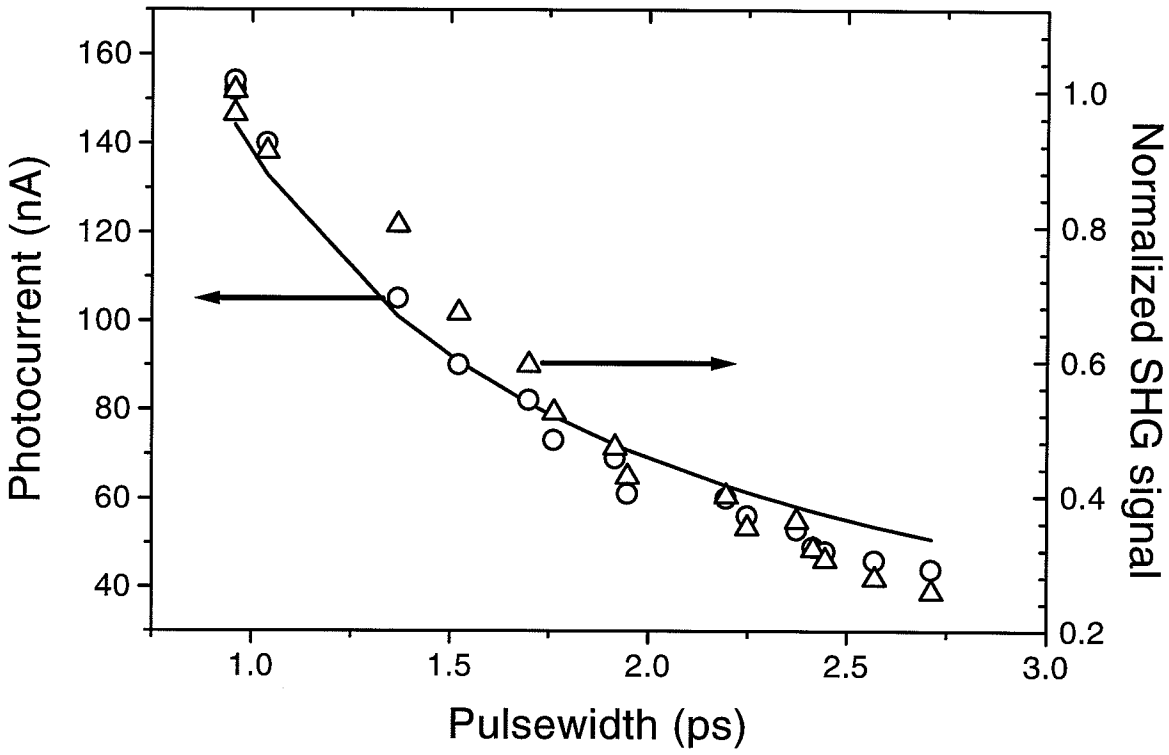

Fig. 2.8. Pulsewidth dependence of TPA photocurrent for chirped pulses. ○: experimental data measured for different pulsewidths, with average input power held constant at 4.7 mW. —: $a\tau^{-1}$ curve fitted to the data. △: normalized SHG autocorrelation intensities at τ=0.

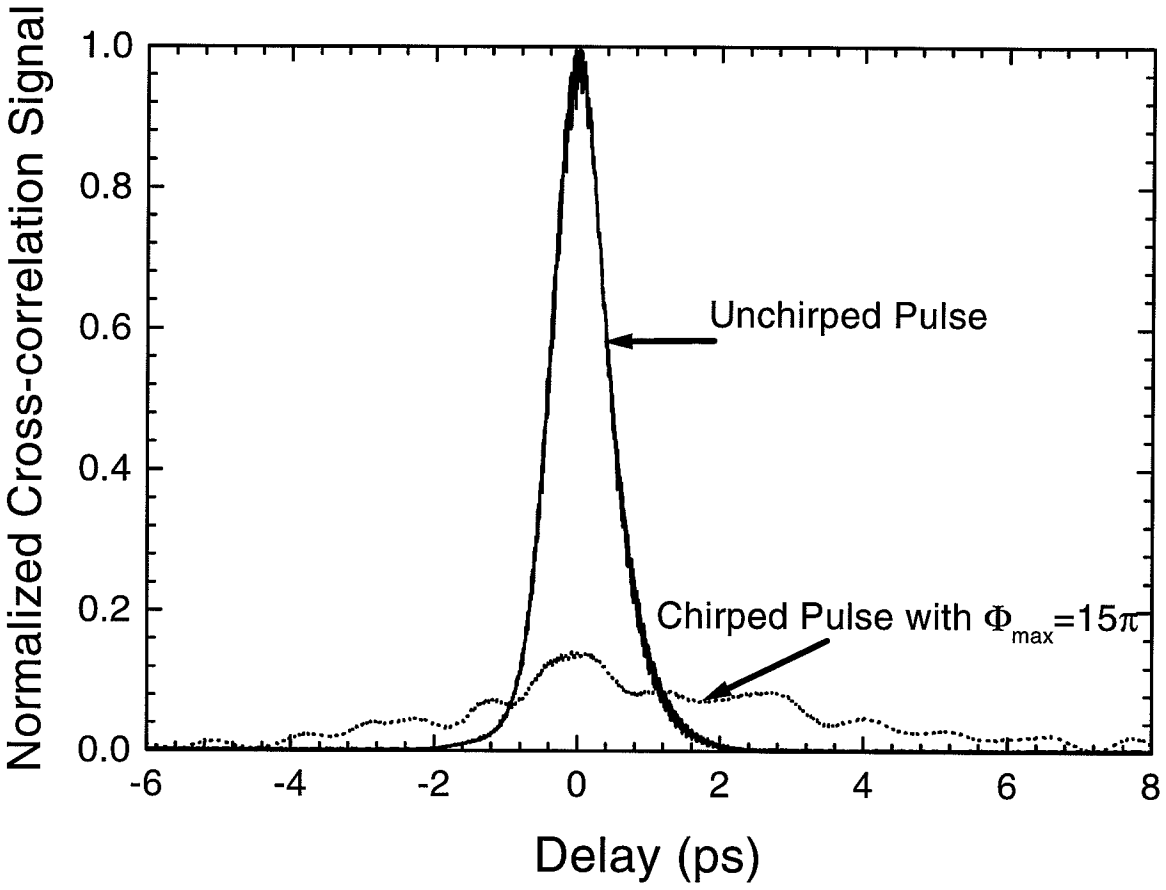

Fig. 2.9. Cross-correlation traces for unchirped and chirped pulses.

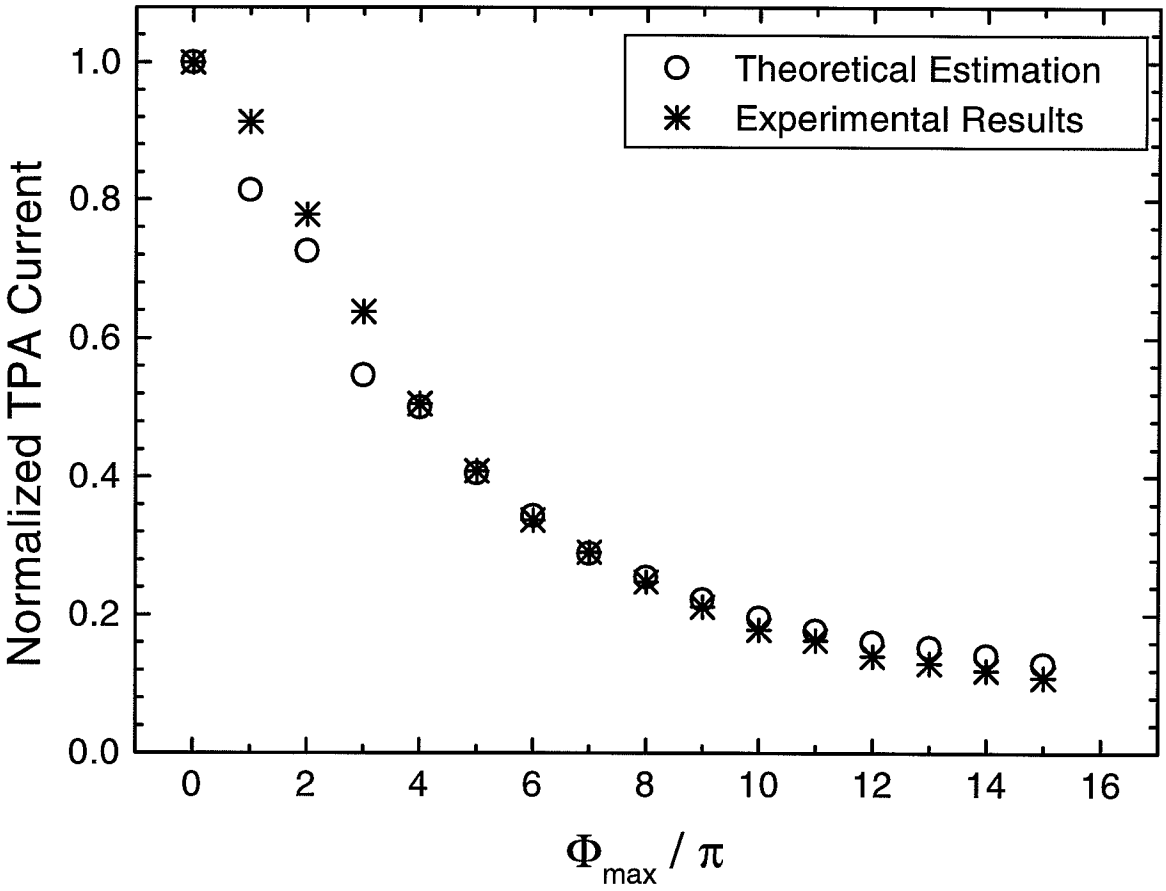

Fig. 2.10. Measured TPA photocurrent compared to theoretical estimation.

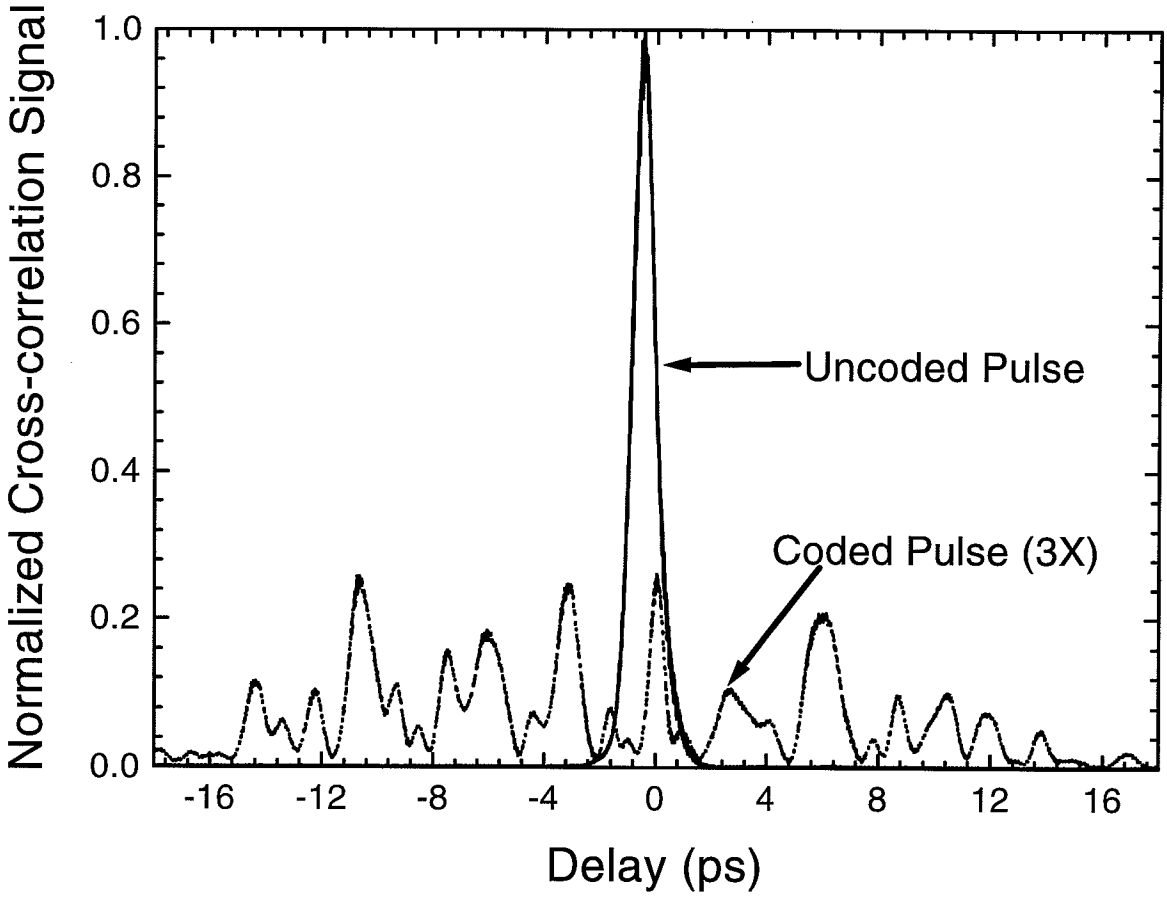

Fig. 2.11. Cross-correlation traces for uncoded pulses and pulses coded with a pseudorandom sequence. The length-63 M-sequence codeword used is [0 0 0 0 0 π π π π π π 0 π 0 π 0 π π 0 0 π π 0 π π π 0 π π 0 π 0 0 π 0 0 π π π 0 0 0 π 0 π π π π 0 0 π 0 π 0 0 0 π π 0 0 0 0 π]

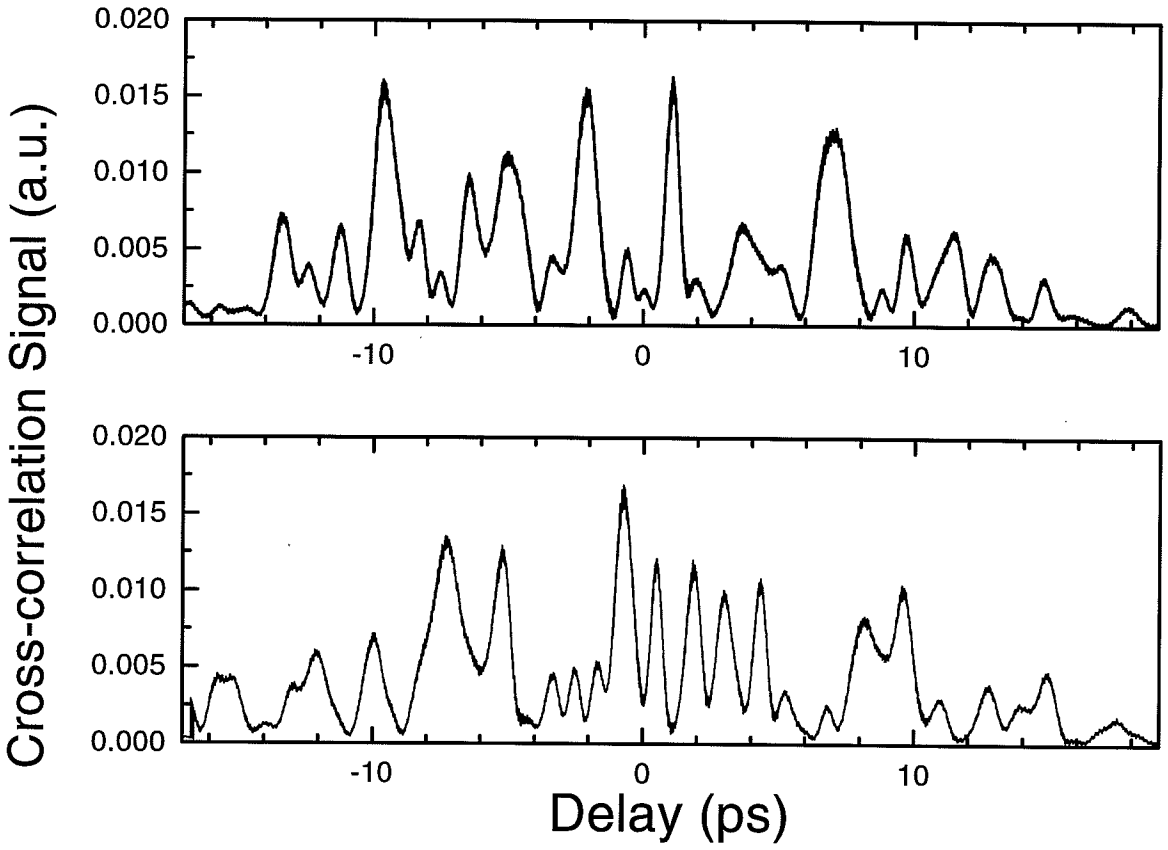

Fig. 2.12. Cross-correlation traces for pulses coded with the pseudorandom sequence given in the caption of Fig. 2.11 and cyclic shift no. 8 of the code, respectively.

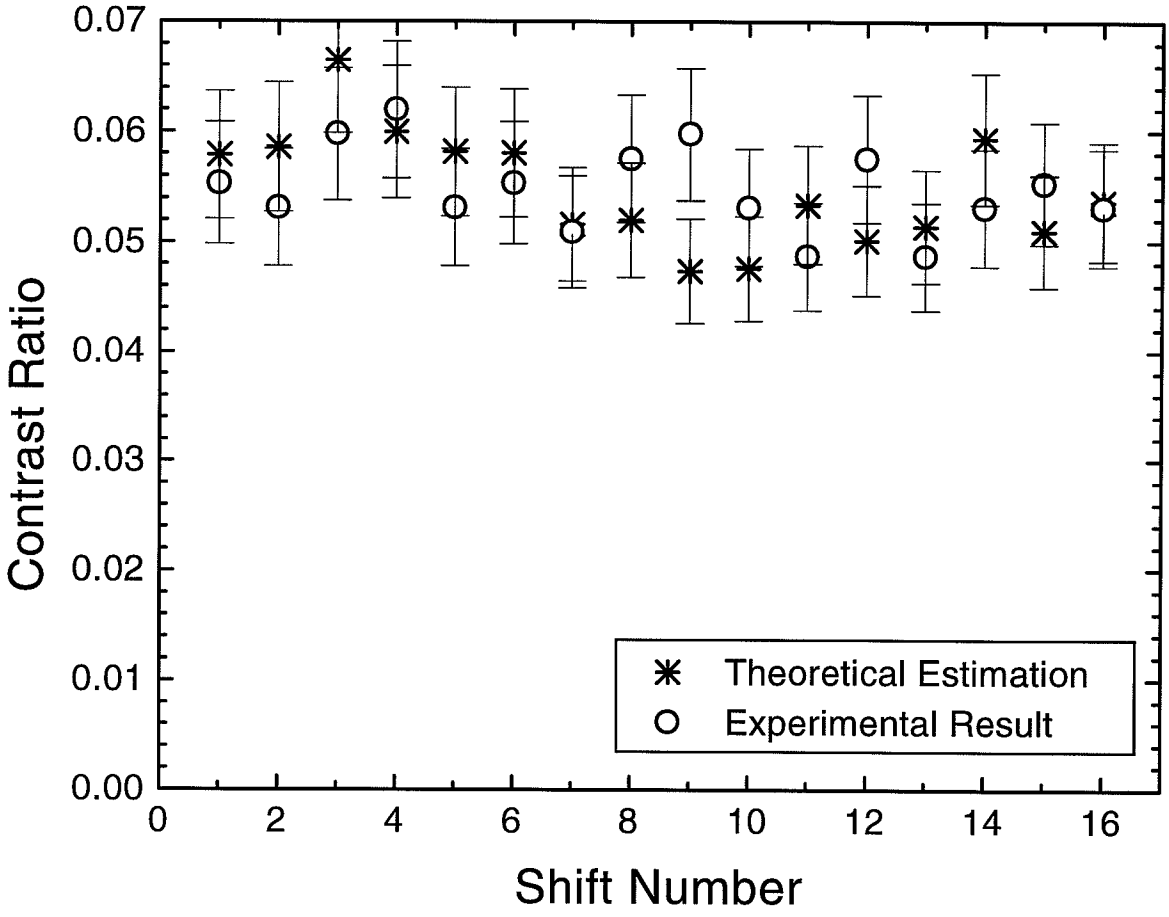

Fig. 2.13. Contrast ratio of TPA photocurrent and theoretical estimation based on pulse shape measurement for coded pulses.

3. THEORY OF SECOND HARMONIC GENERATION IN THICK CRYSTALS FOR ULTRASHORT PULSES

In lieu of the results of the TPA thresholder discussed in the previous chapter, we here propose a nonlinear optical signal process scheme called optical spectral correlator, which, unlike the TPA device, is truly phase sensitive and a real coherent detection scheme. This scheme is based on SHG of ultrashort pulses in thick nonlinear crystals, a parameter range few people had explored before. When a new coding scheme suitable for this detection technique is used, higher MAI suppress and lower operating power requirement could be simultaneously realized.

SHG is one of the oldest nonlinear optical phenomena studied [52, 53, 54, 55], where the pump (fundamental) optical wave of frequency ω propagating in dielectric material is converted to a wave at 2ω due to the nonlinear polarization of the media. Efficient SHG is only possible when the phase velocities of the fundamental and second harmonic (SH) waves are matched so that the generated SH signals can constructively build up in the process. However, because of the existence of phase velocity dispersion, the phase matching condition between the interacting waves is often not met, and the SHG efficiency is severely limited. In order to compensate this phase velocity dispersion, traditionally phase matching techniques based on material birefringence are needed to achieve efficient nonlinear interactions. More recently, quasi-phase-matching (QPM) techniques [56, 57] are under intensive studies, which achieve high SHG conversion efficiency by periodically modulating the material nonlinear coefficient to offset the accumulated material phase mismatch. Periodically poled lithium niobate (PPLN) is our choice of nonlinear material in our studies here, which I will discuss further later.

The situation is more complicated when ultrashort optical pulses are used in the SHG process. Because of the broad bandwidth of the pump light, the SH signals may have broad spectra which can support complex structures. Each SH spectral component results from the coherent addition of different pairs of the frequency components at the fundamental frequency. In addition, the high peak intensity of the excitation pulses enhances the efficiency of the nonlinear frequency conversion process, leading to the possibility of very high efficiency. Because of the high intensity, higher order nonlinearities could also have a significant role and affect the SHG process.

When short pulses are used, the group velocity mismatch (GVM) effect can also affect the SHG spectral bandwidth. In the dispersive medium, since the pump pulse and the SH pulse are at different wavelengths, their group velocities are different. This group velocity mismatch causes the two pulses to gradually walk off from each other in the time domain. When thin nonlinear crystals are used, the walk-off effect is small, so that the two pulses can stay together in the SHG process and a short SH pulse is generated, which has a broad spectrum. On the other hand, for thick crystals, the pump pulse and the generated SH pulse significantly walk off from each other when they propagate through the crystal. Therefore, the generated SH pulse can be much longer than the pump pulse, and its spectrum is narrowed correspondingly.

Theoretical models of SHG process had been well developed since the early age of the studies on SHG [53, 54, 55]. Analytical and numerical studies of SHG of short optical pulses had been done while considering the intrapulse group-velocity dispersion (GVD) effects [58, 59]. However, to my knowledge, no systematic studies (experimental and theoretical) on SHG of femtosecond pulses in long nonlinear crystals under conditions such that both GVD and self phase modulation (SPM) could have a role had been never been done.

Therefore, in this chapter, I first derive a set of coupled nonlinear equations governing the second harmonic generation process which include effects like GVM, GVD and third order nonlinearities. These additional terms could be significant as we will show in later chapters, because of the ultrashort pulses and the high intensity used

(in some of our studies). These equations are formulated in a format that are convenient to be used in Chapter 5 for numerical simulations of SHG process under large depletion conditions.

Under a simpler situation (e. g. there is no depletion, and GVD and SPM are negligible), an analytical description of the SHG output can be given which gives an attractive relation between the pump spectral information and the SHG yield. I would further discuss the implication of this relationship which form the basis of our proposed SHG spectral correlator scheme.

3.1 Derivation of the coupled SHG wave equations

From the well-known Maxwell's equations in a source-free medium:

$$\begin{aligned} \nabla \times \mathbf{E}(\mathbf{r},t) &= -\frac{\partial}{\partial t}\mathbf{B}(\mathbf{r},t) \\ \nabla \times \mathbf{H}(\mathbf{r},t) &= \frac{\partial}{\partial t}\mathbf{D}(\mathbf{r},t) \end{aligned} \tag{3.1}$$

where $\mathbf{E}(\mathbf{r},t)$, $\mathbf{D}(\mathbf{r},t)$, $\mathbf{H}(\mathbf{r},t)$ and $\mathbf{B}(\mathbf{r},t)$ are the electric field, electric displacement, magnetic field and magnetic displacement (induction) vectors, respectively.

For nonmagnetic, but nonlinear dielectric media, we have

$$\begin{aligned} \mathbf{B}(\mathbf{r},t) &= \mu_0 \mathbf{H}(\mathbf{r},t) \\ \mathbf{D}(\mathbf{r},t) &= \epsilon \mathbf{E}(\mathbf{r},t) + \mathbf{P_{NL}}(\mathbf{r},t) \end{aligned} \tag{3.2}$$

where $\mathbf{P_{NL}}(\mathbf{r},t)$ is the electric nonlinear polarization vector and ϵ is the linear permittivity. From Eq. 3.1 and 3.2, and also assuming that the medium is sourceless (e. g. $\nabla \cdot \mathbf{D} = \epsilon \nabla \cdot \mathbf{E} = 0$), we get the nonlinear wave equation:

$$\nabla^2 \mathbf{E}(\mathbf{r},t) - \mu_0 \epsilon \frac{\partial^2}{\partial t^2}\mathbf{E}(\mathbf{r},t) = \mu_0 \frac{\partial^2}{\partial t^2}\mathbf{P_{NL}}(\mathbf{r},t) \tag{3.3}$$

Here we only consider the second and third order nonlinearities, so that $\mathbf{P_{NL}} = \epsilon_0[\chi^{(2)} \cdot \mathbf{EE} + \chi^{(3)} \cdot \mathbf{EEE}]$ Here we limit the discussion to the type-I second harmonic generation situation, and we simplify the optical fields to linearly polarized plane waves colinearly propagating in the z direction, which is appropriate for the SHG in

PPLN. Thus, the above vector equations can be reduced to one-dimensional scalar equations. Also under the plane wave assumption, ∇^2 becomes $\partial^2/\partial z^2$.

Under the slowly varying envelope approximation, we can denote an optical field as:

$$E_i(z,t) = A_i(z,t)\exp[j(\omega_{i,0}t - k_{i,0}z)] \tag{3.4}$$

where A_i is the envelope function of the field, $\omega_{i,0}$ is the center angular frequency of the optical wave and $k_{i,0}$ is the amplitude of the wave vector for the center frequency. This is valid as long as the pulse width is much larger than the optical period, which is true in the scope of this thesis. For the SHG question, the overall field is the summation of the pump field $E_1 = A_1\exp[j(\omega_0 t - k_{1,0}z)]$ and the SH field $E_2 = A_2\exp[j(2\omega_0 t - k_{2,0}z)]$. Therefore, the nonlinear polarization P_{NL} is given by:

$$\begin{aligned} P_{NL} &= \epsilon_0[\chi^{(2)}E_1E_1 + 2\chi^{(2)}E_2E_1^*] \\ &+ 2\epsilon_0[n_0n_2(E_1E_1^* + 2E_2E_2^*)E_1 + n_0n_2(E_2E_2^* + 2E_1E_1^*)E_2] \\ &= P^{(2)}_{NL,2\omega_0} + P^{(2)}_{NL,\omega_0} + P^{(3)}_{NL,\omega_0} + P^{(3)}_{NL,2\omega_0} \end{aligned} \tag{3.5}$$

where we only consider those terms at the angular frequency ω_0 and $2\omega_0$, and those terms represent the effects of SHG (including back conversion) and self-/cross- phase modulations. Here we assume the nonlinear refractive index coefficient $n_2 = \frac{3\chi^{(3)}}{8n_0}$ is approximately the same for both wavelength, as the wavelengths we consider are far from resonance. n_0 is the refractive index (when it is close to the phase matching condition, n_0 is the same for both wavelengths).

By substituting this into Eq. 3.3, we can separate the equation into two coupled equations which consist of terms with the same frequency terms:

$$\begin{aligned} \frac{\partial^2}{\partial z^2}E_1 - \mu_0\epsilon\frac{\partial^2}{\partial t^2}E_1 &= \mu_0\frac{\partial^2}{\partial t^2}(P^{(2)}_{NL,\omega_0} + P^{(3)}_{NL,\omega_0}) \\ \frac{\partial^2}{\partial z^2}E_2 - \mu_0\epsilon\frac{\partial^2}{\partial t^2}E_2 &= \mu_0\frac{\partial^2}{\partial t^2}(P^{(2)}_{NL,2\omega_0} + P^{(3)}_{NL,2\omega_0}) \end{aligned} \tag{3.6}$$

Based on the slowly varying envelope approximation, we also have:

$$\frac{\partial^2}{\partial z^2}E_i(z,t) = (-2jk_{i,0}\frac{\partial A_i}{\partial z} - k_{i,0}^2A_i)\exp[j(\omega_{i,0}t - k_{i,0}z)] \tag{3.7}$$

where the terms of second derivatives of A_i are ignored, as they are much smaller compared to other terms.

Now we take a Fourier transform of the above equations and convert them into the frequency domain. The field in frequency domain is then given by:

$$\tilde{E}(z,\omega) = \widetilde{A_1}(z,\Omega)\exp(-jk_{1,0}z) + \widetilde{A_2}(z,\Omega')\exp(-jk_{2,0}z) \tag{3.8}$$

where $\tilde{E}$ and $\widetilde{A_i}$ are the Fourier transform of E and A_i (i=1,2), respectively, and Ω' and Ω are given by $\omega - 2\omega_0$ and $\omega - \omega_0$, e. g. the detunings of the angular frequencies from the spectral center angular frequencies of the fundamental and SH waves respectively.

Now Eq. 3.6 is also changed into:

$$\begin{aligned} -2jk_{1,0}\frac{\partial\widetilde{A_1}}{\partial z} + (k_1^2(\Omega) - k_{1,0}^2)\widetilde{A_1} &= -\mu_0\omega^2(\tilde{P}^{(2)}_{NL,\omega_0} + \tilde{P}^{(3)}_{NL,\omega_0})\exp(jk_{1,0}z) \\ -2jk_{2,0}\frac{\partial\widetilde{A_2}}{\partial z} + (k_2^2(\Omega') - k_{2,0}^2)\widetilde{A_2} &= -\mu_0\omega^2(\tilde{P}^{(2)}_{NL,2\omega_0} + \tilde{P}^{(3)}_{NL,2\omega_0})\exp(jk_{2,0}z) \end{aligned} \tag{3.9}$$

When the intrapulse third order group velocity dispersion is negligible,

$$\begin{aligned} k_1(\Omega) &= k_{0,1} + \frac{\partial k}{\partial\omega}|_{\lambda=\lambda_1}\Omega + \frac{1}{2}\frac{\partial^2 k}{\partial\omega^2}|_{\lambda=\lambda_1}\Omega^2 = k_{0,1} + \frac{1}{v_{g,1}}\Omega + \frac{\beta_{2,1}}{2}\Omega^2 \\ k_2(\Omega) &= k_{0,2} + \frac{\partial k}{\partial\omega}|_{\lambda=\frac{\lambda_1}{2}}\Omega' + \frac{1}{2}\frac{\partial^2 k}{\partial\omega^2}|_{\lambda=\frac{\lambda_1}{2}}\Omega'^2 = k_{0,2} + \frac{1}{v_{g,2}}\Omega' + \frac{\beta_{2,2}}{2}\Omega'^2 \end{aligned} \tag{3.10}$$

where we have used $\frac{\partial k}{\partial\omega} = v_g^{-1}$, and $v_{g,i}$ is the group velocity. $\beta_{2,i} = \frac{\partial^2 k}{\partial\omega^2}|_{\lambda=\lambda_i}$ is the GVD parameter.

Then Eq. 3.9 becomes:

$$\begin{aligned} \frac{\partial\widetilde{A_1}}{\partial z} + j(\frac{1}{v_{g,1}}\Omega + \frac{\beta_{2,1}}{2}\Omega^2)\widetilde{A_1} &= -j\frac{\mu_0\omega^2}{2k_{1,0}}(\tilde{P}^{(2)}_{NL,\omega_0} + \tilde{P}^{(3)}_{NL,\omega_0})\exp(jk_{1,0}z) \\ \frac{\partial\widetilde{A_2}}{\partial z} + j(\frac{1}{v_{g,2}}\Omega' + \frac{\beta_{2,2}}{2}\Omega'^2)\widetilde{A_2} &= -j\frac{\mu_0\omega^2}{2k_{2,0}}(\tilde{P}^{(2)}_{NL,2\omega_0} + \tilde{P}^{(3)}_{NL,2\omega_0})\exp(jk_{2,0}z) \end{aligned} \tag{3.11}$$

Now we take the equation back into time domain by taking an inverse Fourier transform and put in those P_{NL} terms.

$$\begin{aligned} \frac{\partial A_1}{\partial z} + \frac{1}{v_{g,1}}\frac{\partial A_1}{\partial t} - \frac{j}{2}\beta_{2,1}\frac{\partial^2 A_1}{\partial t^2} &= -j\frac{2\omega_0^2}{k_{1,0}c^2}d(z)A_2A_1^*\exp(-j\Delta k_0 z) \\ &\quad - j\frac{n_2k_{1,0}}{n_0}(|A_1|^2 + 2|A_2|^2)A_1 \end{aligned} \tag{3.12}$$

$$\frac{\partial A_2}{\partial z} + \frac{1}{v_{g,2}}\frac{\partial A_2}{\partial t} - \frac{j}{2}\beta_{2,2}\frac{\partial^2 A_2}{\partial t^2} = -j\frac{2\omega_0^2}{k_{1,0}c^2}d(z)A_1^2\exp(j\Delta k_0 z) - j\frac{n_2 k_{2,0}}{n_0}(|A_2|^2 + 2|A_1|^2)A_2 \quad (3.13)$$

where $\Delta k_0 = k_{2,0} - 2k_{1,0}$ is the phase mismatch and $d = \chi^{(2)}/2$. Both Δk_0 and d can be functions of z. For example, d is the quasi-phase matched nonlinear material that I will further discuss in Chapter 4 is a periodic function of z.

Eq. 3.12 and 3.13 are used in Chapter 5 and numerically solved using the split-step Fourier method.

3.2 SHG equations under small signal conditions

While in Eq. 3.12 and 3.13 all the terms, GVM, GVD, SPM and SHG are explicitly shown, the equation is difficult to analytically solve. Under the condition that the pump power is low, the higher order nonlinearity disappears first, and also the change of the pump field is very small, so that the $E_2E_1^*$ term in Eq. 3.12 is zero.

To further simplify the equations, we rewrite the Fourier transform of Eq. 3.4 in the form [57]:

$$E_i(z,\Omega) = A_i'(z,\Omega)\exp(-jk_i(\Omega)z) \quad (3.14)$$

where we note that $k_i(\Omega)$ is a function of Ω in this case, unlike in the previous section.

Following the similar deductions in the previous section, we can find that $A_1'(z,\Omega')$ is invariant over z. Also we can get the equation for the evolution of the SH spectrum envelope function $A_2'(z,\Omega)$:

$$\frac{d}{dz}A_2'(z,\Omega) = -j\frac{\mu_0\omega^2}{2k_2(\Omega)}\widehat{P_{NL}}(z,\Omega)\exp(jk_2(\Omega)z) \quad (3.15)$$

where, compared to Eq. 3.11, the dispersion related terms are taken into the expression of A_2' so that the equation is greatly simplified. The spectral equation is more convenient for understanding our spectral coding and correlation scheme discussed later.

Here the nonlinear polarization spectrum $\widehat{P_{NL}}$ is given by:

$$\widehat{P_{NL}}(z,\Omega) = 2\epsilon_0 d(z) \times \int_{-\infty}^{\infty} A_1'(\Omega')A_1'(\Omega-\Omega')\exp(-j[k_1(\Omega')+k_1(\Omega-\Omega')]z)d\Omega' \quad (3.16)$$

which is the Fourier transform of the nonlinear polarization P_{NL}.

By integrating Eq. (3.15) over z, we get the output A_2:

$$\begin{aligned} A_2'(\Omega) &= \int_{-\infty}^{\infty} dz' \Gamma(z') \exp(jk_2(\Omega)z') \\ &\times \int_{-\infty}^{\infty} A_1'(\Omega') A_1'(\Omega - \Omega') \exp(-j[k_1(\Omega') + k_1(\Omega - \Omega')]z) d\Omega' \end{aligned} \quad (3.17)$$

where $\Gamma(z) = -j4\pi d(z)/\lambda_1 n_0$ is the nonlinear coupling coefficient. Here λ_1 is the fundamental wavelength.

Then, if the fundamental and SH waves are phase matched at the center frequency of their spectrum, Eq. (3.17) can be simplified to [57]:

$$A_2'(\Omega) = 2 \int_0^{\infty} A_1'(\Omega/2 + \Omega') A_1'(\Omega/2 - \Omega') d\Omega' \cdot D(\Omega) \quad (3.18)$$

The transfer function $D(\Omega)$ represents the effect of phase matching condition on the SHG spectrum generated and is given by:

$$D(\Omega) = \int_{-\infty}^{\infty} \Gamma(z) \exp(-j\alpha\Omega z) dz \quad (3.19)$$

where $\alpha = 1/v_{g1} - 1/v_{g2}$ is the group-velocity mismatch (GVM) between the fundamental pulse and the SH pulse. For a uniform nonlinear crystal (NLC) of length L, $D(\Omega)$ is given as:

$$D(\Omega) = \Gamma L sinc(\Omega\alpha L/2) \quad (3.20)$$

This effect may limit the possible SHG frequency bandwidth to $\sim \frac{0.88}{L|\alpha|}$ [53].

3.2.1 Thin nonlinear crystals and broadband SHG

When thin nonlinear crystals (i.e., $L \ll \tau/|\alpha|$, where τ is the pulsewidth of an unchirped pump pulse) are used, the temporal walk-off between the fundamental and SH pulses is small compared to their pulsewidths, so that the two pulses stay together in the nonlinear interaction process (as illustrated in Fig. 3.1(a)). In this limit, the function $D(\Omega)$ is much broader than the source term (the auto-convolution term of

A_1) on the right hand side of Eq. (3.18), and it can be considered as constant in the region of interest and its effect can be ignored. For broadband SHG, the SHG power P_{SHG} is given by:

$$\int_{-\infty}^{\infty} |\int_{-\infty}^{\infty} A_1'(\Omega/2+\Omega')A_1'(\Omega/2-\Omega')d\Omega'|^2 d\Omega = \int_{-\infty}^{\infty} I_1^2(t)dt \qquad (3.21)$$

where I_1 is the temporal intensity function of the pump pulse. Therefore, the SHG power is only related to the optical intensity and not sensitive to the optical temporal phase distributions. It is noted that the two photon absorption effect in Chapter 2 can also be described by an equation in the same form of Eq. (3.21) [50], and we also experimentally observed their similarity.

3.2.2 Thick nonlinear crystals and narrowband SHG

On the other hand, in thick crystals, where the GVM is large (i. e., $L \gg \tau/|\alpha|$), $D(\Omega)$ can be significantly narrower than the first term on the right hand side of Eq. (3.18). In applications where broadband SHG is required, which include most femtosecond applications, this spectral narrowing effect is considered unfavorable and, therefore, left largely unexplored. Equivalently in the time domain, the GVM between fundamental and SH pulses causes the SH pulses to walk off from the fundamental, which leads to a temporal broadening of the SH output pulse, as shown in Fig. 3.1(b). This is also usually considered undesirable, and therefore most femtosecond experiments are performed with thin SHG crystals ($L \ll \tau/|\alpha|$).

However we show that in a signal processing context, the GVM can be beneficial. Consider the situation where the length of the nonlinear crystal is very large, so that $D(\Omega)$ approaches a δ-function. Then the output SHG power is given as [60]:

$$\int_{-\infty}^{\infty} |A_2'(\Omega)|^2 d\Omega = 8\pi\Gamma^2 L |\int_0^{\infty} A_1'(\Omega')A_1'(-\Omega')d\Omega'|^2/|\alpha| \qquad (3.22)$$

i. e. it is proportional to the self-convolution of the pump field spectrum. As it is related to the field instead of intensity functions, this is sensitive to the phase functions, and is fundamentally different from the broadband two-photon processes,

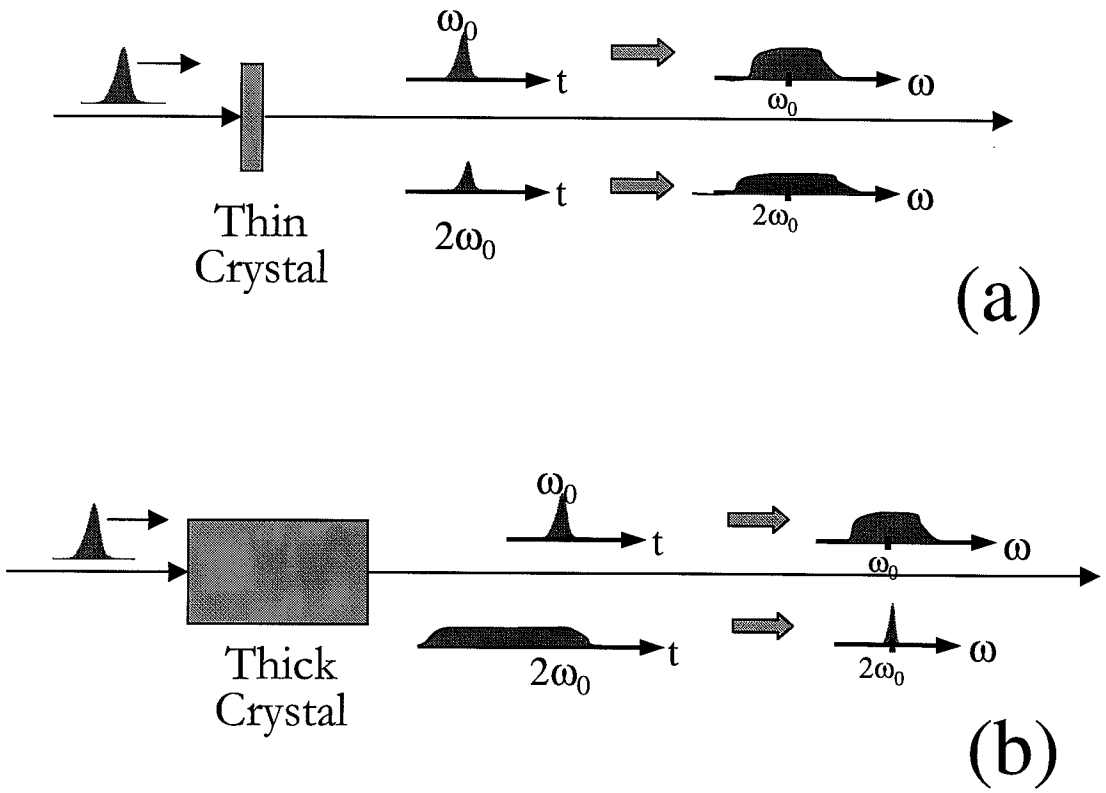

Fig. 3.1. SHG of short optical pulses in thin and thick nonlinear crystals.

like SHG in thin crystals or TPA into a continuum [50]. It should be noted that the transition probability for two photon absorption (TPA) in an atomic medium (i. e. with narrow discrete initial and final states) has the same functional form as the above equation, assuming the weak response condition and no intermediate resonance [61].

Eq. (3.22) also shows that the SH power scales linearly with L. For large L ($\sim$ cm), highly efficient SHG of femtosecond pulses can be achieved even under conditions of large group-velocity mismatch. This was demonstrated in [62], where nearly 60 % SHG conversion efficiency was obtained using only $\sim$ 150 milliwatts average power from a modelocked Ti:sapphire laser. This potential for high efficiency is of great importance for the CDMA communication systems.

3.3 CDMA Correlation and Coding Scheme

Base on Eq. (3.22) above, we design our optical waveforms in the following way, as illustrated in Fig. 3.2: Our optical spectrum at 1.56 μm wavelength should have a flat-top (e. g. $|A_1(\Omega')|$ is near constant within a certain frequency range and zero otherwise) and unchirped. The fundamental spectrum is divided into 2N 'channels' with an equal frequency width, each of which is given a phase shift $\Phi_i (i = -N, \ldots, -1, 1, \ldots, N)$. We divide the spectrum in half and call the phase patterns on the low frequency and high frequency sides of the spectrum $C_1 = \{\Phi_{-1} \ldots \Phi_{-N}\}$ and $C_2 = \{\Phi_1 \ldots \Phi_N\}$, respectively. Thus the SHG signal would be the coherent sum of the signals from N pairs of channels and is proportional to:

$$|\sum_{i=1}^{N} \exp(j\Phi_i) \exp(j\Phi_{-i})|^2 \tag{3.23}$$

e. g. the square of the magnitude of the correlation function between code words C_1 and C_2. The SHG output is then directly related to the correlation properties of the applied spectral phase functions.

In such a ultrashort pulse CDMA system (see Fig. 3.2), the spectral phase code C_1 is applied at the transmitter to the spectrum and C_2 is applied by the receiver. Based on our previous discussion, we know that SHG in long nonlinear crystals can

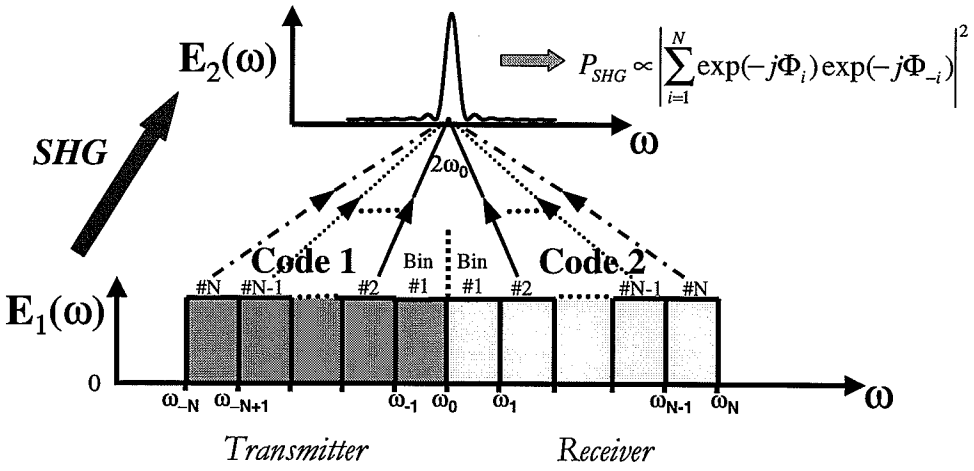

Fig. 3.2. Scheme of spectral phase coding for SHG spectral correlators.

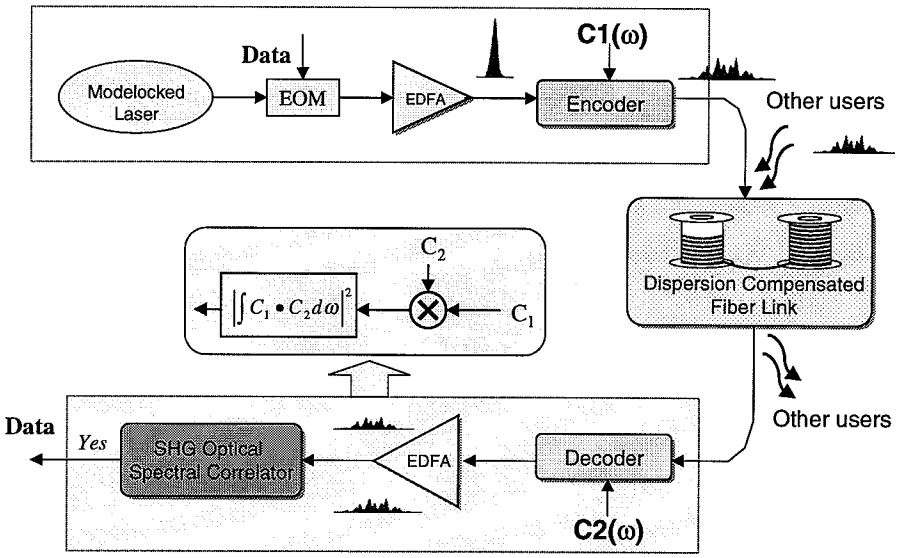

Fig. 3.3. Scheme of optical CDMA system using SHG spectral correlators.

work as an optical spectral correlator. If the C_1 and C_2 are selected from a code set with low cross correlations, only the signals coded with a matched C_1 and C_2 pair can generate significant SHG output, and the pulses coded with unmatched C_1 and C_2 will generate little signal. Thus the rejection of multi-access interference noise is realized.

It should be noted that this is a different coding/decoding scheme compared to those described in earlier UP-CDMA publications [3, 19], and it is designed to fit the functionality of the proposed SHG spectral correlator. Also the selection criteria of the spectral codes are also slightly different here, and the orthogonality of the codes is more important than their randomness as in the previous coding scheme. For the random codes used in the previous coding schemes, the autocorrelation of

each codeword should have an impulse-like shape. For orthogonal codes, it is the cross-correlations between different codewords that need to be a delta-function.

4. EXPERIMENTAL STUDIES OF SPECTRAL CODE CORRELATOR BASED ON SHG IN THICK CRYSTALS

In this chapter, the experimental studies of SHG using spectrally coded optical pulses are given. We used PPLN (both bulk and waveguide PPLN) as the nonlinear meterial, and the results demonstrated a great potential of realizing both high MAI suppression ratio for the CDMA system and high conversion efficiency (thus low operating power requirement).

We first briefly introduce the idea of quasi-phase matching and periodically poled materials. Then the experimental setup and methods are discussed. Finally experimental results are given.

4.1 Quasi-Phase Matching and PPLN

The development of the appropriate nonlinear optical devices could be of great importance to realize an all-optical scheme, which is also true in our case. Quasi-phase-matching (QPM) technique, as an alternative to the conventional phase matching techniques for parametric processes, offers great advantages, some of whom are very important for real-world applications.

In a QPM material, the nonlinear coefficient is modulated with a period related to the coherence length of the interaction to offset the accumulated material phase mismatch [63]. Since late 80's, various materials, including nonlinear crystals [56, 64] and semiconductors [65, 66], had been studied to realize QPM. The advantages of QPM over conventional techniques mainly are: any interaction within the transparency range of the crystal can be noncritically phase matched at a specific temperature, which avoids spatial walkoff; QPM allows the use of largest nonlinear coefficients in the particular material. Besides the above advantages, PPLN, as the most success-

ful QPM material so far, also has large nonlinearity and GVM parameter ($\sim$ 0.3 ps/mm) and is availability in relatively large sizes (which is rather important for our applications) [67].

PPLN is normally fabricated by applying an external electric field (typically > 20 kV/mm) to reverse the polarity of the ferroelectric domains [56]. PPLN can be used in many parametric processes, such as second-harmonic generation (SHG), third-harmonic generation (THG), difference frequency generation (DFG) and sum-frequency generation (SFG), over a large wavelength range [56, 68, 69, 70, 71, 72, 67, 73, 74].

For SHG and PPLN with uniform gratings for first order QPM, the phase mismatch Δk is given by:

$$\Delta k = 2\pi(\frac{n_2}{\lambda_2} - 2\frac{n_1}{\lambda_1} - \frac{1}{\Lambda}) \tag{4.1}$$

where Λ is the period of the grating. For a fixed Λ, the phase matching wavelength can be temperature tuned. The phase matching temperature (wavelength) can be predicted by using the following Sellmeier equation of extraordinary refractive index of bulk PPLN [75]:

$$n_e^2 = a_1 + b_1 f + \frac{a_2 + b_2 f}{\lambda^2 - (a_3 + b_3 f)^2} + \frac{a_4 + b_4 f}{\lambda^2 - a_5^2} - a_6\lambda^2 \tag{4.2}$$

where the temperature parameter f is given by $f = (T - T_0)(T + T_0 + 2 \times 273.16)$ with temperature T expressed in degrees Celsius and $T_0 = 24.5^oC$. Other constants a_i and b_i are available from [75].

Since the crystal is often used at elevated temperatures, the expansion of the grating period should also be considered [75]:

$$\Lambda = \Lambda_{25^oC}[1 + \alpha(T - 25^oC) + \beta(T - 25^oC)^2] \tag{4.3}$$

where Λ_{25^oC} is the length at 25^oC.

Ideally the nonlinear parameter of the 1st order QPM material is $2/\pi$ times the original nonlinear coefficient. For PPLN, the largest component in the d tensor, d_{33}

that is as large as 16.5 pm/V is used. In this case, all interaction beams are polarized along the z-axis of the z-cut crystal.

4.2 Experimental Setup

In our experimental setup, as shown in Fig. 4.1, a passively mode-locked fiber laser at 1560 nm [47] was used, which had a repetition rate of $\sim$ 40 MHz, like the one used in the TPA work, but had a different spectral shape and higher output power. Since a polarization beam splitter cube was used in the laser cavity as the mode locking component and the state of polarization could be changed by the polarization controllers (PC's) in the cavity, the output pulse shape could be significantly changed, by adjusting the PC by merely a few degrees (while the laser stayed mode-locked). Shown in Fig. 4.2 are the intensity autocorrelation traces of the direct output from the laser (no external spectral filtering) when the PC was slightly adjusted. This caused additional difficulties to carry out cross-correlation measurements as further discussed later in this chapter, since it was more difficult to consistently compensate the dispersion of reference pulses from time to time.

A fiber-pigtailed femtosecond pulseshaper [19] with a 128-pixel amplitude/phase LCM array [48, 76] was used to apply spectral phase codes consisting of different choices of C_1 and C_2 to the femtosecond optical pulses. The coded waveforms simulates the kind of optical inputs to an optical spectral correlator in the CDMA system, under an ideal distortion-free transmission condition. After transmission by an $\sim$ 4 m length of single mode fiber, the pulses were coupled into free-space and then launched into the PPLN crystal sample placed in a temperature controlled oven. The state of polarization of the pump beam was controlled by a half-wave plate so that the light was linearly polarized along the z-axis of the crystal. The sample was heated to an elevated temperature so that the SHG phase matching wavelength was tuned to $\sim$ 780 nm, the center of the input spectrum, and the photorefractive effect was eliminated. The SHG output at 0.78 μm wavelength generated by the PPLN was collected and sent into a computer controlled spectrometer with a resolution of $\sim$ 0.03 nm. A photomultiplier tube (PMT) and lock-in amplifier were used with the

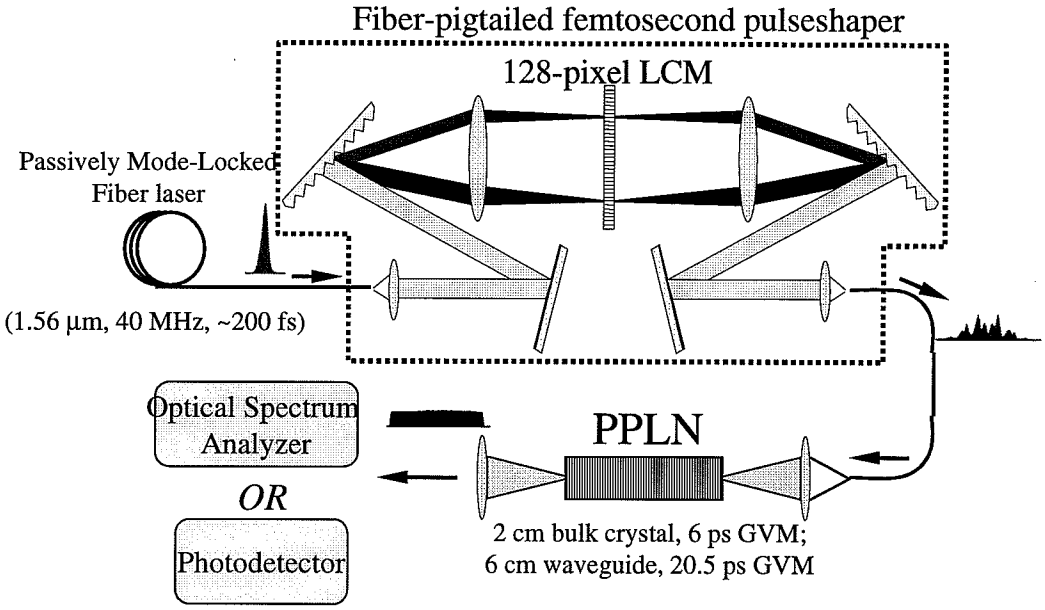

Fig. 4.1. Scheme of PPLN SHG experimental setup.

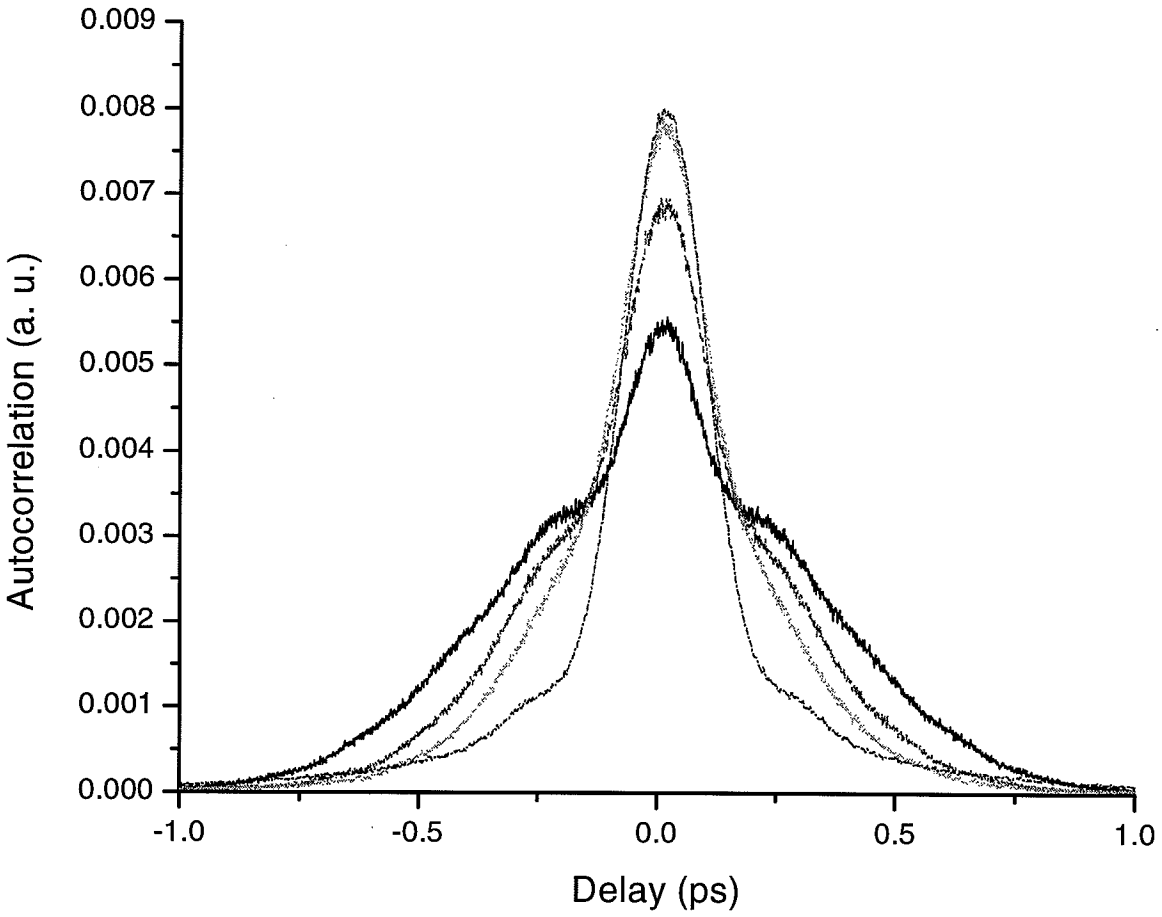

Fig. 4.2. Pulse shape variation due to different state of polarization in the fiber laser.

spectrometer. The SHG spectra were measured for pump pulses coded with various phase code pairs of C_1 and C_2. In some later experiments, a high-speed photodiode was also used to directly measure the SHG signals.

Two kinds of PPLN samples were used in our studies. First, a commercial PPLN crystal from Crystal Technology was used, which was 20 mm long and 0.5 mm thick and had a quasi-phase-matching grating with 19.0 μm period. The light was loosely focused into the crystal, with a depth of focus longer than the crystal. The GVM of the bulk PPLN is $\sim$ 0.3 ps/mm, corresponding to a total GVM of $\sim$ 6 ps.

The second sample used was annealed proton exchanged PPLN waveguides [77], which had a 55.5-mm-long SHG section with a uniform grating period of 14.75 μm and tapered sections at the input and output ends to facilitate better light coupling. The sample was fabricated and provided by M. H. Chou and K. R. Parameswaran from the group of Prof. M. M. Fejer at Stanford University. The waveguide was designed to support mainly the TM_{00} mode at the pump wavelength. In the tapered coupling region, the width of the fundamental mode is 10.7 μm and the depth is 8.28 μm (at $1/e^2$), and the width and depth of the SH mode are 5 and 3.52 μm, respectively [78]. In the SH interaction region, the width and depth of the pump mode are 8.12 and 4.41 μm, and those of the SH mode are 5.05 and 2.07 μm, respectively. The modes are symmetric in width and asymmetric in depth [78]. The peaks of the two modes also don't overlap in depth. The GVM of this annealed proton exchanged waveguide is $\sim$ 0.37 ps/mm, corresponding to a total GVM of $\sim$ 20.5 ps. This implies a theoretical second harmonic phase matching bandwidth of $\sim$ 0.1 nm. The observed SHG bandwidth, as shown in Fig. 4.10 later, was $\sim$ 3 times wider than the ideal value, presumably due to small structural or temperature nonuniformity in the device.

In either case, the SH bandwidth is smaller than the frequency width of each 'bin' in the coding process ($\sim$ 1.1 nm at 1560 nm) so that the assumptions of Eq. 3.22 are satisfied.

4.3 Generation of Spectrally Coded Pulses

The faithful generation of the spectrally coded femtosecond pulse is important to fully explore the potential of the optical spectral correlation scheme.

As a crucial device for the optical pulse shaping, the amplitude/phase LCM needs to be carefully calibrated. Since we used an amplitude/phase LCM here, its phase vs. drive voltage level table can be in-situ calibrated [76]. It is also found from our experience that small variations in the yaw angle of the LCM in the pulse shaper can cause small but significant changes to the calibration results.

In the preceding sections on the theoretical description of the spectral correlation mechanism, it is stipulated that the optical spectral intensity should be nearly constant within the bandwidth. Experimentally, the direct laser output had a spectrum (a typical one can be seen in Fig. 4.3) significantly wider than the spectral window imposed by the physical window size of the LCM and the configuration of the pulse shaper. The common presence of a CW peak in the laser spectrum had no effect on our experiments, as it fell out of the spectral window of the pulse shaper. The spectrum passed through the pulseshaper had a significantly nonuniform shape and needed to be equalized. A transmittance function was applied to the LCM, which is proportional to the inverse of the original spectral distribution. The spectra before and after gain equalization are shown in Fig. 4.4, where we can see that the pump spectrum was quite flat within the $\sim$ 18 nm bandwidth. Any residual spectral phase chirp from the fiber system was also compensated [15] by applying appropriate quadratic and cubic phase functions to the LCM along with the phase codes.

Because of the relative broad spectrum and the large incident angle ($\sim 70^{o}$) to the grating in the pulse shaper, the mapping between the linearly spaced pixels on the LCM and their corresponding optical frequencies was no longer strictly linear [79]. When the pixel position vs. its corresponding optical frequency was measured, it was observed that the curve significantly deviated from a linear function, and at the two ends of the LCM the deviation from a linear mapping can be as large as 0.3 nm (e. g. more than 2 pixel size). Though this effect didn't have a significant influence

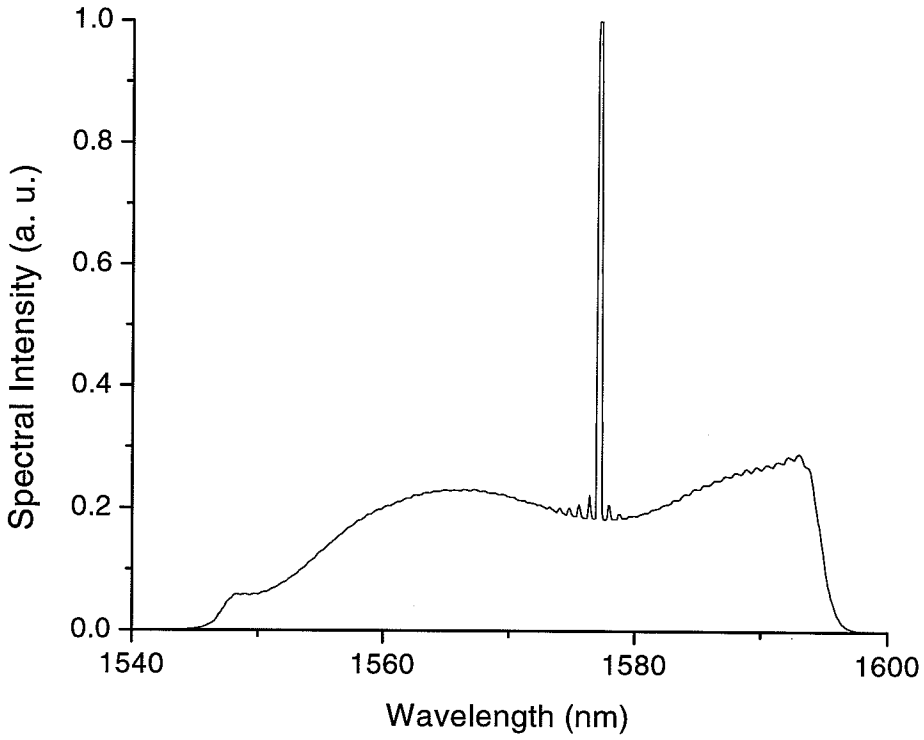

Fig. 4.3. Spectrum of the output from the fiber laser used in the PPLN SHG studies.

on the results of the TPA work where the bandwidth was only 3-4 nm wide, it could make a significant difference here. A direct, linear mapping of the code function to the pixels would result in actually spectral code bins of different bandwidths. Since, in the coding scheme used here, it is required that the frequency bandwidth of each code bit should be the same, optical coded signals generated by the simple linear mapping would not be able to generate the highest contrast ratio. Therefore, special cares were taken to map all the functions of frequency (including the dispersion compensation and gain equalization functions) to the modulation functions to each individual pixels based on the measured pixel vs. frequency curve. An example of the phase code function and its mapped version is given in Fig. 4.5. Due to the pixelation nature of the LCM, this mapping can not be perfect especially for functions varying very fast, however, in our following experiments the results seemed to be good.

As to the spectral phase codes used, we studied two different families of binary phase codes with known correlation properties. As a first case, we chose C_1 and C_2 from a set of eight length-8 Hadamard codes (see the below matrix which consists eight code words as the row vectors) [80], which are orthogonal in their bipolar form and therefore should suppress the SHG signal at $\Omega = 0$ very strongly, ideally to zero. To convert the binary codes to phase codes, we set Φ_i to π when the corresponding code bit is -1, and to 0 when the corresponding bit is 1.

$$\begin{bmatrix} -1 & -1 & -1 & -1 & -1 & -1 & -1 & -1 \\ -1 & 1 & -1 & 1 & -1 & 1 & -1 & 1 \\ -1 & -1 & 1 & 1 & -1 & -1 & 1 & 1 \\ -1 & 1 & 1 & -1 & -1 & 1 & 1 & -1 \\ -1 & -1 & -1 & -1 & 1 & 1 & 1 & 1 \\ -1 & 1 & -1 & 1 & 1 & -1 & 1 & -1 \\ -1 & -1 & 1 & 1 & 1 & 1 & -1 & -1 \\ -1 & 1 & 1 & -1 & 1 & -1 & -1 & 1 \end{bmatrix}$$

In our experiments, C_1 was fixed to the second code word in the code set, while C_2 is varied among all words in the set. Shown in Fig. 4.6, the spectral phase coding

process spreads the unchirped femtosecond input pulse into lower intensity waveforms approximately 10 psec long and with complicated substructures. The temporal profiles of the pulses were measured using intensity cross-correlation method. A reference pulse was obtained from a not-filtered laser output which had a pulsewidth of $\sim$ 110 fs. As noted earlier, reliable measurements were only possible when the mode-locking position of the laser (like the PC positions in the laser) was kept very stable during the period of measurements.

Shown in Fig. 4.7 are experimental cross-correlation measurements of the intensity profiles of coded pulses as well as the theoretical intensity profiles. Data are shown for two different choices of C_2. In each case we see a close match between the calculated waveforms and the data, except that the experimental data are smoothed somewhat due to the finite pulsewidth of the reference pulse, which is not taken into account in the simulation. Since, for originally unchirped input spectrum, any $0-\pi$ phase codes applied should generate symmetric output temporal function, as shown in Fig. 4.7, this verifies the accuracy of the LCM calibration and the chirp compensation process.

Even though the two intensity profiles look quite similar, the correlation properties of the concatenated codes are quite different. One of them (Fig. 4.7(a)) consists of highly correlated codewords. The phase code { 1 -1 1 -1 1 -1 1 -1 ⋮ -1 1 -1 1 -1 1 -1 1 } was used, and it consisted of C_1 and C_2 with the bits in C_1 arranged from right to left and the bits in C_2 arranged from left to right (as shown in Fig. 3.2). Here C_1 and C_2 were the same: { -1 1 -1 1 -1 1 -1 1 }, the second code word in the Hadamard matrix (see [80]). This pump waveform should yield the same SH intensity at the center frequency ($\Omega = 0$) as the uncoded case as we discussed in the previous sections. The other (Fig. 4.7(b)) consists of two orthogonal codewords ($C_1 \neq C_2$), the phase code { 1 -1 1 -1 1 -1 1 -1 ⋮ -1 1 -1 1 1 -1 1 -1 } was used, with C_1 kept the same and C_2 being the sixth word: { -1 1 -1 1 1 -1 1 -1 }, which ideally should null the SH at $\Omega = 0$.

As the second case, we used the M-sequence code, which has an finite auto-/cross-correlation ratio of 1/(code length). This should lead to a contrast ratio

of $(codelength)^2$ between matched and unmatched codes. Similar to the case of Hadamard codes, the waveforms coded with code words of length-7 and length-15 M-sequence codes are shown in Fig. 4.8 and Fig. 4.9, respectively. Length-15 M-sequence codes spread the pulse in a temporal window more than 10 ps long, about twice as large as the length-7 codes.

It is noted that those pulses coded with M-sequence codes had smoother waveforms and lower peak intensities than those coded with Hadamard codes (because of the pseudorandom nature of the M-sequence codes), while the latter yields much stronger contrast. This is in contrast to the results in [45], where the intensities of the waveforms decide the contrast, because of the difference between the two schemes described in Eq. (3.22). Also the two matched coded pulses shown in Fig. 4.8 and Fig. 4.9 respectively should generate comparable amount of SHG signals at the center frequency, though the latter has a peak intensity about half as that of the former.

4.4 Experimental Results Using Bulk PPLN Samples

First, we measured the SH spectrum for pump pulses coded with different combinations of Hadamard code words. With a pump pulse energy of $\sim$ 2 pJ, Fig. 4.10 shows that, for uncoded pulses, the SHG generated from the equalized, unchirped pump input has a $sinc^2$ shape with a bandwidth of $\sim$ 0.3 nm, in good agreement with the theory. The conversion efficiency was low enough that the no-depletion condition was satisfied. For coded pulses, in the situation with correlated codes ($C_1 = C_2$, as in Curve II), strong SHG was observed and its peak is comparable to that of the uncoded case (Curve I), even though the input pulse has been dispersed significantly in time. The SHG bandwidth is now dominated by the correlation function of the code and is narrower than in Curve I. The minor difference in the peak intensities of Curves I and II may arise from small imperfections in the coding process. For each of the six other cases where $C_1 \neq C_2$, the seven traces corresponding to $C_1 \neq C_2$ show very weak SHG. Compared with the uncoded pulse case, the SHG at the center frequency was suppressed by at least 600 for all seven unmatched codes and by more than 1500 in some traces (limited by the noise floor of our measurements).

As a second case, the pump pulses are coded with different combinations of M-sequence codes. As seen in Fig. 4.11, though the SHG spectra have vastly different shapes at wavelengths other than the center wavelength (779.75 nm), the spectral strength is suppressed by a similar factor of 50 at the center. This quantitatively proves the 'correlation squared' relation described in Eq. 3.23.

From the CDMA application point of view, the orthogonal codes like Hadamard codes would yield superior contrast ratio. Other types of (nearly) orthogonal codes with different characteristics in other aspects could also be applied to the CDMA. Therefore, our scheme opens up a large set of possible codes which had been widely studied for years for radio frequency CDMA or other communication applications.

We realize that, even though the optical waveforms we demonstrated above under well controlled experimental condition were able to realize the excellent contrast ratio, in a real system, the often inevitable nonideal realization of the scheme can adversely affect the eventual outcome. One of the most obvious problem for the fiber systems is dispersion. In Fig. 4.12, we show the SHG spectra of the coded pump waveforms with the existence of a quadratic spectral distortion ($\sim 0.018\ ps/nm$, e. g. a maximum of $\sim 0.15\pi$ phase change across the spectral bandwidth), which can be caused by residual second order dispersion in the fiber transmission link. This set of waveforms which showed very similar SHG suppression in Fig. 4.10 under chirp-free conditions now show quite different results. Not only are the shapes of the SHG spectra different, but now some codes now generate much more SHG than others. This difference lies in the different symmetry of the spectral codes used and implies that some code combinations may be more 'vulnerable' to chirps than others. With a large number of different spectral codes available to us based on our spectral correlation scheme, it may be possible to design a set of nearly orthogonal codes which are less susceptible to dispersions.

On the other hand, we have observed that third order dispersion, which also often plays an important role for ultrashort pulse systems, has nearly no effect on the SHG outputs in our scheme. This finding can be easily explained by the following equation.

The yield of coded pump pulses with the third order dispersion represented by a cubic spectral phase term is proportional to:

$$\left|\sum_{i=1}^{N} \exp(j(\Phi_i + a\Omega^3)) \exp(j(\Phi_{-i} - a\Omega^3))\right|^2 = \left|\sum_{i=1}^{N} \exp(j\Phi_i) \exp(j\Phi_{-i})\right|^2 \qquad (4.4)$$

Here a represents the strength of the third order dispersion, and the antisymmetric phase distortions on the two sides cancel each other out. Since, for subpicosecond pulses transmitted over a relatively long length of fiber (like tens of kilometers), third order dispersion is one of the dominant factors for pulse distortion and often challenging to fully compensate [15, 19, 16], this 'invulnerability' to odd-order dispersions could significantly ease the requirements placed on the dispersion compensation system.

4.5 Experimental Results Using PPLN SHG Waveguides

We first measured the SHG efficiency using the uncoded pulses. The results shown in Fig. 4.13 show a small signal efficiency of $\sim$ 50%/pJ. This is more than 500 times higher than the efficiency demonstrated using bulk PPLN under the small GVM condition [81], due to the high interaction intensity in the waveguide and the long interaction length of the sample under the large GVM condition. The SHG efficiency began to saturate at input internal pump pulse energy higher than 0.5 pJ, and the SHG efficiency under large pump depletion condition will be further discussed in the next chapter. In order to obtain good coupling efficiency, it would be convenient that a telescope consisting of two lenses is used before the focusing lens to adjust the free space beam size so that optimal mode matching can be achieved. It would also provide additional freedom in optimizing the coupling, as we had only xyz stages in the setup. Here two lenses with focal lengths of 60 mm and 40 mm, respectively, were used to form the telescope.

To verify the spectral correlation function of the PPLN SHG waveguide device, similar to the case of using bulk PPLN samples, the SHG output spectrum was measured using different coded pump waveforms. For pump signal coded with length-

8 Hadamard codes, when a correlated code was applied, strong SHG was observed. On the other hand, for all the other seven cases corresponding to not-correlated codes, the SHG signals were suppressed by at least 50 times, as shown in Fig. 4.14.

The high efficiency and the spectral narrowing effect caused by the large GVM enabled the use of a high-speed avalanche photodiode (APD) for direct real time detection for pump pulse energies < 1 pJ, in contrast to the lock-in detection in the bulk PPLN studies [60]. To study the phase code dependence, we used phase codes from a set of eight length-8, orthogonal Hadamard codes, which should yield large contrast in the SHG signal. Fig. 4.15 shows the SHG signals displayed on a digital oscilloscope driven by the APD with an internal transimpedance amplifier. The APD (Hamamatsu C5658) had a quantum efficiency of $\sim 70\%$ at 780 nm wavelength and a total avalanche plus amplifier gain of $\sim 10^4$. For coded pulses with $C_1 = C_2$, significant SHG comparable to the no coding case was generated for each input pulse, and an electrical pulse train at ~ 40 Mbit/s was observed. At only $\sim 10\ \mu W$ average power input (0.25 pJ per pulse before the coupling lens), the electrical signal was as large as 500 mV peak-to-peak and had a pulsewidth of ~ 1 ns, limited by the 500 MHz scope bandwidth and ~ 1 GHz photodetector bandwidth. The voltage signal-to-noise ratio (SNR) is $\sim$ 50:1, which should be sufficient for low error rate detection. For each of the 7 other cases where $C_1 \neq C_2$, the SHG signal was significantly suppressed so that, at the same input power level, no observable electrical pulses were present in the trace shown in Fig. 4.15. Compared with the uncoded pulse case, the total SHG signal was suppressed by at least 50 for all seven unmatched codes. We expect that potentially higher suppression ratios as demonstrated in [60] should also be possible in the waveguide experiments, through improved precision in the coding process and by using SHG devices with a more ideal (hence narrower) SHG tuning curve or by applying external spectral filtering (at the expense of increased loss).

A power SNR of about 15 to 20 dB is normally required to obtain a BER of 1×10^{-9} [46] in digital optical communication systems. Based on the above observations, at ~ 0.1 pJ pulse energy level, the SNR we observed would be enough for error-

free detections. When we consider a high speed system with the same pulse energy level, 0.5 mW average power per channel is needed at the bit rate of 10 Gbit/s. At the conversion efficiency of 5%, the SHG power of 25 μW is also well above the minimal power requirement for the optical receivers [46]. Therefore, we believe that such optical spectral correlators offer the potential to operate at mW power level at $\sim$ 10 Gbit/s speed with sufficient SNR for high quality communications. This would be significant breakthrough in lowering the operating power of nonlinear signal processing devices required by optical CDMA systems and enhancing the viability of ultrashort pulse CDMA schemes.

For communication applications, it is desired that the devices are polarization insensitive, as the optical signals after transmission through a significant length of fiber are normally randomly polarized. Even though our current device is polarization dependent, it is also noted that a polarization independent device can be realized by methods demonstrated in [82].

4.6 Summary

In summary, we have demonstrated a novel yet simple scheme for distinguishing between different, phase coded ultrafast optical waveforms for proposed coherent CDMA networking. Because of the high conversion efficiency using PPLN SHG waveguide devices, we believe that it should be possible to realize nonlinear code recognition operation at many Gb/s per user at <1 mW average power per user. This advance offers the possibility of ultrashort pulse CDMA systems operating at realistic power budgets.

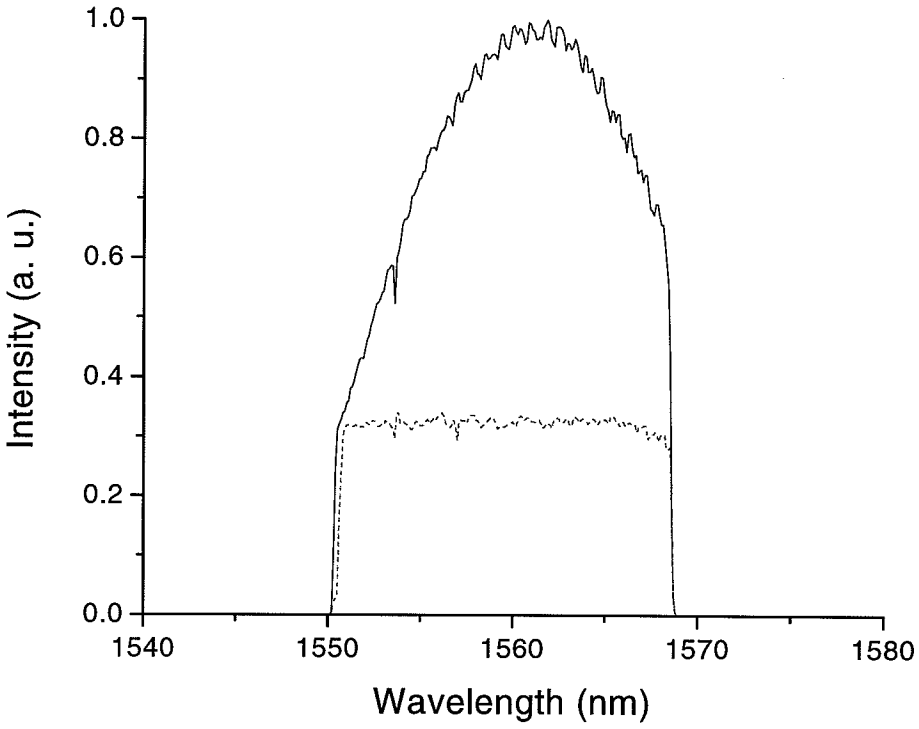

Fig. 4.4. Gain equalization of the pump spectrum.

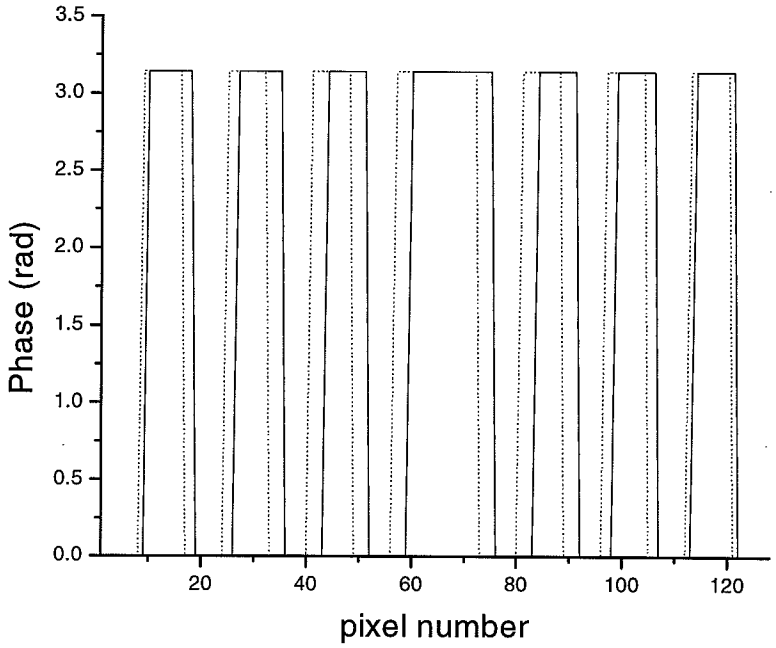

Fig. 4.5. The mapping of the spectral phase coding function to the spatial modulation function of LCM.
The solid line is the mapped modulation function considering the actual frequency of each pixel position, and the dotted line is the result assuming a linear mapping.

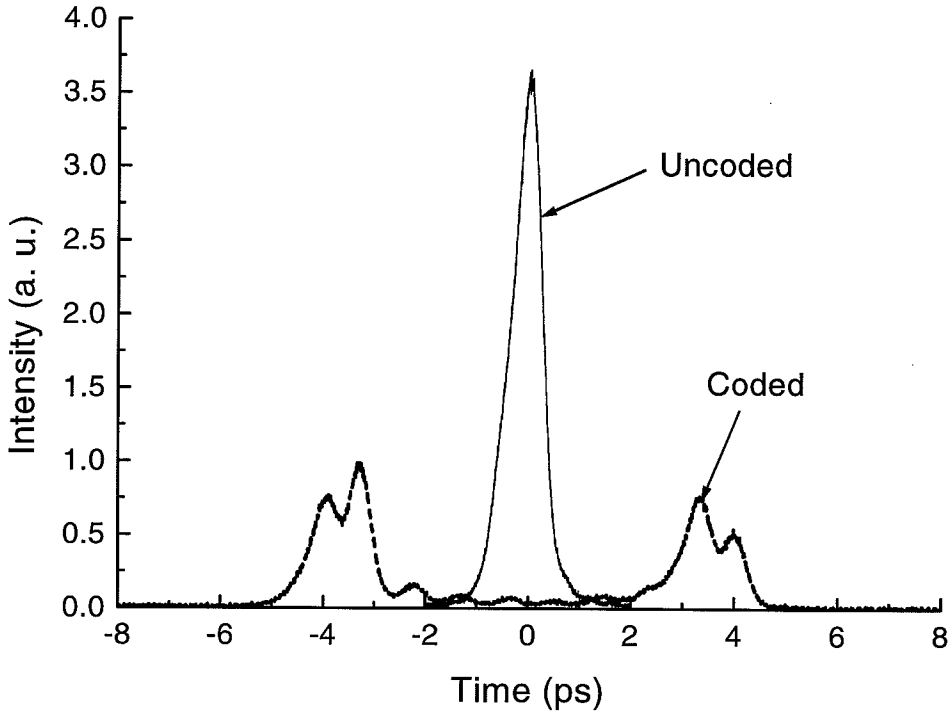

Fig. 4.6. Experimental intensity cross-correlation data of spectrally uncoded and coded pulses.

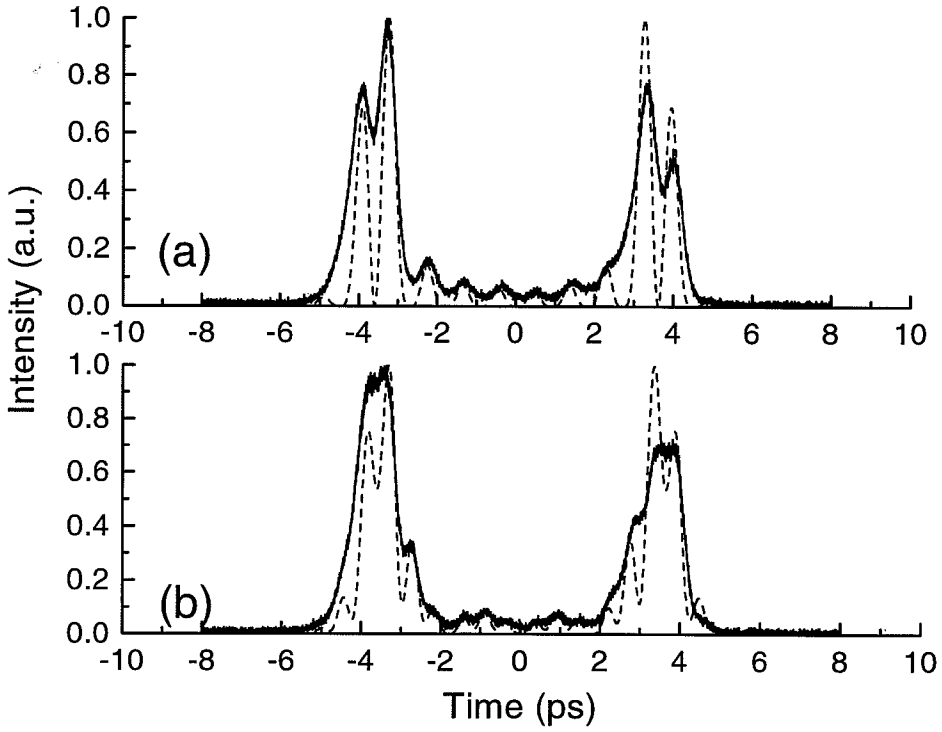

Fig. 4.7. Theoretical intensity profiles and experimental intensity cross-correlation data of pulses spectrally coded with Hadamard codes.

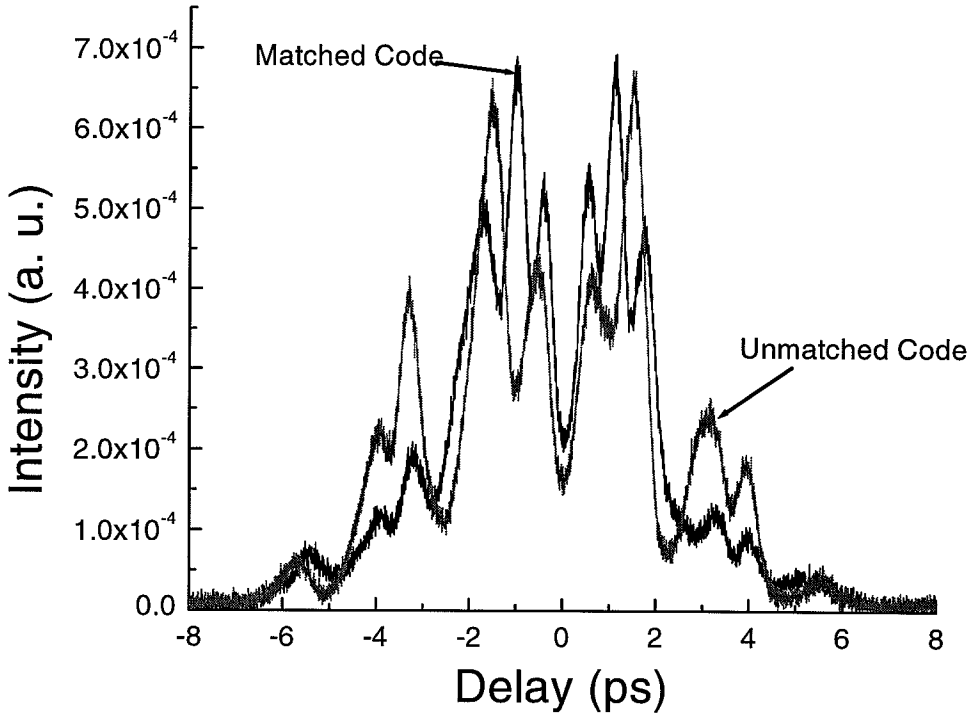

Fig. 4.8. Experimental intensity cross-correlation data of pulses spectrally coded with length-7 M-sequence codes.

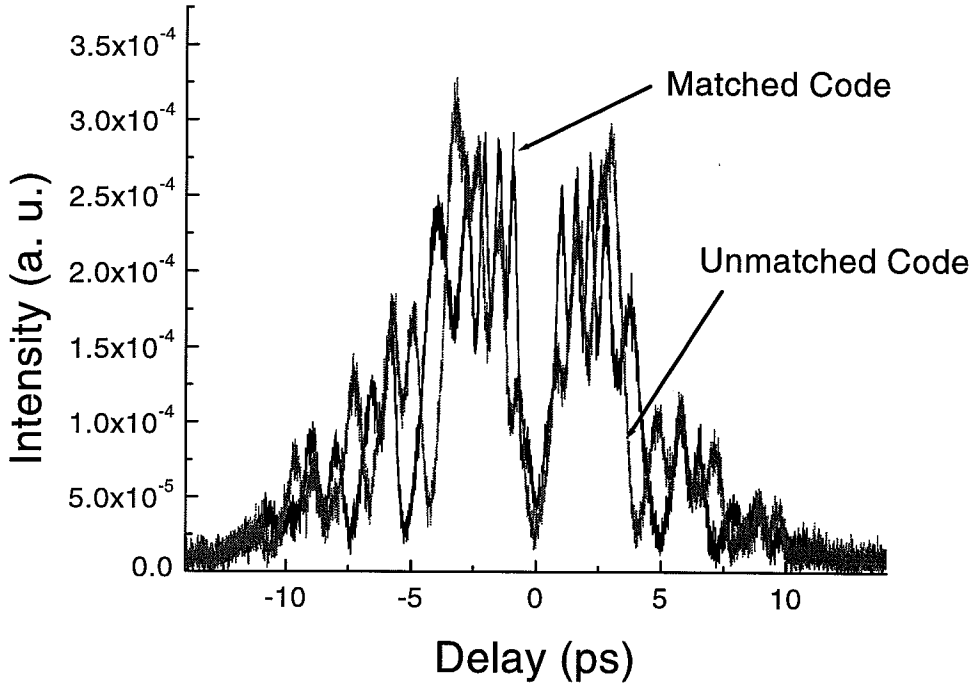

Fig. 4.9. Experimental intensity cross-correlation data of pulses spectrally coded with length-15 M-sequence codes.

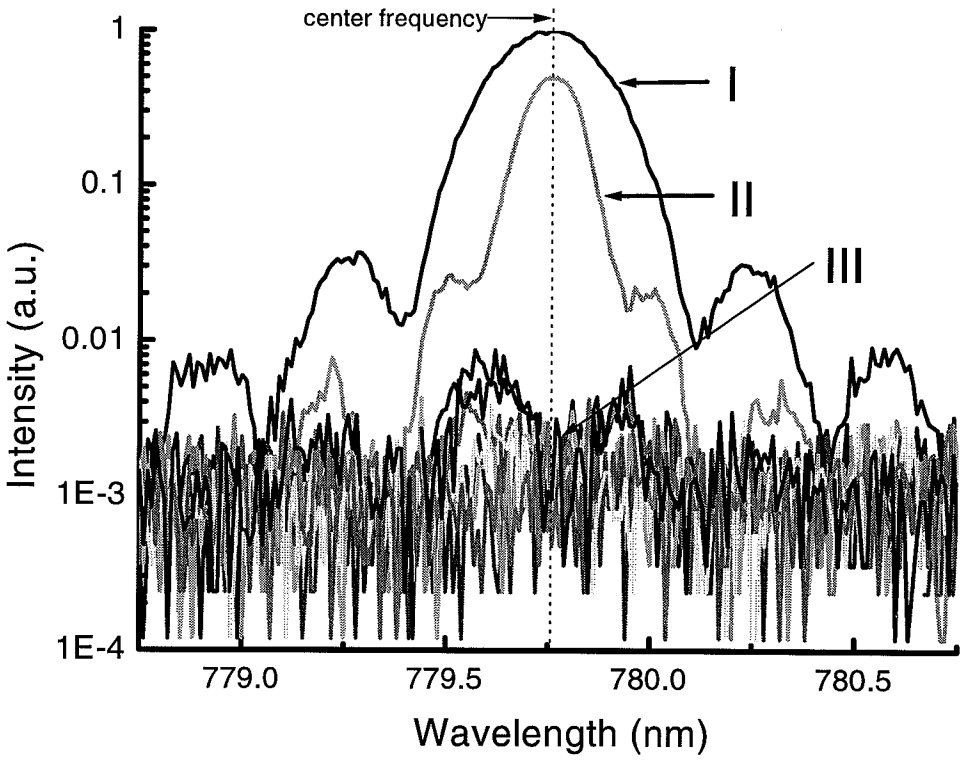

Fig. 4.10. SHG spectra measured under different spectral phase coding situations with C_1 and C_2 chosen from length-8 Hadamard codes.
I–no phase code was applied to the pump pulses.
II–the phase codes C_1 and C_2 are the same.
III–data for fixed C_1, for all choices of $C_2 \neq C_1$.

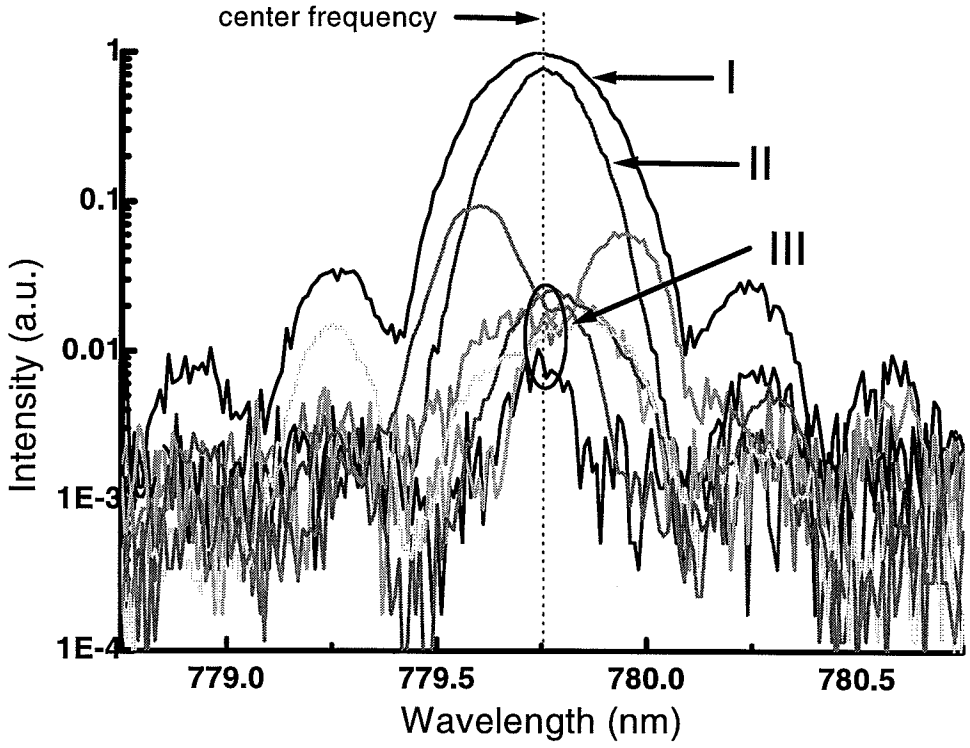

Fig. 4.11. SHG spectra measured under different spectral phase coding situations with C_1 and C_2 chosen from length-7 M-seq codes.
I–no phase code was applied to the pump pulses.
II–the phase codes C_1 and C_2 are the same.
III–data for fixed C_1, for all choices of $C_2 \neq C_1$.

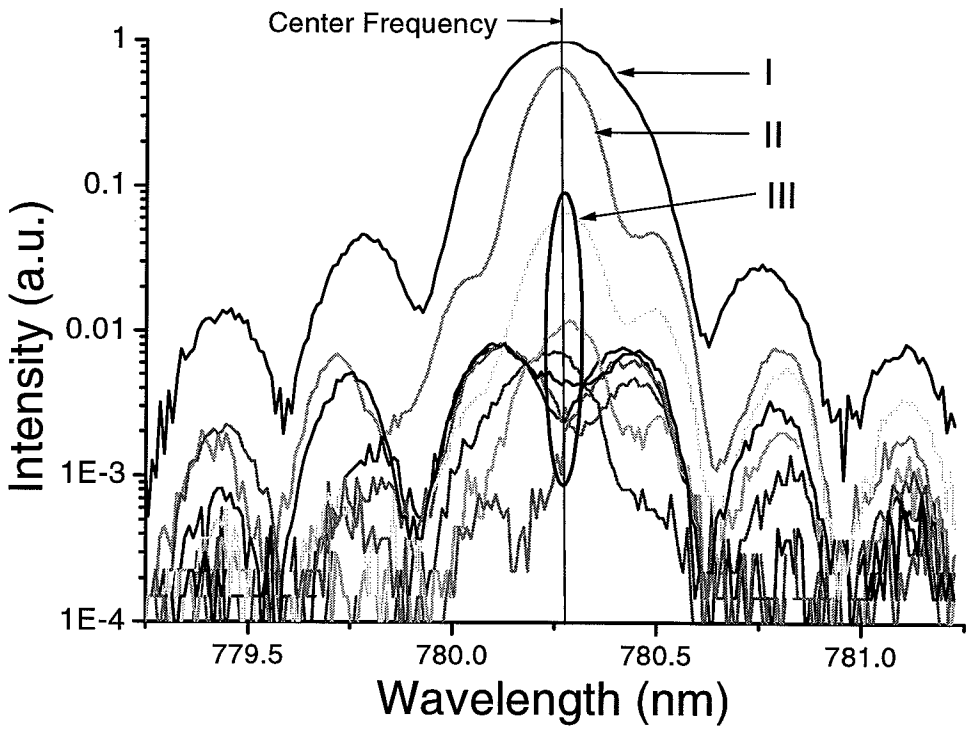

Fig. 4.12. The influence of residual second order spectral phase distortion on the SHG spectra measured under different spectral phase coding situations.
I–no phase code was applied to the pump pulses.
II–the phase codes C_1 and C_2 are the same.
III–data for fixed C_1, for all choices of $C_2 \neq C_1$.

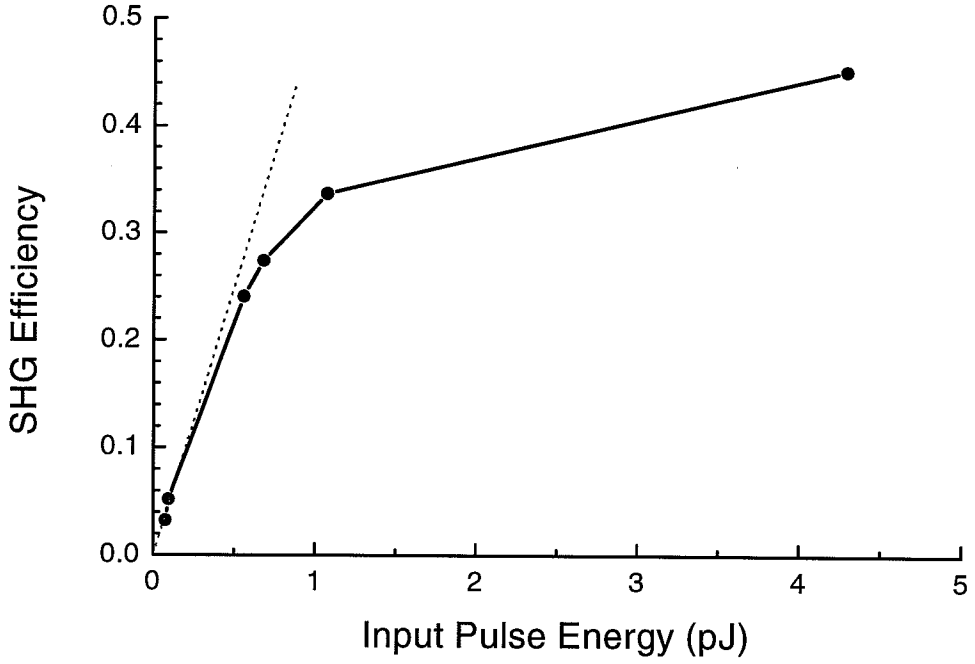

Fig. 4.13. Internal SHG conversion efficiency vs. internal input pump pulse energy. The dotted line is the 50%/pJ line.

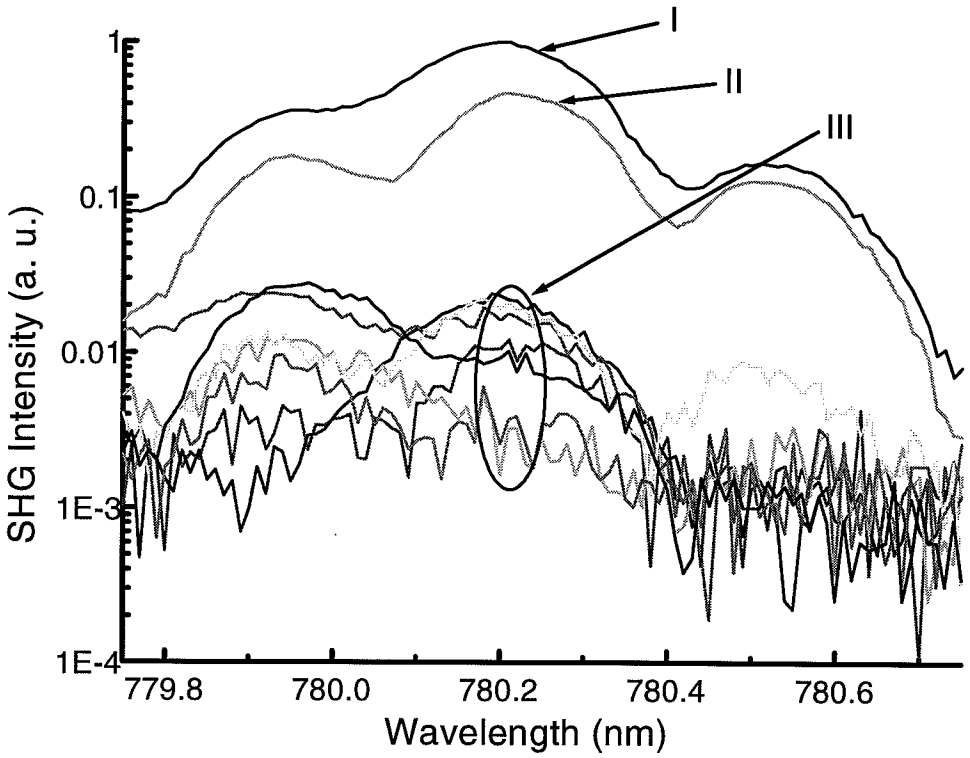

Fig. 4.14. SHG spectra of PPLN waveguides measured under different spectral phase coding situations.
I–no phase code was applied to the pump pulses.
II–the phase codes C_1 and C_2 are the same.
III–data for fixed C_1, for all choices of $C_2 \neq C_1$.

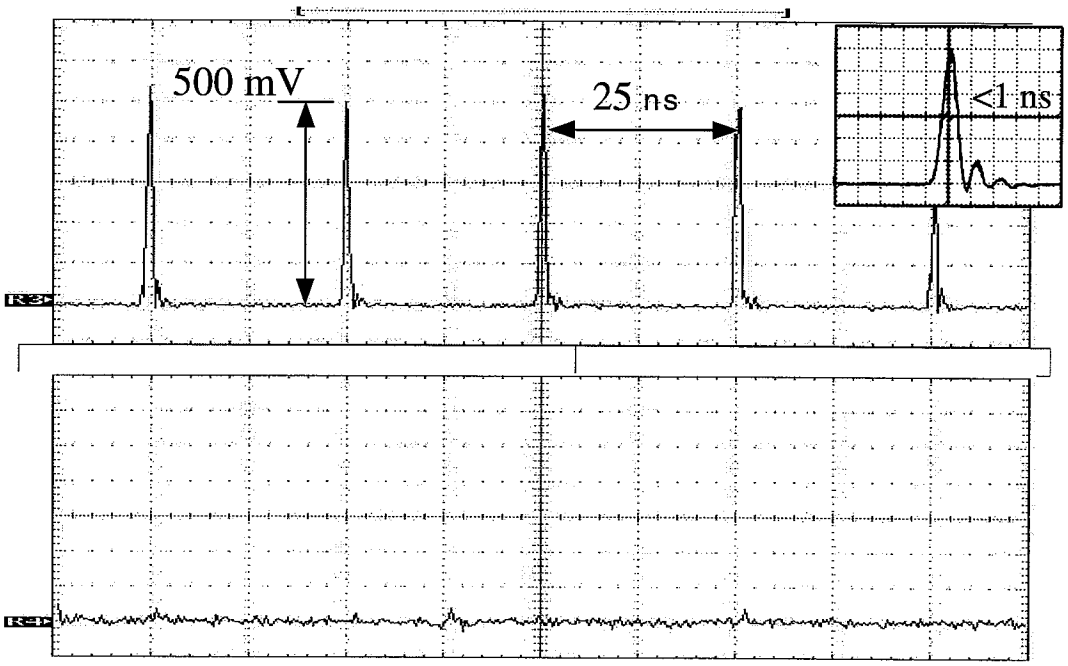

Fig. 4.15. SHG signals measured by a photodetector under different spectral phase coding situations. Top: matched phase codes ($C_1 = C_2$). Bottom: unmatched phase code ($C_1 \neq C_2$).

5. SHG OF FEMTOSECOND PULSES IN THICK CRYSTAL UNDER LARGE CONVERSION EFFICIENCY CONDITIONS

In our previous experimental studies of SHG in thick PPLN crystals in Chapter 4, the experiments were carried out mostly under the low pump power condition. However, because of the high conversion efficiency we observed with the PPLN waveguide device, one could expect a high pump depletion ratio at rather small average pump powers, like hundreds of microwatts.

Even though SHG had been extensively studied since the 60's, the parameter range that we are studying here had been left relatively unexplored. The early studies on the SHG phenomenon of high power short optical pulses are mostly theoretical [53, 54, 59, 58], until the availability of high power femtosecond lasers in the 80's. For example, the saturation of SHG powers and the distortion of pump and SH pulses are studied under hypothetical conditions with strong GVD in [59]. Picosecond pulse SHG was simulated considering a small effect of GVM and GVD [58]. Even though effects like the GVM, GVD and SPM are included in some of those theoretical studies, there had been little corresponding experimental studies. When these effects are considered, analytical solutions are impossible to find in most cases. Numerical studies are needed, and their results can be vastly different depending on the parameters used [59, 58]. Therefore, those early works can not provide strong guidance to the current experimental work, because of the different parameter ranges involved.

The development of highly efficient nonlinear materials, like nonlinear PPLN waveguides, gives us the opportunities to study these effects. However, experimental short pulse SHG studies had been mostly focused on the cases of little GVM [81] with

the goal of generating short SH pulses, and long crystals are mostly used in CW SHG studies [83].

Besides the studies of SHG process, more recently, another interesting related development is in the area of cascaded $\chi^{(2)}$ effects. Lots of efforts had been made to theoretically model this phenomenon [84, 85] originated from a not-phase-matched parametric process in $\chi^{(2)}$ medium. Short pulse propagation in a SHG crystal in a close-to-phase-matching configuration had been studied in [86, 87]. Nevertheless, in those cases, the power conversion to SH signals are generally small and considered deleterious.

Realizing high overall conversion efficiency can be of some significance for short wavelength generation applications. Another potential application based on high depletion of the pump pulse in an SHG process is a proposed optical add-drop multiplexer (ADM) for the optical CDMA system. It is based on an idea similar to that presented in earlier chapters on the optical spectral correlator. The function of an ADM is to add or extract a specific channel of data into or from the main data stream in the network without affecting other transmitted channels. Because of the asynchronous nature of the CDMA system, there had been no proposed scheme to realize this function for the ultrashort pulse CDMA system.

Here we notice that the SHG process in long nonlinear crystals could possibly realize two functions simultaneously, e.g. distinguishing the properly and improperly decoded pulses by generating vastly different amount of SHG signals, and efficiently converting the properly decoded pulse into shorter wavelength (and therefore deplete or drop pulses in that channel).

The setup of such a dropping multiplexer would consist of two pulse shapers and a long SHG crystal, as shown in Fig. 5.1 [88]. The input is decoded by the first pulse shaper by applying a phase code $C_2(\omega)$, then the light is sent to the crystal, which converts the properly decoded pulses efficiently into the SH wavelength while leaving other channels nearly intact. After the SHG signal is separated, the remaining fundamental light is coded by the second pulse shaper with a function $C_2^*(\omega)$, so that

all the spectral phase functions of the rest channels are restored and the pulse streams can be sent into the network again.

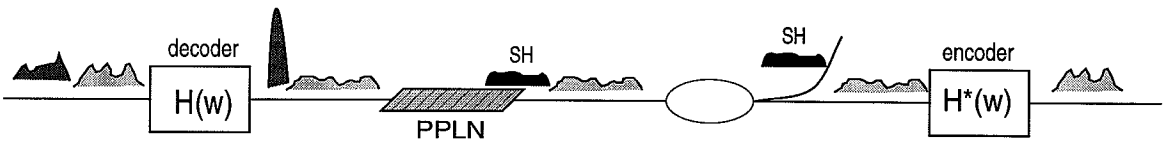

Fig. 5.1. Scheme of proposed add-drop multiplexer for CDMA systems.

In the previous chapter, we experimentally demonstrated that the optical spectral correlator can generate significant amount of SHG for the correctly decoded optical inputs while generating nearly no SHG for the incorrectly decoded input, under the small signal condition. In addition, our proposed ADM scheme would also require a high depletion of the pump pulse when they are correctly decoded.

The questions we would like to address in this chapter is whether it is feasible to achieve close to 100 % conversion efficiency for properly decoded pulses; if feasible, at what kind of power level; if not, what are the limiting factors. Our results given in this chapter will show that the SHG efficiency can be saturated at levels significantly lower than 100 %. Here we'd like to comprehensively study this effect experimentally and theoretically and understand the factors that limit the SHG efficiency under our experimental conditions.

5.1 Experimental Studies

Since we had demonstrated in the previous chapter that the SHG efficiency for the correctly decoded pulses could be similar to the uncoded pulses, in our experiments, for simplicity, we used uncoded femtosecond pulses.

Our experiments used femtosecond pulses around 1560 nm wavelength from the OPO (also used in Chapter 2). Around 1560 nm, the pulsewidth was $\sim$ 200 fs and the spectral bandwidth was $\sim$ 12 nm. The beam was split into two, and one part is focused into the PPLN waveguide. The other part was delayed in free-space and synchronized, and was used as the reference beam for characterizing the fundamental

output from the waveguide. First, we set the temperature of the oven holding the PPLN sample to $\sim 90^o$ C, which gave a phase matching wavelength around 1558.5 nm. The pump center wavelength was tuned to match this wavelength, and the input power was varied as the output power was measured by a power meter. The measured internal pump pulse energy vs. internal conversion efficiency is plotted in Fig. 5.2. The internal values are obtained by considering the Fresnel reflection loss and coupling loss. We can see that the efficiency quickly saturates to about 60% at pulse energy levels above 2 pJ. A small amount of green light generated by a sum frequency generation process between the pump and the second harmonic was also observable under high pump conditions. Also shown in the plot is the theoretical SHG efficiency considering only the SHG process under the large GVM condition (with all other effects ignored). We can see that the experimental results significantly deviate from the theoretical ones when the pump pulse energy is above 2 pJ and saturate much faster. The procedure to obtain the theoretical estimates will be given in the coming section. It is noted that the overall power transmission (e. g. the sum of throughput fundamental power and SHG power) stayed fairly constant within a noise margin, as the pump power increased. The SHG power was measured by a Si power meter. A Ge (Newport 818-IR) power meter was used to measure the fundamental power before and after the crystal. After the crystal, to block the SH beam, a Si filter was used and its reflection loss was considered when we calculated the power. Under such conditions, when the input power was increase from 100 μW to 1.6 mW, the throughput ratio stayed within a 29-32 % range. This may suggest that there is not significant nonlinear loss in the SHG process.

Also we compare the two efficiency curves with other commonly used SHG efficiency curves under different conditions. CW SHG efficiencies under a couple of hypothetical conditions are calculated. In Fig. 5.3, the 'CW-square pulse' curve is the well-known $tanh^2$ curve, which corresponds to the case of a quasi-CW, long square pulse input. The 'CW-Gaussian pulse' curve shows the SHG efficiency under the case of a quasi-CW, long Gaussian-shape pulse input. The two long pulses are assumed to

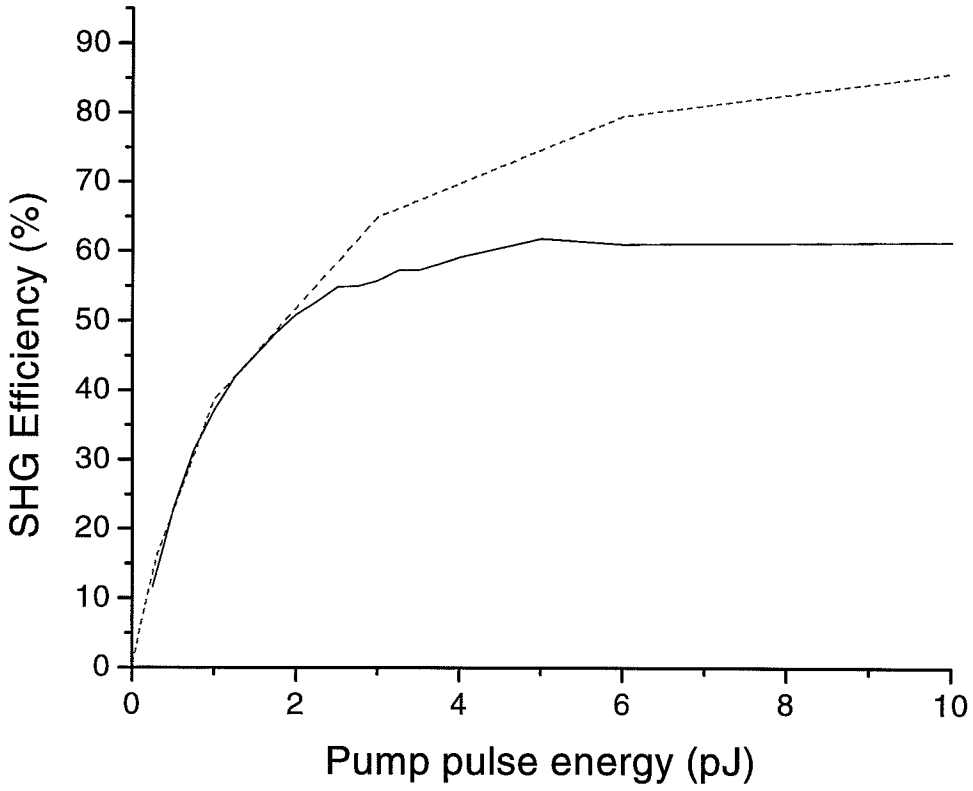

Fig. 5.2. SHG efficiency vs. pump pulse energy. Solid line: experimental result. Dash line: theoretical result.

have the same average power and FWHM width. The unit of the x-axis of the plot is adjusted so that the two sets of results can have the same small signal efficiency slope. Then, we can see that our pulsed data, theoretical and experimental alike, are significantly different from the CW SHG saturation curves. In order to study the potential factors that cause this saturation phenomenon, we managed to further characterize the output optical signals from the nonlinear material, in order to get insight into the physical processes within. First, we measured the pump spectrum exiting the SHG sample using an optical spectrum analyzer (OSA). In Fig. 5.4, the fundamental spectra measured under low and high power conditions are shown. In this case, the phase matching wavelength is at the center of the pump spectrum. We can see that, as the pump power increases, the pump spectrum is no longer symmetric, and shorter wavelength side is more significantly suppressed around 1554 nm. First there is a 'shoulder', and then a spectral 'hole', as the power increases. Also large side lobes compared to the original pump spectrum are also observable. As the SHG process was phase matched at the center of the pump spectrum, the explanation for this asymmetric pump spectrum depletion is not readily available from the SHG process itself. This clearly indicates the involvement of other physical processes.

For a fixed $\sim$ 1558.5 nm phase matching wavelength (at a temperature of about 90 degrees), the input pump wavelength was tuned, while the input power was kept at about 10 pJ. As shown in Fig. 5.5, the pump spectrum is significantly distorted at this power level as long as its center wavelength is no more than $\sim$ 6 nm away from the phase matching wavelength. We also did the similar measurements under different phase matching temperatures. For example, the phase matching temperature was tuned to $\sim$ 120 degrees, which shifted the phase matching wavelength to $\sim$ 1561.5 nm. The output pump spectrum was measured at different input center wavelengths (as shown in Fig. 5.6). Comparing to Fig. 5.5, the measured spectral features in Fig. 5.6 are very similar but shifted by the same amount corresponding to the shift in the phase matching wavelength. The large 'fringes' in the spectrum in Fig. 5.6 were caused by double reflections in the setup. This suggests that the spectral distortion

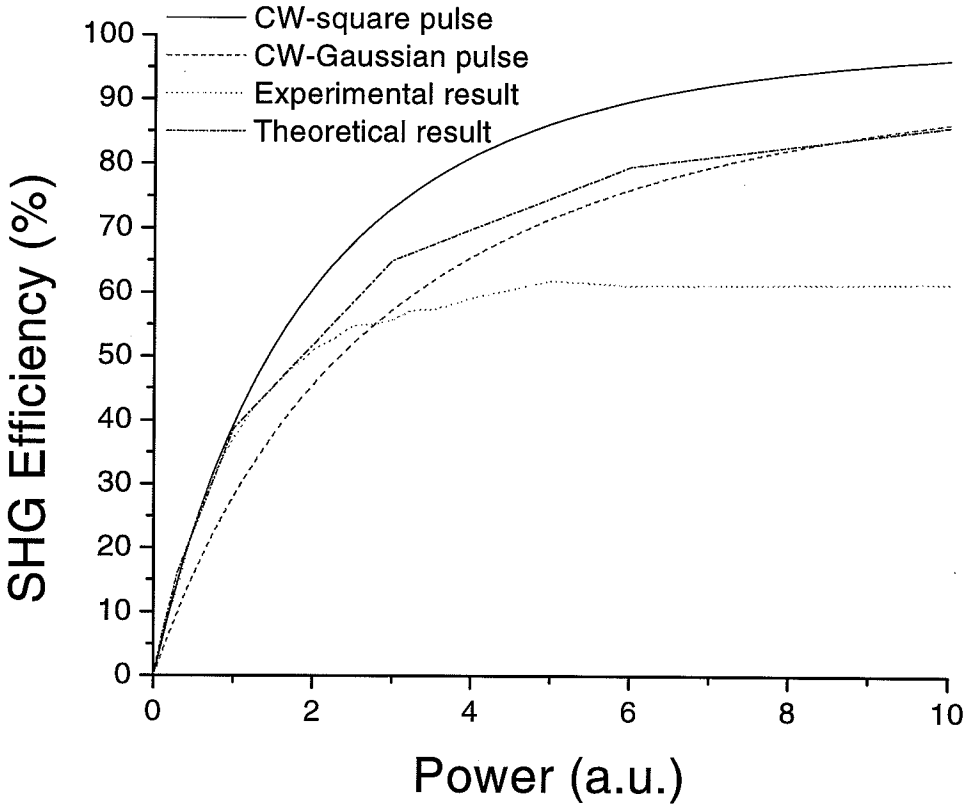

Fig. 5.3. Comparison of different SHG saturation curves.

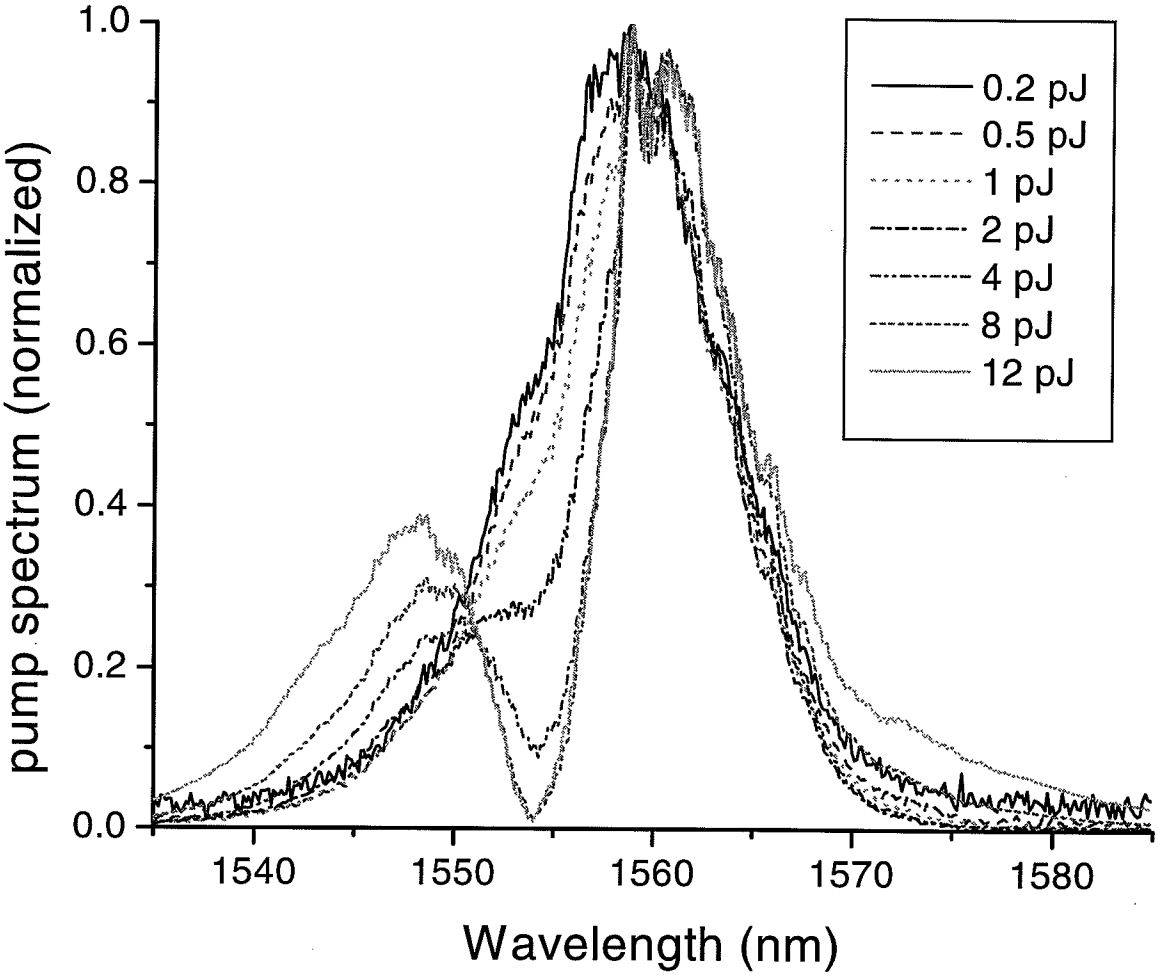

Fig. 5.4. Pump spectrum variation as the pump power increases.

may not be caused by an additional parametric process 'accidentally' phase matched for that specific wavelength. Such a process could deplete the frequency components within a narrow range, but should be quite sensitive to changed phase matching conditions.

The pulseshape of the output pump pulse was measured by field cross-correlation. When the pump wavelength was centered around 1548 nm while the phase matching wavelength was at 1558 nm, the pulse shaper was measured at both low power and high power condition. As shown in Fig. 5.7, there is no significant pulse shape changes under high power conditions. The pulsewidth is also close to the estimation based on the spectral bandwidth. This may indicate that dispersion is not a significant factor here. For the case that the pump is phase matched for the SHG, under low power input, the pulseshape is similar to that in Fig. 5.7. On the other hand, at higher power levels, a double-pulse-like pulseshape was observed under the 10 pJ pump, as seen in Fig. 5.8. This coincides with the occurrence of the spectral 'hole' discussed above.

To completely characterize the pump signal, by using a setup that was similar to the used used to do the field cross-correlation measurements, I carried out spectral interferometry measurements for the pump output, in order to retrieve the spectral phase information. When the pump spectrum is centered at the phase matching wavelength, $\sim$ 1558.5 nm, a significant phase jump around the spectral amplitude 'dip' began to emerge as the power increased. Shown in Fig. 5.9, the jump has a magnitude of a couple of radians. The measurements under low power conditions showed no sign of a phase jump in the high power case but small phase variation most likely due to measurement noise from instabilities in the interferometry setup.

We also measured the SHG spectrum using the OSA, which had a spectral resolution of $\sim$ 0.08 nm. As seen in Fig. 5.10, at low input powers, the SHG spectrum had a FWHM bandwidth of $\sim$ 0.3 nm and the curve had a longer and oscillating tail on the short wavelength side. Based on the GVM parameter and the length of the sample, the ideal SHG tuning curve should have a $sinc^2$ shape with a FWHM less

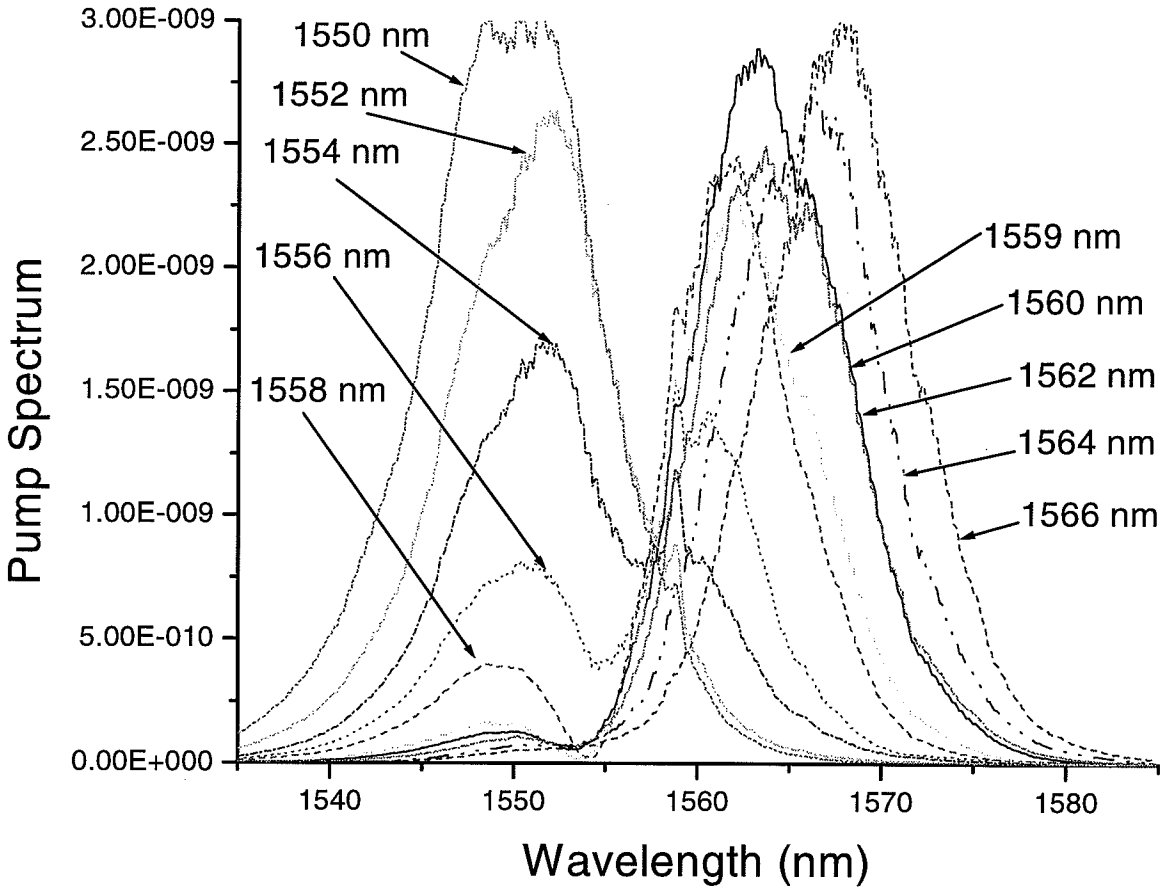

Fig. 5.5. Output pump spectrum under high power conditions, as the center wavelength is varied. The labels show the center wavelengths of the input pump spectrum

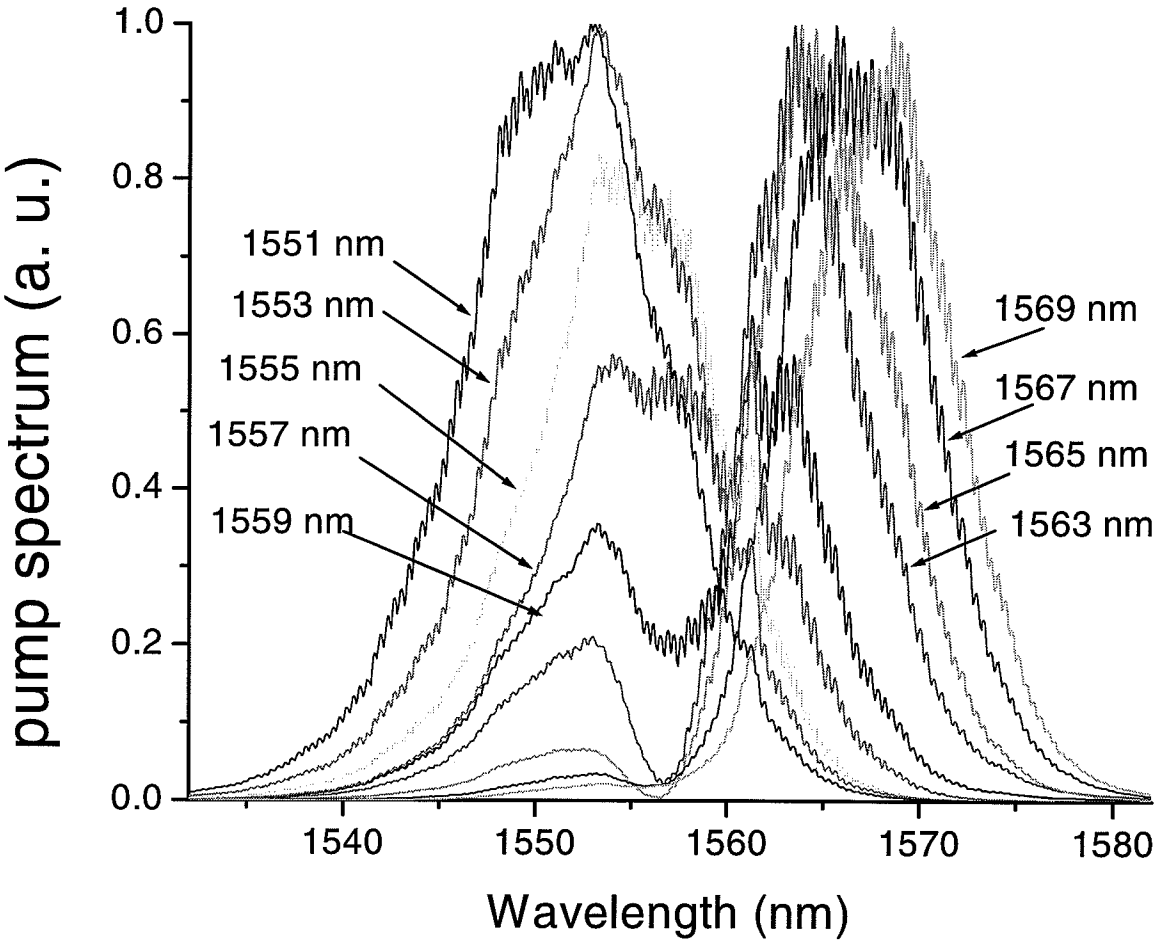

Fig. 5.6. Output pump spectrum under high power conditions, as the center wavelength is varied. The phase matching wavelength is different from that in Fig. 5.5. The labels show the center wavelengths of the input pump spectrum.

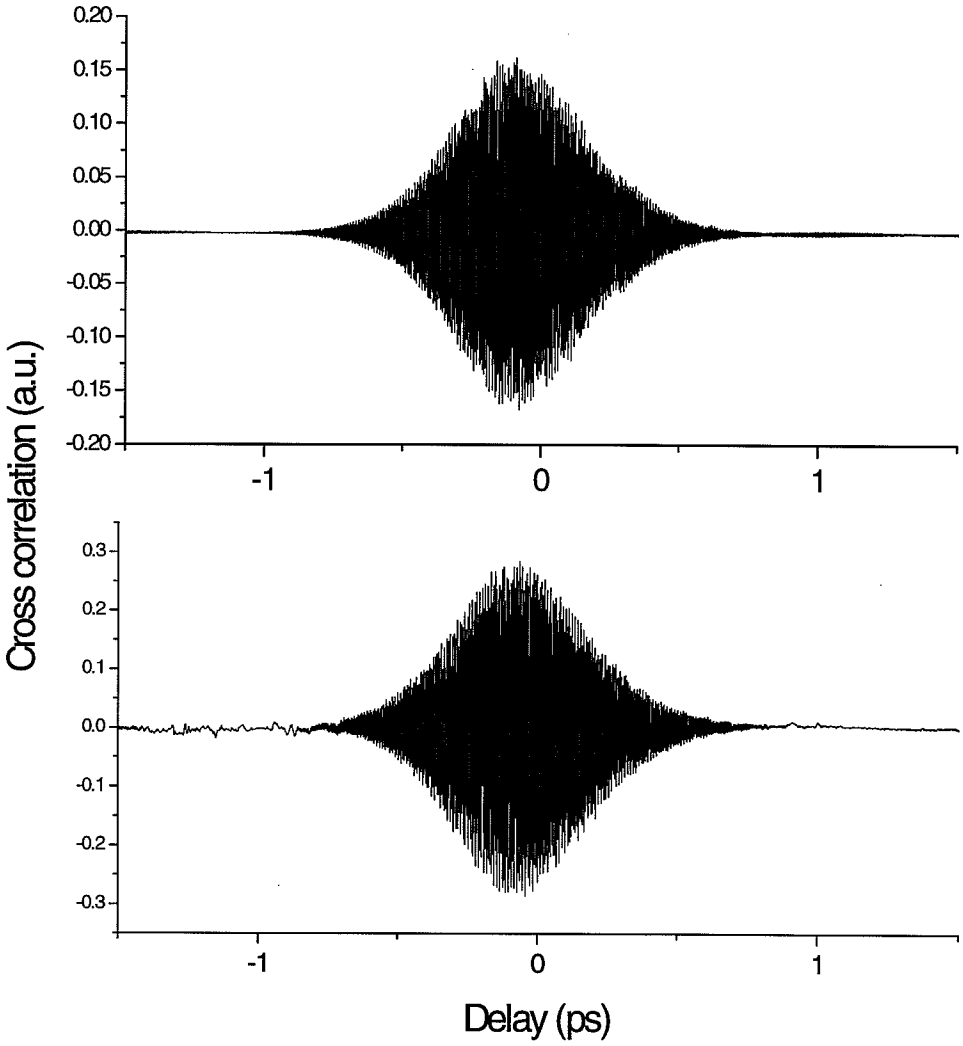

Fig. 5.7. Pump pulse temporal shape when it is not phase matched for SHG. Top: at 0.5 pJ power level, bottom: at 10 pJ power level.

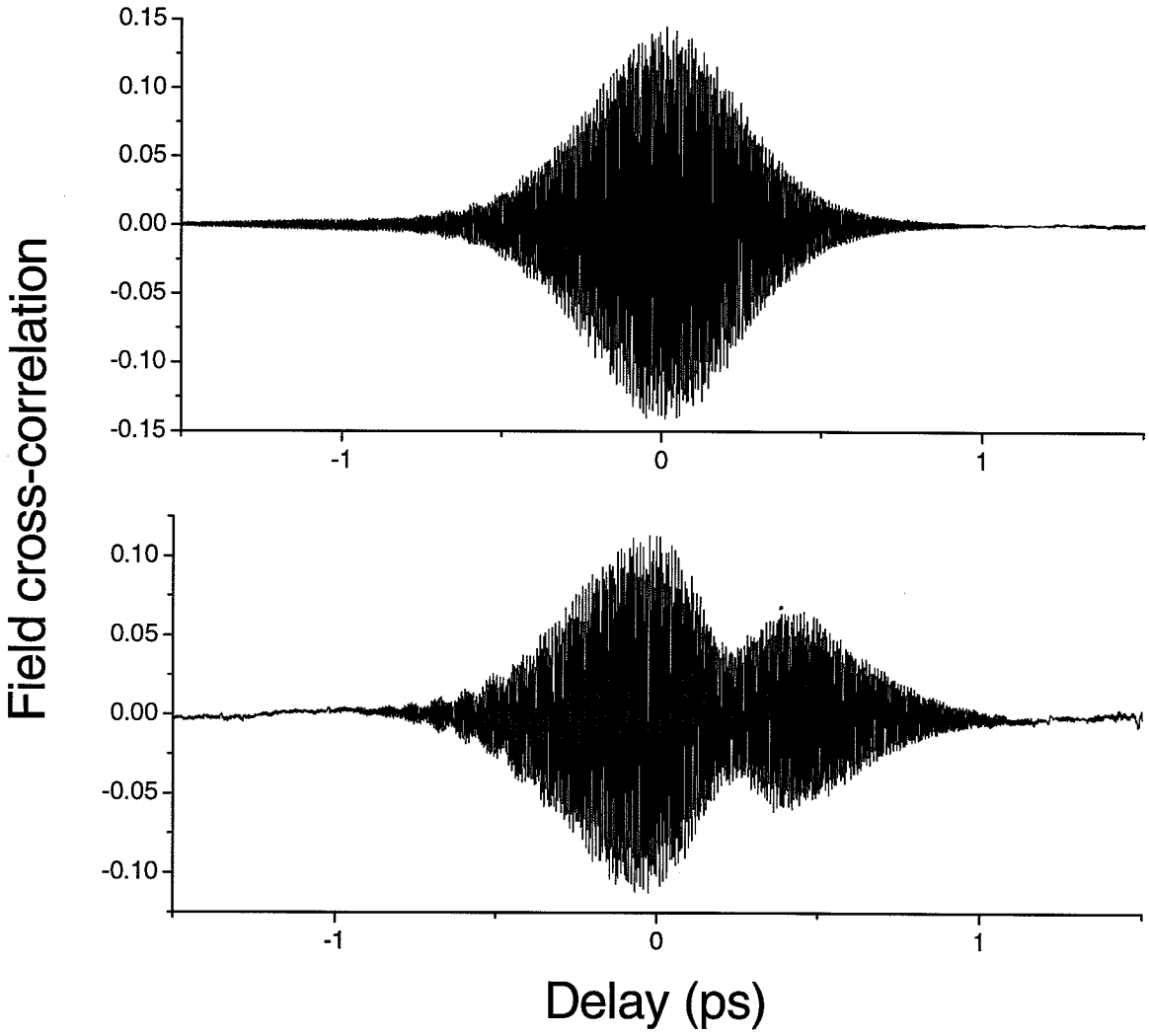

Fig. 5.8. Pump pulse temporal shape when it is phase matched for SHG. Top: at 0.5 pJ power level, bottom: at 10 pJ power level.

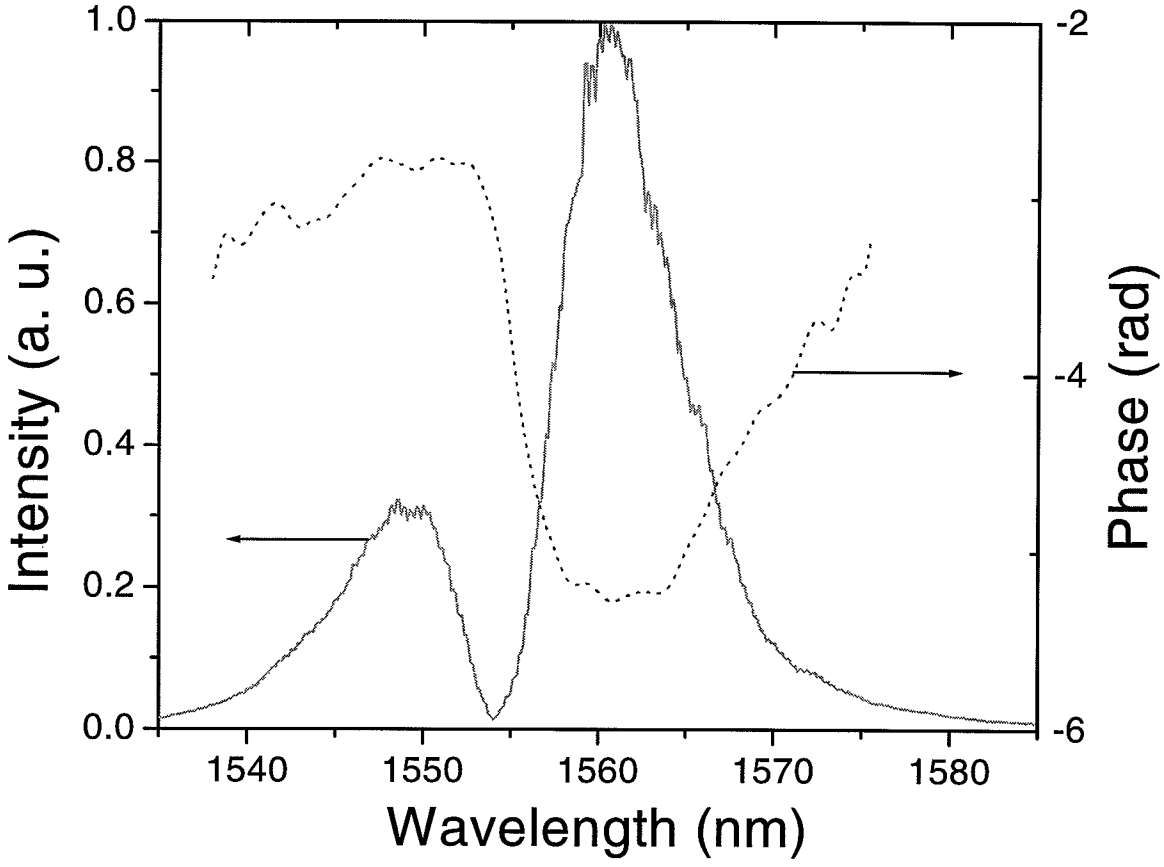

Fig. 5.9. Spectral phase curve of the pump under the phasematched and large input condition. Measured at $\sim$ 10 pJ power level.

than 0.1 nm. The deviation from the ideal value may be caused by inhomogeneities in the device structure and/or nonuniform temperature distribution in the PPLN oven. We will address this issue further in the following section.

At high pump powers, the SH spectrum also changed. Shown in Fig. 5.11 are the SH spectra measured under 0.5 pJ and 10 pJ pump pulse energies, respectively. We can see a increasingly larger 'tail'.

After we carefully characterized the output signals from the SHG process, we numerically solved the coupled SHG equation described in Chapter 3. The goal is to adjust the parameters in the equations in order to match the experimental results, so that we could learn more about the interaction of various nonlinear processes inside the waveguide.

5.2 Theoretical and Numerical Studies

First, let's reformulate the Eq. 3.12 and 3.13 into a form that is suitable for simulation. We take a transform $\tau = t - z/v_{g,2}$ and the two equations become:

$$\begin{aligned}\frac{\partial A_1}{\partial z} + (\frac{1}{v_{g,1}} - \frac{1}{v_{g,2}})\frac{\partial A_1}{\partial \tau} - \frac{j}{2}\beta_{2,1}\frac{\partial^2 A_1}{\partial \tau^2} &= -j\frac{2\omega_0^2}{k_{1,0}c^2}d(z)A_2A_1^*\exp(-j\Delta k_0(z)z) \\ &- j\frac{n_2 k_{1,0}}{n_0}(|A_1|^2 + 2|A_2|^2)A_1 - \frac{\alpha_1}{2}A_1 \quad (5.1)\end{aligned}$$

$$\begin{aligned}\frac{\partial A_2}{\partial z} - \frac{j}{2}\beta_{2,2}\frac{\partial^2 A_2}{\partial \tau^2} &= -j\frac{2\omega_0^2}{k_{1,0}c^2}d(z)A_1^2\exp(j\Delta k_0(z)z) \\ &- j\frac{n_2 k_{2,0}}{n_0}(|A_2|^2 + 2|A_1|^2)A_2 - \frac{\alpha_2}{2}A_2 \quad (5.2)\end{aligned}$$

where α_1 and α_2 are the linear loss of the material. Although experimentally we did not observe very strong GVD effects, they are included for the completeness of the theory.

The method of numerical simulation is based on the Split-Step Fourier (SSF) method [89]. Here, to increase the calculation accuracy, I used the symmetrized SSF method [89]. The interaction length is equally divided into a large number of small segments. Within a segment $[z, z+\Delta z]$, the pump and SH pulses are first propagated for a distance of $\Delta z/2$ with only GVM and GVD. These terms are solved in the

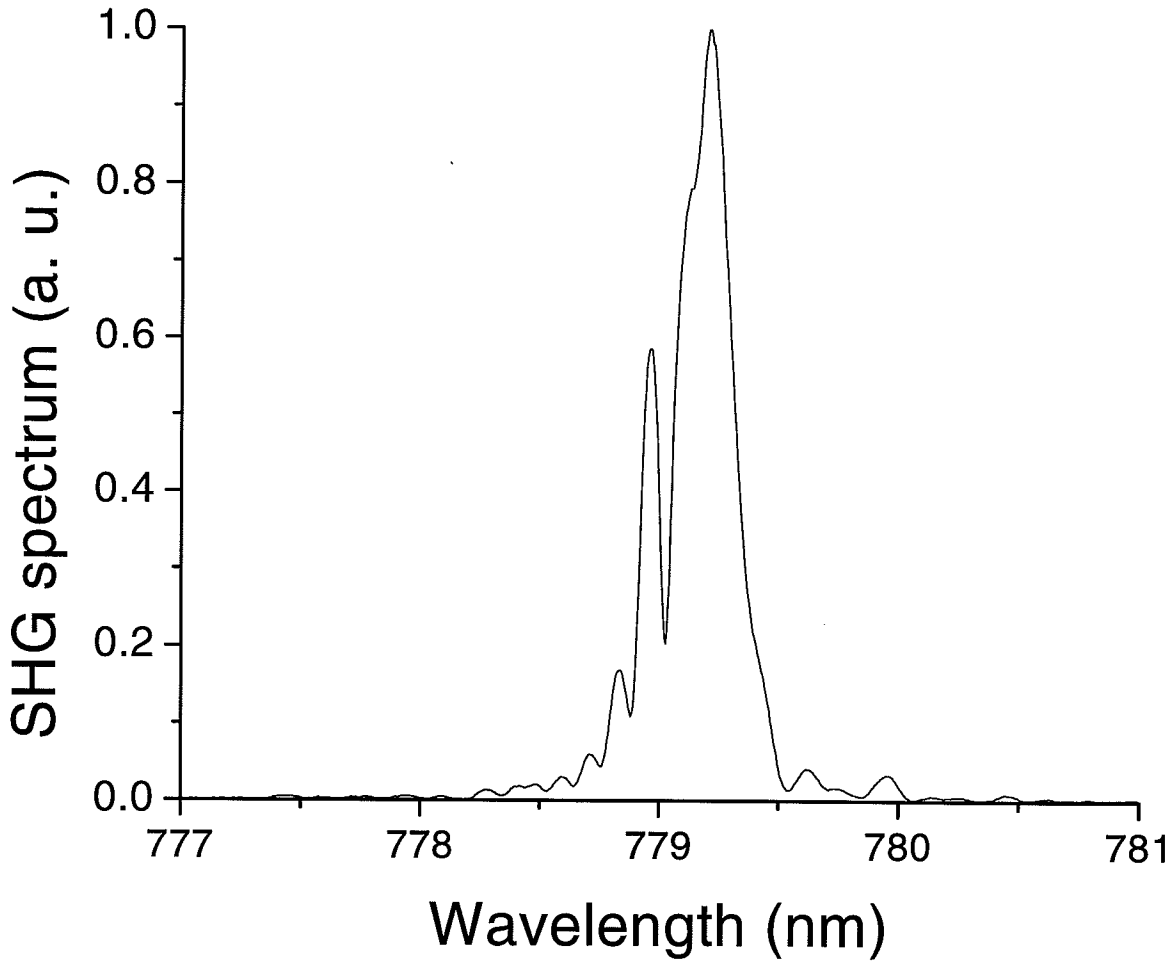

Fig. 5.10. SH spectrum shape under low pump conditions.

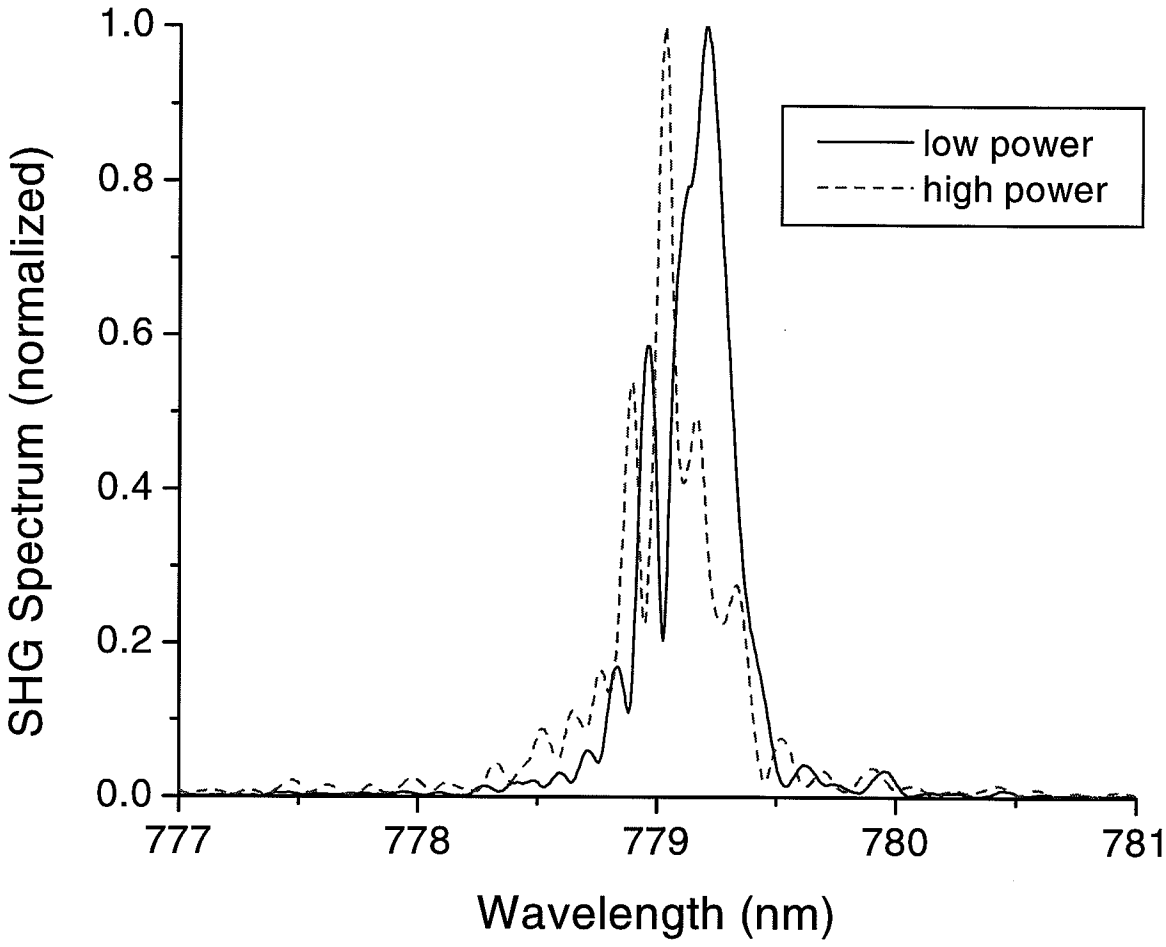

Fig. 5.11. SH spectrum shape under different input pump powers.

spectral domain. Then the nonlinear effects over the entire segment are calculated in the time domain. Similar to other coupled propagation equations, like those for cross-phase modulations [90], the equations can be solved by assuming the coupled terms are nearly constant within one calculation step. Finally, the pulses are propagated for another distance of $\Delta z/2$ with only GVM and GVD.

To further improve the accuracy of the SSF method, I used the approach described in [89] to calculate the nonlinear effects. The trapezoidal rule is used to evaluate the integral of the nonlinear terms over the length Δz. Since the values of $A_1(z+\Delta z)$ and $A_2(z+\Delta z)$ are initially unknown, an iterative method is used. First, intermediate values of $A_1(z+\Delta z)$ and $A_2(z+\Delta z)$ are calculated based on $A_1(z)$ and $A_2(z)$. Then, the final result of $A_1(z+\Delta z)$ and $A_2(z+\Delta z)$ are solved using both the $A_i(z)$ and the intermediate value of $A_i(z+\Delta z)$. With some additional calculation time for each step, this process can increase the accuracy of the simulation and eventually reduce the overall simulation time [89].

Here we consider a uniform nonlinear material, so that $d(z)$ is a constant throughout the material. In fact, what we used in the experiments are periodically poled materials. Their $d(z)$ is a periodic function of z. For the first order QPM, we can consider it as a nonlinear material with $d_{eff} = 2d/\pi$. However, based on our experimental observation, the $\Delta k_0(z)$ term may not be a constant. As, in our experimental setup, it is difficult to maintain an exactly uniform temperature distribution across the whole waveguide, such a distribution can change the local quasi-phase matching wavelength. This effectively gives a nonuniform Δk. One more complication arises when $\Delta k \neq 0$, and, for the step $[z, z+\Delta z]$, the contribution of SHG effect are given by:

$$-j\frac{2\omega_0^2}{k_{1,0}c^2}d_{eff}A_1^2(z)\exp(j\Delta kz)\exp(j\Delta k\Delta z/2)sinc(\Delta k\Delta z/2)\Delta z \tag{5.3}$$

$$-j\frac{2\omega_0^2}{k_{1,0}c^2}d_{eff}A_2(z)A_1^*(z)\exp(-j\Delta kz)\exp(-j\Delta k\Delta z/2)sinc(\Delta k\Delta z/2)\Delta z \tag{5.4}$$

which are functions of z.

Also note that the n_2 used in the simulation is given in the unit of m^2/W instead of

m^2/V^2 as in the previous chapters, just to be in conformity with the normal definition in literatures, as explained in [89]. Also for the waveguide problem we are trying to address, the SHG coupling coefficient needs to be modified to include the effect of mode coupling between the fundamental and SH beam. A spatial integral over the product of the mode transverse profiles $E_{\omega}^{2}(x,y)E_{2\omega}^{*}(x,y)$ needs to be included, which is normally given as the inverse of the square root of the overlap area of the two modes. The field terms for the SHG process are adjusted accordingly to be proportional to the power.

The correct selection of the calculation step size is important to ensure reliable results. This is verified in my simulation process, by reducing the calculation step size until there is minimal changes on the simulation results.

The simulation program was written in Matlab, and no special efforts had been spent to optimize the speed of the program. A calculation step of $10\mu m$ would guarantee a reliable result, under the current conditions. Using a Pentium III 900 Hz PC, the simulation time would be around 45 minutes.

The parameters used in the simulation were decided in this way: Some of them, like material index, GVM parameter and waveguide parameters are known with little uncertainty. Some of them, like GVD, are not well known for the waveguide devices, but within a reasonable range. For those parameters that are crucial to the simulation and unknown, we adjusted their value repetitively to match the experimental results.

To match the simulation results to the experimental ones, first the SHG coefficient was slightly adjusted to match the small signal SHG efficiency. This also takes into account small device imperfections that reduce the SHG efficiency from its ideal value. The other effects we discuss later have relatively insignificant effect on the small signal SHG efficiency.

Since our observed SHG spectra show a shape significantly different from a $sinc^2$ shape, the phase matching condition or the nonlinear medium obviously deviate from a uniform one. We try to model the temperature distribution and the waveguide variance by incorporating a varying effective temperature profile $\Delta T(z)$, which results

in the Δk distribution [83]. We adjust the parameters in the following equations to match the low power SHG spectrum we measured. The final $\Delta T = \Delta T_1 + \Delta T_2$ is given by [83]:

$$\Delta T_i = \begin{cases} T_{Ni}\left(\frac{z_{ui}-z}{z_{Ni}}\right)^{p_i} & z \le z_{ui} \\ 0 & z_{ui} < z \le z_{oi} \\ T_{Ni}\left(\frac{z-z_{oi}}{z_{Ni}}\right)^{p_i} & z_{oi} < z \end{cases} \tag{5.5}$$

where $z_{o1} = 31mm$, $z_{u1} = 29mm$, $z_{N1} = 10mm$, $p_1 = 4.3$, $T_{N1} = 0.01$, $z_{o2} = 30mm$, $z_{u2} = 30mm$, $z_{N2} = 25mm$, $p_2 = 1.2$ and $T_{N2} = 0.12$. These parameters give a maximum temperature variance of about 1 K. Plotted in Fig. 5.12 are the simulated and experimentally measured SHG spectrum. They match relatively well, while the simulated one has a slightly longer and larger tail on the short wavelength side.

We now only consider the effective Δk effect, the GVM, the intrinsic n_2 from $\chi^{(3)}$ ($\sim 10 \times 10^{-16}\ cm^2/W$) [91] and GVD ($\sim 100\ ps^2/km$) [74]. It was found that the GVD and SPM terms had insignificant effect on the simulation results under our simulation power range (max. $\sim$ 10 pJ). Those key parameters used in the simulation are listed in the following table: Under high power conditions, the SHG conversion efficiencies with Δk are significantly reduced, compared to the curve without this effect (see Fig. 5.13). The output pump pulse shape and its spectrum are shown in Fig. 5.15 and Fig. 5.14 at the power level of 10 pJ. We can see that the pulse shape has some similarities to what we measured experimentally at lower pump powers. However, there are some significant differences: the spectral phase shape doesn't look like the other one measured; and the spectral hole and the temporal second hump are not formed yet.

In order to further fit the simulation results to the experimental ones, we found that adding a 'nonlinear phase shift' (NPM) term for the pump pulse with a large negative coefficient ($\sim -2000 \times 10^{-16}\ cm^2/W$) could significantly change the results. As shown in Fig. 5.13, the simulated SHG efficiency is closer to the measured values. Also shown in Fig. 5.13 is the SHG efficiency when only the large 'NPM' term is added. When the 'NPM' term is considered, the pump spectrum calculated shows a

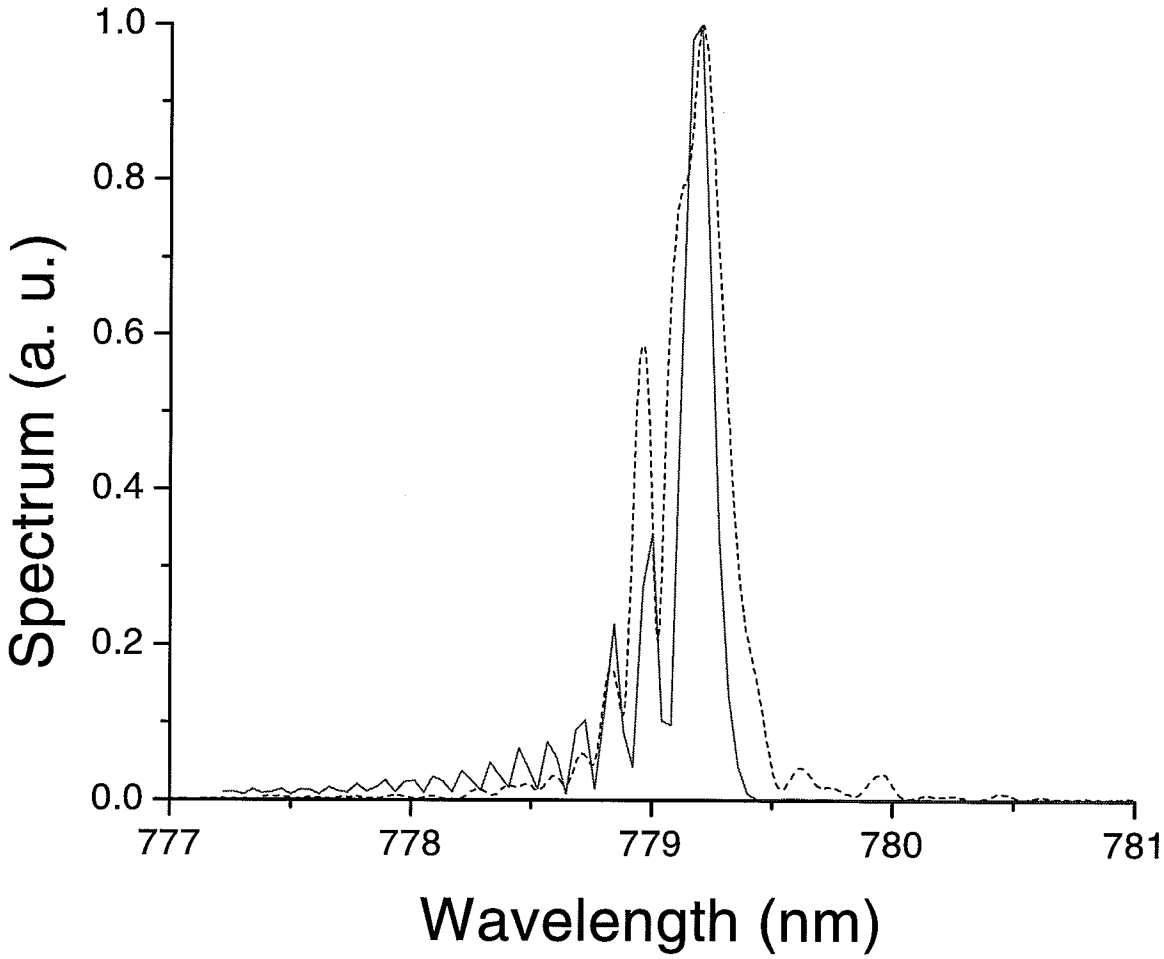

Fig. 5.12. Simulated and experimental SH spectrum under low input power. Solid line: simulation result. Dash line: experimental result.

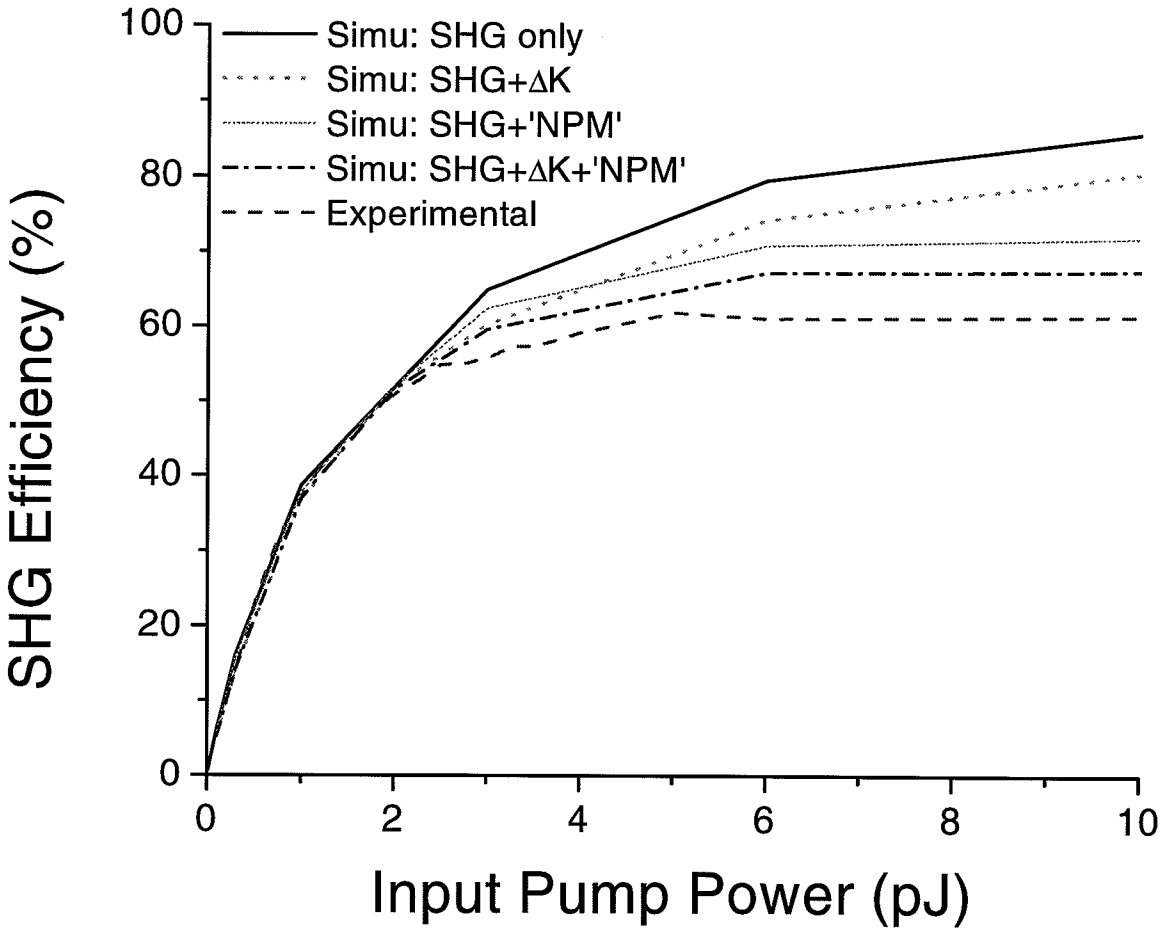

Fig. 5.13. Simulated SH conversion efficiency vs. input pump power, considering the effects of different physical processes.

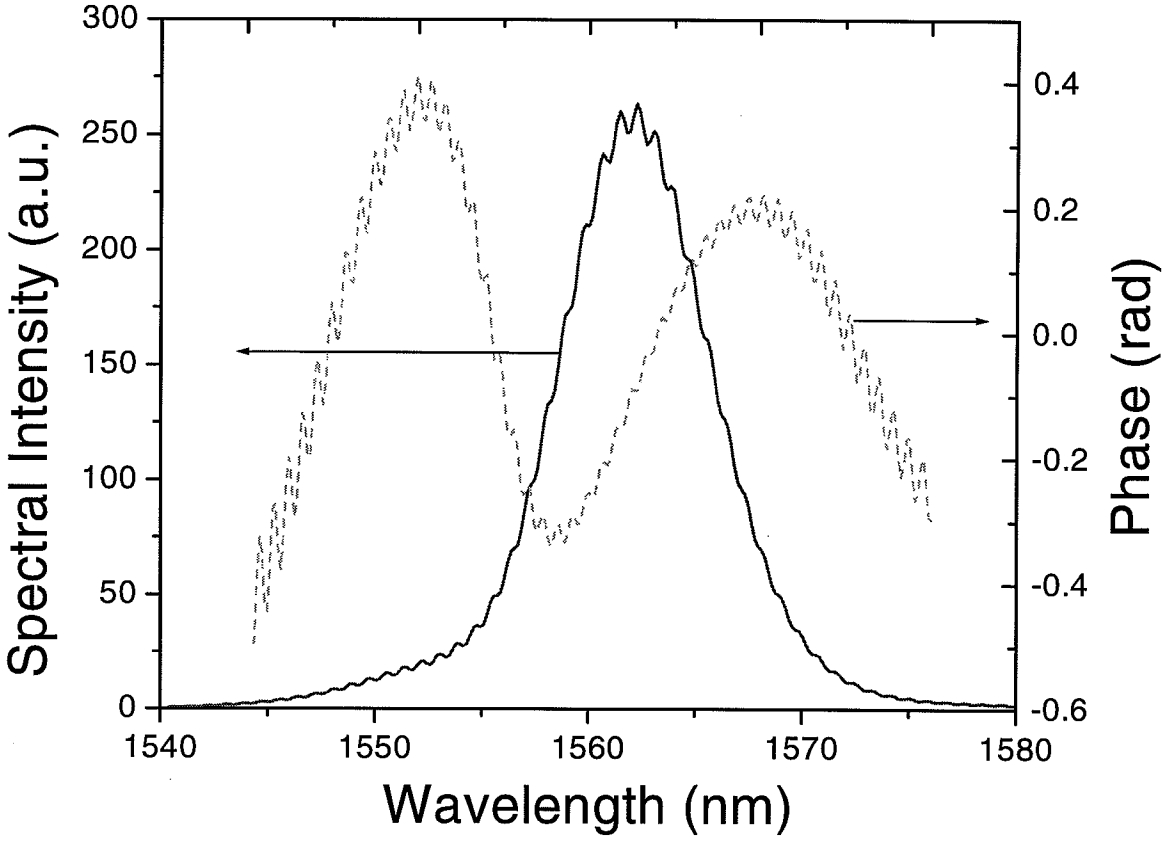

Fig. 5.14. Simulated pump spectrum under 10pJ input power, considering an effective varying phase mismatch.

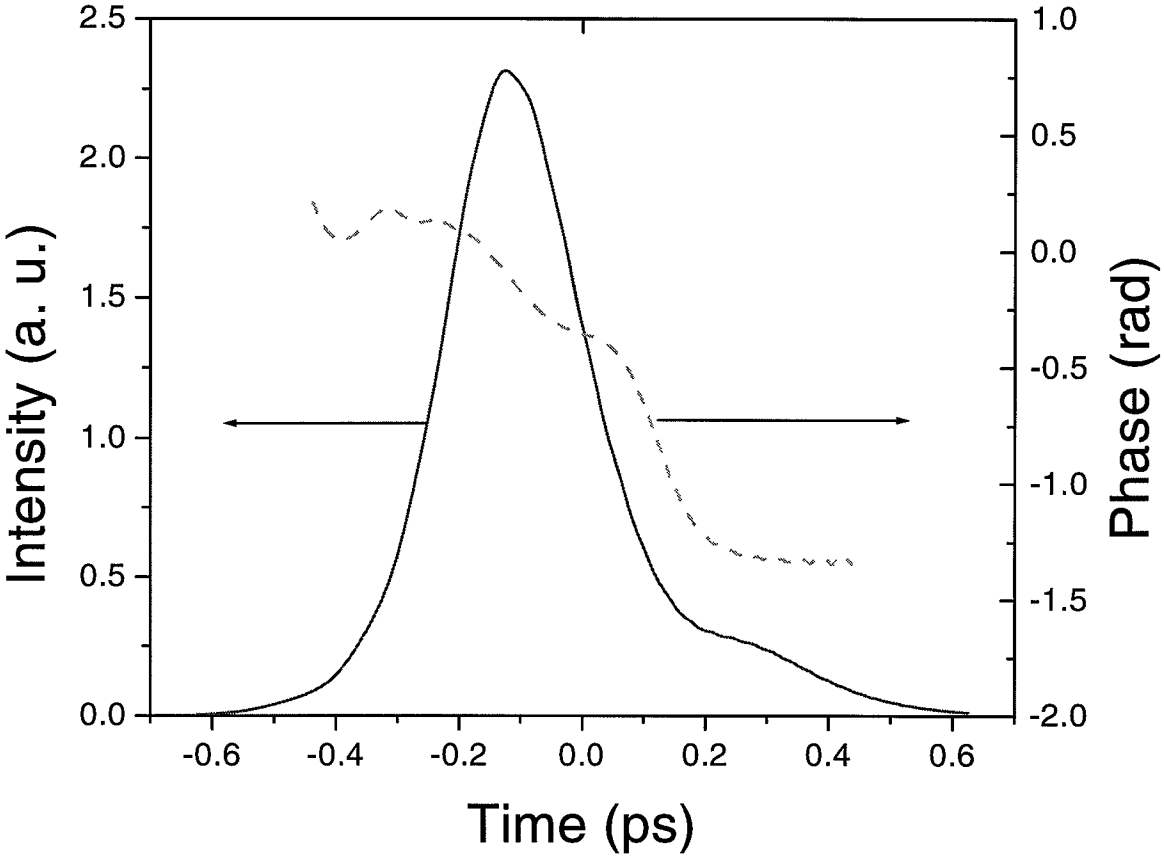

Fig. 5.15. Simulated pump pulse shape under 10pJ input power, considering only an effective varying phase mismatch.

Fundamental mode size	40 μm^2
SH mode size	10 μm^2
Overlap area	53.1 μm^2 [78]
Crystal length	6 cm
refractive index	2.14
α (GVM)	0.37 ps/mm [78]
β_2	100 ps^2/km
Linear loss	0.35 dB/cm [78]
d_{eff}	16.5 pm/V [81] $\times$ 0.5
T_0 of the input pump pulse	140 fs

Table 5.1
Simulation Parameters.

phase jump very similar to what we measured in the experiments (see Fig. 5.16). The temporal pulse shape at 10 pJ pump power is shown in Fig. 5.17. Both the temporal and spectral shapes of the pump pulse at high input power show strong similarities to the experimentally measured ones. However, with only the 'NPM', the calculated SHG spectrum doesn't have the asymmetric shape as shown in the experimental results. The nonuniform phase mismatch distribution is essential to yield that kind of SH spectrum results, and it also has noticeable effects on the SHG efficiency.

We also simulated the cases that the phase matching wavelength doesn't equal the input center wavelength, as those experimental studies (shown in Fig. 5.5). A 10-pJ input pump pulse energy was assumed. Different constant phase mismatches were introduced in the simulation process in order to change the relative difference between the input wavelength and the phase matching wavelength. This is the same as experimentally tuning the input wavelength while keeping the phase matching wavelength constant. As shown in Fig. 5.9, we see the simulation results show similarities to the experimentally observed results. For the cases that corresponds to tuning to longer

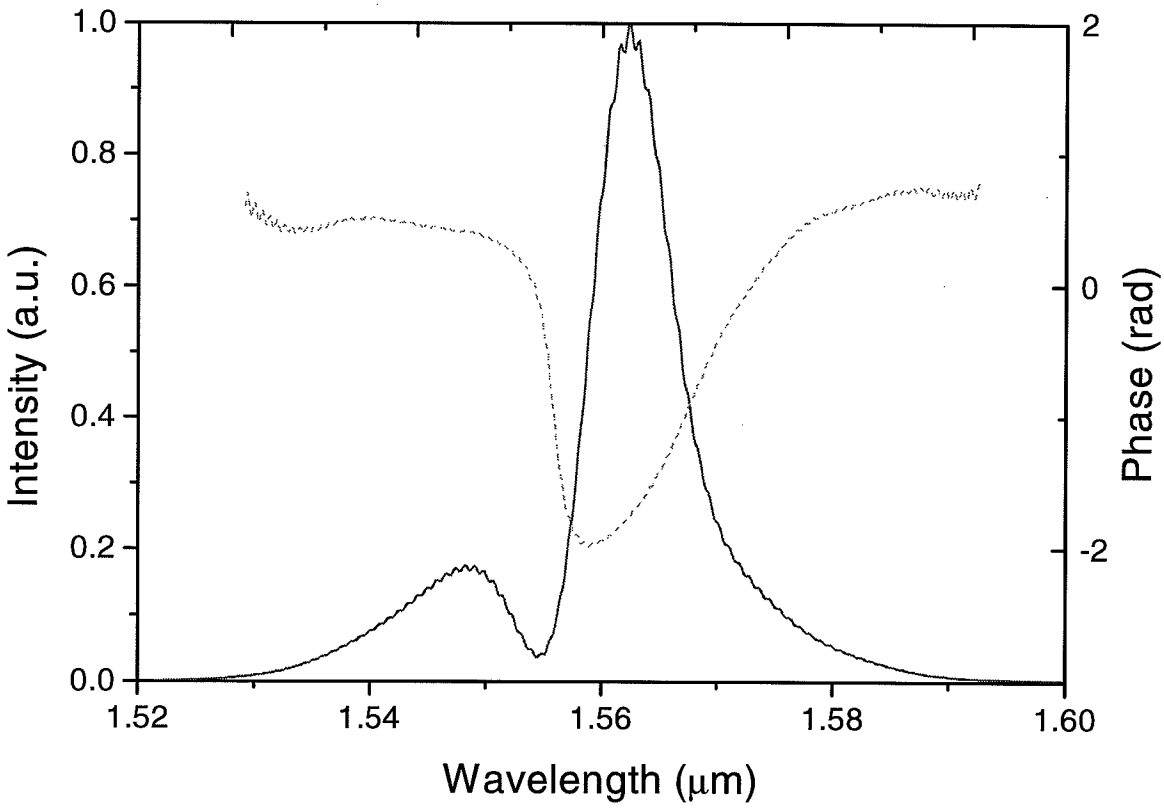

Fig. 5.16. Simulated pump spectrum under 10pJ input power, considering an effective varying phase mismatch and an effective 'NPM' term.

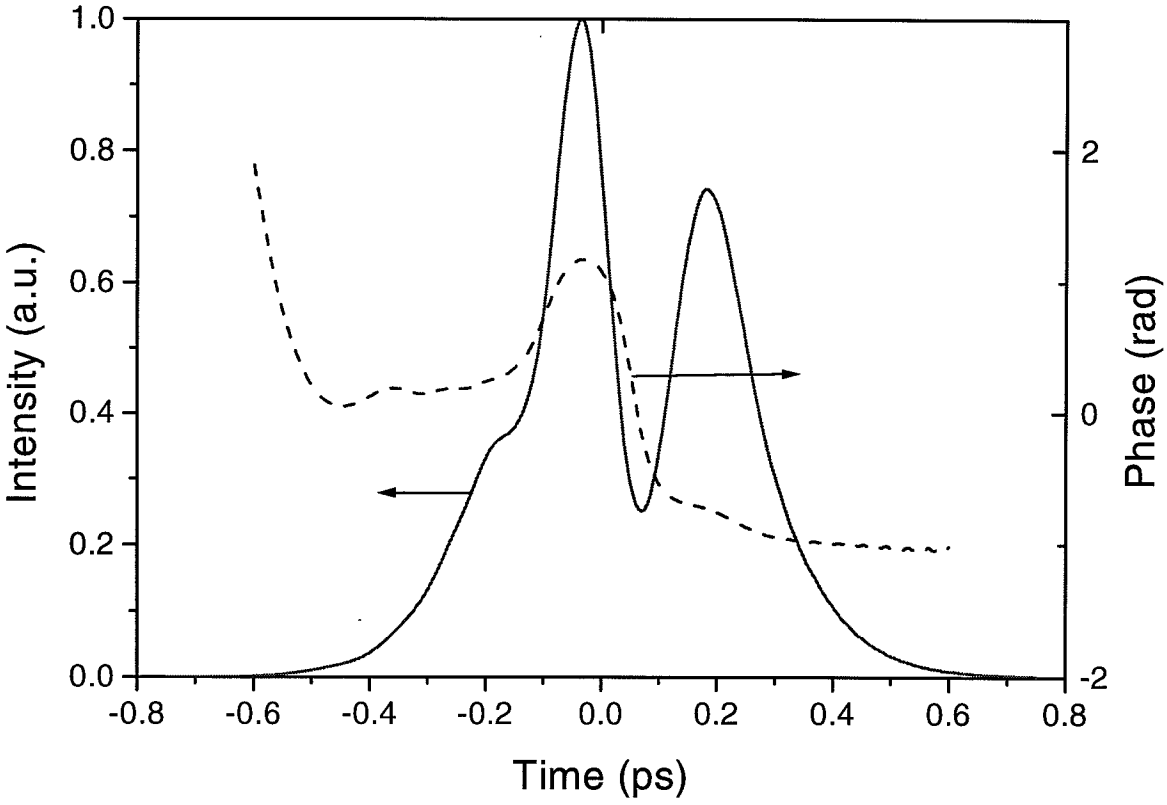

Fig. 5.17. Simulated pump pulse shape under 10pJ input power, considering an effective varying phase mismatch and an effective 'NPM' term.

input wavelengths by a few nanometers, there isn't much spectral distortion. On the other hand, for the cases that corresponds to tuning to shorter input wavelengths, the simulated results qualitatively resemble the experimental ones, while their sidelobes on the short wavelength side are somewhat larger.

To get more insight into what happens to the pump and SH pulse in the nonlinear process, the pulse evolution of the fundamental pulse is given in Fig. 5.19. Within the first 1 cm of the interaction region, the pump pulse transfers significant amount of energy into the SH, while some nonlinear phase shift is accumulated in itself too. Now the SH signal is strong enough that significant back conversion can modify the pump pulse shape. Because of the temporal frequency chirp of the pump pulse resulted from the 'NPM', different pump frequency components are separated in time. Therefore, due to the GVM effect, the 'tail' of the pump has stronger interactions with the SH pulse. This may generate a second hump in the pump pulse and cause a nonuniform spectral distortion in the pump spectrum. The nonuniform phase mismatch distribution seem to be able to result in somewhat similar results. However, because of the relatively small estimated magnitude of this distribution based on the measured SHG spectrum, it probably plays a relatively minor role in causing the spectral and temporal distortion of the pump pulses.

For most materials, their SPM n_2's are positive and much smaller than what we assumed in the simulation [32], except in the presence of nonlinear absorptions. Thus, our additional 'NPM' and its potential physical explanation need some further discussions. We believe the origin of this term may come from a cascaded $\chi^{(2)}$ process.

There had been a significant amount of research, especially theoretical research, on the cascaded $\chi^{(2)}$ from parametric processes [84]. It was realized that the cascaded nonlinear phase shift could replace the $\chi^{(3)}$ process and lead to interesting applications, like all-optical switching [85] and pulse compression [86]. The equations similar to what we study here (Eq. 5.1 and 5.2) also govern the problems of spatial and temporal solitons under a different parameter range, where significant GVD is present, and their solitary solutions are also theoretically studied in

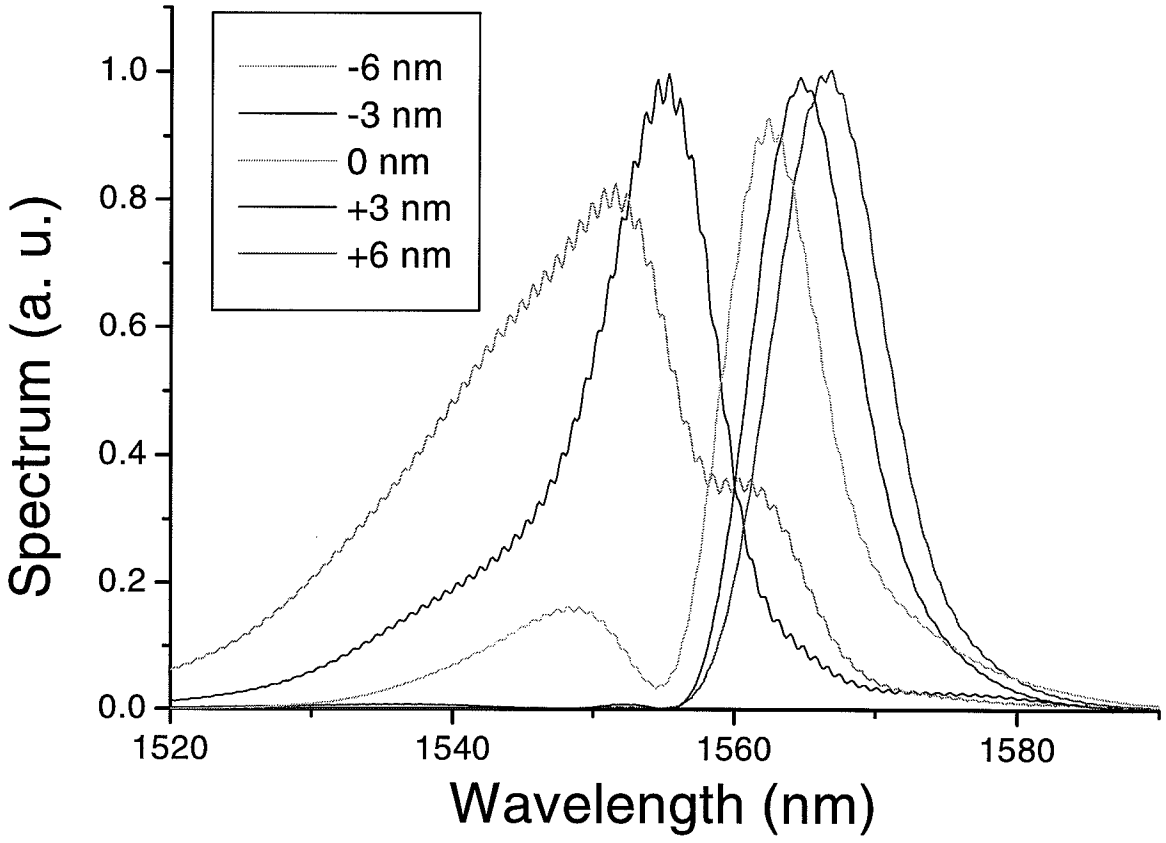

Fig. 5.18. Simulated pump spectrum under large input condition and varied phasematching conditions. The labels show the difference between the input pump center wavelength and the phase matching wavelength.

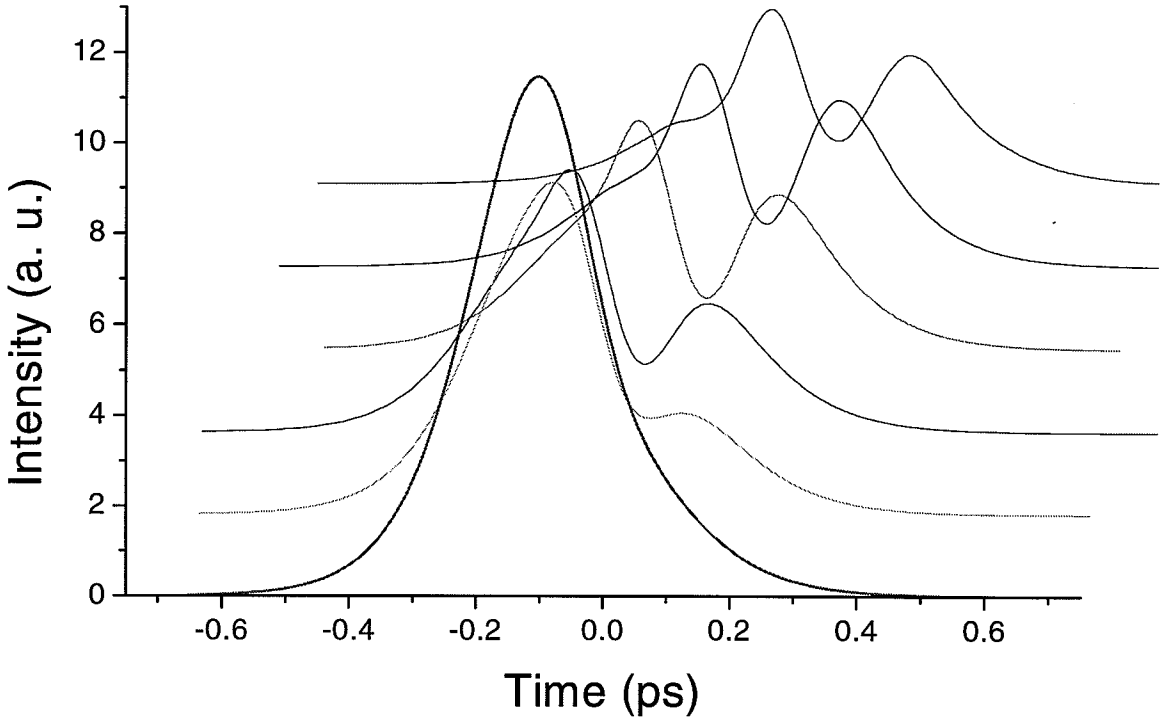

Fig. 5.19. The simulated evolution of the pump pulse shape under 10pJ input power, considering an effective varying phase mismatch and an effective 'NPM' term. Shown are the pulses after every 1 cm, e. g. at the distances of 1 cm , 2 cm, ..., 6 cm.

[84, 92, 93, 94, 95, 96, 97, 98, 99, 85, 86, 87].

It is interesting to note the similarities between the pump pulse shape we measured and the double-hump pulse solution for spatial solitons in the presence of walk-off [98, 99]. In the latter case, a phase jump also exists between the two humps, which bears resemblance to our case.

Though, in some experimental studies [86], GVM, SPM, cascaded $\chi^{(2)}$ and GVD are also considered, the difference between ours and theirs is significant. The parametric process they studied is not phase matched. We are studying a SHG potentially with an 'additional' not-phasematched parametric process, which I believe had not been fully studied before.

Cascaded $\chi^{(2)}$ processes can lead to very large nonlinear phase shifts, compared to the $\chi^{(3)}$ processes [85]. The effective n_2 from SHG processes can be larger than $\sim 10 \times 10^{-12}\ cm^2/W$ for PPLN [85]. Its sign is decided by the phase mismatch, so that it can be easily a negative one depending on the phasematching condition. Under our experimental condition, one potential physical origin of this additional nonlinear phase modulation could come from the interaction between the TM_{00} fundamental mode and other higher order SH modes.

It had been realized that a multi-step $\chi^{(2)}$ cascading could exist, especially in materials like PPLN where the phase matching conditions between other $\chi^{(2)}$ process could be nearly met [100, 101, 102]. It is pointed out that a process that involves third harmonic generation (THG) could result in a nonlinear phase shift that has a I^2 dependence. We experimentally observed the existence of some amount of green light, which was the third harmonic signal generated by a sum-frequency generation (SFG) process between the fundamental and the SH it generated. This process seems to be not exactly phase matched, but its QPM effective phase mismatch could be relatively small, so that cascaded $\chi^{(2)}$ effect could be generated from this effect. Based on the theory given in [100], under the condition that $\Delta k_2 = 0$, e. g. the SHG process is phase matched, the estimated $n_{4,eff}$ could be roughly in the order of $10^{-28}/\Delta k_3$ m^4/W^2 (using PPLN numbers), where the Δk_3 is the phase mismatch of the THG

process. In our simulation, an effective n_4 around 2×10^{-31} can be used to generate the similar simulation results shown above. This number seems to be within reasonable range if Δk_3 is as large as several hundreds to thousands.

Our above etimations over-simplifies the problem by approximating the cascaded $\chi^{(2)}$ effects with an fixed effective n_2 or n_4, as the effective n_2 or n_4 has an intensity dependence [85]. Also our pulsed input may violate the CW-input assumption that had been used in those analysis of n_2 or n_4. However, the estimation shows the possibility of explaining the phenomena by considering the cascaded $\chi^{(2)}$ effects.

A more accurate modeling of both the SHG and the cascaded $\chi^{(2)}$ effect involves a set of 3 coupled equations. Due to our limited knowledge of the related parameters of the potential cascaded $\chi^{(2)}$ process and simulation resources, it is beyond the scope of this dissertation. Such issues may lead to some errors in our simulation, and prevent us from quantitatively matching all experimental results using a fixed set of simulation parameters. Nevertheless, it is clear that our simulation matches the results very well qualitatively, and provide us important insight into the physical phenomena related to the SHG process.

As a conclusion, as we had investigated the high-power femtosecond SHG under large GVM conditions. We decided that the potential culprit for the saturated SHG conversion efficiency of $\sim$ 60 % may be a nonuniform phase mismatch vectors along the waveguide and a nonlinear spectral phase shift.

If our previous conclusions are correct, we can manage to control these effects to get higher SHG efficiency under high power conditions. The temperature variation problem can be solved by using better oven design. The waveguide made with a more uniform structure would also help the efficiency. If the nonlinear phase shift does come from a cascaded $\chi^{(2)}$ process, the PPLN design can be modified slightly, so that the process can be prevented.

6. SUMMARY

As a conclusion, in this dissertation a few nonlinear optical phenomena are studied experimentally and theoretically, with the goal of realizing all-optical waveform recognition in a ultrashort pulse CDMA scenario. Ultrafast optics techniques, involving generation, transmission and detection of femtosecond pulses, are used in these studies. The two-photon absorption waveguide nonlinear optical thresholding scheme demonstrated the pulseshape dependence of the photocurrents and showed a simple way to implement MAI suppression. The optical spectral correlation scheme based on second harmonic generation in long nonlinear crystals show, by far, the best MAI suppression ratio and lowest power requirement. The extensive study of the high power SHG of femtosecond pulses in long PPLN waveguides revealed some interesting physical phenomena that had not been explored before.

Although my studies on these nonlinear device had been focused on their communication applications, it is noted that the results may also have interesting implications in fundamental science areas, like nonlinear optics and coherent controls [103].

LIST OF REFERENCES

[1] A. A. Hassan, J. E. Hershey, and G. J. Saulnier. *Perspectives in spread spectrum.* Kluwer Academic Publishers, Norwell, MA, USA, 1998.

[2] D. D. Sampson, G. J. Pendock, and R. A. Griffin. Photonic code-division multiple-access communications. *Fiber Integr. Opt.*, 16:129–157, 1997.

[3] J. A. Salehi, A. M. Weiner, and J. P. Heritage. Coherent ultrashort light pulse code-division multiple access communication systems. *J. of Lightwave Tech.*, 8(3):478–491, Mar 1990.

[4] M. Kavehrad and D. Zaccarin. Optical code-division-multiplexed systems based on spectral encoding of noncoherent sources. *J. of Lightwave Tech.*, 13(3):534–545, Mar 1995.

[5] A. Grunnet-Jepsen, A. E. Johnson, E. S. Maniloff, T. W. Mossberg, M. J. Munroe, and J. N. Sweetser. Demonstration of all-fiber sparse lightwave CDMA based on temporal phase encoding. *IEEE Photon. Technol. Lett.*, 11(10):1283–1285, Oct 1999.

[6] N. Wada and K.-I. Kitayama. A 10 Gb/s optical code division multiplexing using 8-chip optical bipolar code and coherent detection. *J. of Lightwave Tech.*, 17(10):1758–1765, Oct 1999.

[7] H. X. C. Feng, A. J. Mendez, J. P. Heritage, and W. J. Lennon. Effects of optical layer impairments on 2.5 Gb/s optical CDMA transmission. *Optics Express*, 7(1):2–9, Jul 2000.

[8] C. C. Chang, H. P. Sardesai, and A. M. Weiner. Code-division multiple-access encoding and decoding of femtosecond optical pulses over a 2.5-km fiber link. *IEEE Photon. Technol. Lett.*, 10(1):171–173, Jan 1998.

[9] A. Baltuska, Z. Wei, M. S. Pshenichnikov, and D. A. Wiersma. Optical pulse compression to 5 fs at a 1-MHz repetition rate. *Opt. Lett.*, 22(2):102–104, Jan 1997.

[10] R. Mellish, S. V. Chernikov, P. M. W. French, and J. E. Taylor. All-solid-state compact high repetition rate modelocked Cr^{4+}-YAG laser. *Electron. Lett.*, 34(6):552–553, Mar 1998.

[11] G. J. Valentine, J. M. Hopkins, P. Lozaalvarez, G. T. Kennedy, W. Sibbett, D. Burns, and A. Valster. Ultralow-pump-threshold, femtosecond $Cr^{3+}LiSRaLF_6$ laser pumped by a single narrow-stripe AlGaInP laser diode. *Opt. Lett.*, 22(21):1639–1641, Nov 1997.

[12] S. Kawanishi, H. Takara, T. Morioka, O. Kamatani, K. Takiguchi, T. Kitoh, and M. Saruwatari. 400 Gbit/s TDM transmission of 0.98 ps pulses over 40 km employing dispersion slope compensation. In *Conference on Optical Fiber Communication*, volume 2, pages 423–426, 1996.

[13] C. C. Chang and A. M. Weiner. Fiber transmission for sub-500-fs pulses using a dispersion-compensating fiber. *IEEE J. Quantum Electron.*, 33(9):1455–1464, Sep 1997.

[14] L. Gruner-Nielsen, S. N. Knudsen, B. Edvold, T. Veng, D. Magnussen, C. C. Larsen, and H. Damsgaard. Dispersion compensating fibers. *Optical Fiber Technology*, 6(2):164–180, Apr 2000.

[15] C. C. Chang, H. P. Sardesai, and A. M. Weiner. Dispersion-free fiber transmission for femtosecond pulses by use of a dispersion-compensating fiber and a programmable pulse shaper. *Opt. Lett.*, 23(4):283–285, Feb 1998.

[16] S. Shen and A. M. Weiner. Complete dispersion compensation for 400-fs pulse transmission over 10-km fiber link using dispersion compensating fiber and spectral phase equalizer. *IEEE Photon. Technol. Lett.*, 11(7):827–829, Jul 1999.

[17] M. D. Pelusi, X. Wang, F. Futami, K. Kikuchi, and A. Suzuki. Fourth-order dispersion compensation for 250-fs pulse transmission over 139-km optical fiber. *IEEE Photon. Technol. Lett.*, 12(7):795–797, Jul 2000.

[18] A. M. Weiner, J. P. Heritage, and E. M. Kirschner. High-resolution femtosecond pulse shaping. *J. Opt. Soc. Am. B*, 5(8):1563–1572, Aug 1988.

[19] H. P. Sardesai, C. C. Chang, and A. M. Weiner. A femtosecond code-division multiple-access communication system test bed. *J. of Lightwave Tech.*, 16(11):1953–1964, Nov 1998.

[20] H. Tsuda, H. Takenouchi, T. Ishii, K. Okamoto, T. Goh, K. Sato, A. Hirano, T. Kurokawa, and C. Amano. Spectral encoding and decoding of 10 Gbit/s femtosecond pulses using high resolution arrayed-waveguide grating. *Electron. Lett.*, 35(14):1186–1188, Jul 1999.

[21] A. Grunnet-Jepsen, A. E. Johnson, E. S. Maniloff, T. W. Mossberg, M. J. Munroe, and J. N. Sweetser. Fibre Bragg grating based spectral encoder/decoder for lightwave CDMA. *Electron. Lett.*, 35(13):1096–1097, Jun 1999.

[22] A. Grunnet-Jepsen, A. E. Johnson, E. S. Maniloff, T. W. Mossberg, M. J. Munroe, and J. N. Sweetser. Spectral phase encoding and decoding using fiber Bragg gratings. In *Conference on Optical Fiber Communication*, page 3, 2000.

[23] P. C. Chou, H. A. Haus, and J. F. Brennan. Reconfigurable time-domain spectral shaping of an optical pulse stretched by a fiber Bragg grating. *Opt. Lett.*, 25(8):524–526, Apr 2000.

[24] H. P. Sardesai and A. M. Weiner. Nonlinear fibre-optic receiver for ultrashort pulse code division multiple access communications. *Electron. Lett.*, 33(7):610–611, Mar 1997.

[25] H. Tsuda, K. Okamoto, T. Ishii, K. Naganuma, Y. Inoue, H. Takenouchi, and T. Kurokawa. Second- and third-order dispersion compensator using a arrayed-waveguide grating. *IEEE Photon. Technol. Lett.*, 11(5):569–571, May 1999.

[26] H. Tsuda, H. Takenouchi, A. Hirano, T. Kurokawa, and K. Okamoto. Performance analysis of a dispersion compensator using arrayed-waveguide gratings. *J. of Lightwave Tech.*, 18(8):1139–1147, Aug 2000.

[27] D. Cotter, J. K. Lucek, M. Shabeer, K. Smith, D. C. Rogers, D. Nesser, and P. Gunning. Self-routing of 100 Gbit/s packets using 6 bit 'keyword' address recognition. *Electron. Lett.*, 31(25):2201–2202, Dec 1995.

[28] X. A. Shen and R. Kachru. Optical header recognition by spectroholographic filtering. *Opt. Lett.*, 20(24):2508–2510, Dec 1995.

[29] S. Kawanishi. Ultrahigh-speed optical time-division-multiplexed transmission technology based on optical signal processing. *IEEE J. Quantum Electron.*, 34(11):2064–2079, Nov 1998.

[30] A. Villeneuve, C. C. Yang, G. I. Stegeman, C. N. Ironside, G. S. Celsi, and R. M. Osgood. Nonlinear absorption in a GaAs waveguide just above half the bandgap. *IEEE J. Quantum Electron.*, 30(5):1172–1175, May 1994.

[31] A. Villeneuve, C. C. Yang, G. I. Stegeman, C.-H. Lin, and H.-H. Lin. Nonlinear refractive-index and two photon-absorption near half the band gap in AlGaAs. *Appl. Phys. Lett.*, 62(20):2465–2467, May 1993.

[32] M. Sheik-Bahae, D. C. Hutchings, D. J. Hagan, and E. W. Van Stryland. Dispersion of bound electronic nonlinear refraction in solids. *IEEE J. Quantum Electron.*, 27(6):1296–1309, Jun 1991.

[33] V. Mizrahi, K. W. DeLong, G. I. Stegeman, M. A. Saifi, and M. J. Andrejco. Two-photon absorption as a limitation to all-optical switching. *Opt. Lett.*, 14(20):1140–1142, Oct 1989.

[34] J. S. Aitchison, Y. Silberberg, A. M. Weiner, D. E. Leaird, M. K. Oliver, J. L. Jackel, E. M. Vogel, and P. W. E. Smith. Spatial optical solitons in planar glass waveguides. *J. Opt. Soc. Am. B*, 8(6):1290–1297, Jun 1991.

[35] Y. Takagi, T. Kobayashi, K. Yoshihara, and S. Imamura. Multiple- and single-shot autocorrelator based on two-photon conductivity in semiconductors. *Opt. Lett.*, 17(9):658–660, May 1992.

[36] F. R. Laughton, J. H. Marsh, D. A. Barrow, and E. L. Portnoi. The two-photon absorption semiconductor waveguide autocorrelator. *IEEE J. Quantum Electron.*, 30(3):838–844, Mar 1994.

[37] M. M. Karkhanehchi, C. J. Hamilton, and J. H. Marsh. Autocorrelation measurements of modelocked Nd:YLF laser pulses using two-photon absorption waveguide autocorrelator. *IEEE Photon. Technol. Lett.*, 9(5):645–647, May 1997.

[38] H. K. Tsang, L. Y. Chan, J. B. D. Soole, H. P. LeBlanc, M. A. Koza, and R. Bhat. High sensitivity autocorrelation using two-photon absorption in InGaAsP waveguides. *Electron. Lett.*, 31(20):1773–1775, Sep 1995.

[39] J. K. Ranka, A. L. Gaeta, A. Baltuska, M. S. Pshenichnikov, and D. A. Wiersma. Autocorrelation measurement of 6-fs pulses based on the two-photon-induced photocurrent in a GaAsP photodiode. *Opt. Lett.*, 22(17):1344–1346, Sep 1997.

[40] D. T. Reid, M. Padgett, C. Mcgowan, W. E. Sleat, and W. Sibbett. Light-emitting diodes as measurement devices for femtosecond laser pulses. *Opt. Lett.*, 22(4):233–235, Feb 1997.

[41] W. Rudolph, M. Sheik-Bahae, A. Bernstein, and L. F. Lester. Femtosecond autocorrelation measurements based on two-photon photoconductivity in ZnSe. *Opt. Lett.*, 22(5):313–315, Mar 1997.

[42] A. M. Streltsov, J. K. Randa, and A. L. Gaeta. Femtosecond ultraviolet autocorrelation measurements based on two-photon conductivity in fused silica. *Opt. Lett.*, 23(10):798–800, May 1998.

[43] L. P. Barry, B. C. Thomsen, J. M. Dudley, and J. D. Harvey. Autocorrelation and ultrafast optical thresholding at 1.5 μm using a commercial InGaAsP 1.3 μm laser diode. *Electron. Lett.*, 34(4):358–360, Feb 1998.

[44] A. M. Weiner. Effect of group velocity mismatch on the measurement of ultrashort optical pulses via second harmonic generation. *IEEE J. Quantum Electron.*, 19(8):1276–1283, Aug 1983.

[45] Z. Zheng, A. M. Weiner, J. H. Marsh, and M. M. Karkhanehchi. Ultrafast optical thresholding based on two-photon absorption GaAs waveguide photodetectors. *IEEE Photon. Technol. Lett.*, 9(4):493–495, Apr 1997.

[46] G. P. Agrawal. *Fiber-optic communication systems.* John Wiley & Sons, Inc., New York, NY, USA, 2nd ed. edition, 1997.

[47] K. Tamura, H. A. Haus, and E. P. Ippen. Self-starting additive pulse modelocking erbium fiber ring laser. *Electron. Lett.*, 28(24):2226–2228, Nov 1992.

[48] A. M. Weiner, D. E. Leaird, J. S. Patel, and II J. R. Wullert. Programmable shaping of femtosecond optical pulses by use of 128-element liquid crystal phase modulator. *IEEE J. Quantum Electron.*, 28(4):908–920, Apr 1992.

[49] M. M. Karkhanehchi, J. H. Marsh, and D. C. Hutchings. Polarization dependence of two-photon absorption in an AlGaAs waveguide autocorrelator. *Appl. Opt.*, 36(30):7799–7801, Oct 1997.

[50] Z. Zheng, S. Shen, H. Sardesai, C. C. Chang, J. H. Marsh, M. M. Karkhanehchi, and A. M. Weiner. Ultrafast two-photon absorption optical thresholding of spectrally coded pulses. *Opt. Comm.*, 167:225–233, Aug 1999.

[51] I. Moerman, P. P. Van Daele, and P. M. Demeester. A review on fabrication technologies for the monolithic integration of tapers with III-V semiconductor devices. *IEEE Select. Topics Quantum Electron.*, 3(6):1308–1320, Dec 1997.

[52] P. A. Franken, A. E. Hill, C. W. Peters, and G. Weinreich. Generation of optical harmonics. *Phys. Rev. Lett.*, 7:118–119, 1961.

[53] W. H. Glenn. Second-harmonic generation by picosecond optical pulses. *IEEE J. Quantum Electron.*, QE-5(6):284–290, 1969.

[54] S. A. Akhmanov, A. P. Sukhorukov, and A. S. Chirkin. Nonstationary phenomena and space-time analogy in nonlinear optics. *Sov. Phys. JETP*, 28(4):748–757, 1969.

[55] G. D. Boyd and D. A. Kleinman. Parametric interaction of focused gaussian light beams. *J. Appl. Phys.*, 39:3597–3639, 1968.

[56] L. E. Myers, R. C. Eckardt, M. M. Fejer, R. L. Byer, W. R. Bosenberg, and J. W. Pierce. Quasi-phase-matched optical parametric oscillators in bulk periodically poled $LiNbO_3$. *J. Opt. Soc. Am. B*, 12(11):2102–2115, 1995.

[57] G. Imeshev, M. A. Arbore, M. M. Fejer, A. Galvanauskas, M. Fermann, and D. Harter. Ultrashort-pulse second-harmonic generation with longitudinally nonuniform quasi-phase-matching gratings: pulse compression and shaping. *J. Opt. Soc. Am. B*, 17(2):304–318, Feb 2000.

[58] R. C. Eckardt and J. Reintjes. Phase matching limitations of high efficiency second harmonic generation. *IEEE J. Quantum Electron.*, QE-20(10):1178–1187, Oct 1984.

[59] N. C. Kothari and X. Carlotti. Transient second-harmonic generation: influence of effective group-velocity dispersion. *J. Opt. Soc. Am. B*, 5(4):756–764, Apr 1988.

[60] Z. Zheng and A. M. Weiner. Spectral phase correlation of coded femtosecond pulses by second-harmonic generation in thick nonlinear crystals. *Opt. Lett.*, 25(13):984–986, Jul 2000.

[61] D. Meshulach and Y. Silberberg. Coherent quantum control of multiphoton transitions by shaped ultrashort optical pulses. *Phys. Rev. A*, 60(2):1287–1292, Aug 1999.

[62] A. M. Weiner, A. M. Kan'an, and D. E. Leaird. High-efficiency blue generation by frequency doubling of femtosecond pulses in a thick nonlinear crystal. *Opt. Lett.*, 23(18):1441–1443, Sep 1998.

[63] J. A. Armstrong, N. Bloembergen, J. Ducuing, and P. S. Persan. Interactions between light waves in a nonlinear dielectric. *Phys. Rev.*, 127:1918–1939, 1962.

[64] G. T. Kennedy, D. T. Reid, A. Miller, M. Ebrahimzadeh, H. Karlsson, G. Arvidsson, and F. Laurell. Near- to mid-infrared picosecond optical parametric oscillator based on periodically poled $RbTiOAsO_4$. *Opt. Lett.*, 23(7):503–505, Apr 1998.

[65] S. J. B. Yoo, C. Caneau, R. Bhat, M. A. Koza, A. Rajhel, and N. Antoniades. Wavelength conversion by difference frequency generation in AlGaAs waveguides with periodic domain inversion achieved by wafer bonding. *Appl. Phys. Lett.*, 68(19):2609–2611, 1996.

[66] D. Zheng, L. A. Gordon, Y. S. Wu, R. S. Feigelson, M. M. Fejer, R. L. Byer, and K. L. Vodopyanov. 16-μm infrared generation by difference-frequency mixing in diffusion-bonded-stacked GaAs. *Opt. Lett.*, 23(13):1010–1012, Jul 1998.

[67] M. A. Arbore, O. Marco, and M. M. Fejer. Pulse compression during second-harmonic generation in aperiodic quasi-phase-matching gratings. *Opt. Lett.*, 22(12):865–867, Jun 1997.

[68] R. G. Batchko, D. R. Weise, T. Plettner, G. D. Miller, M. M. Fejer, and R. L. Byer. Continuous-wave 532-nm-pumped singly resonant optical parametric oscillator based on periodically poled lithium niobate. *Opt. Lett.*, 23(3):168–170, Feb 1998.

[69] A. Galvanauskas, A. Hariharan, D. Harter, M. A. Arbore, and M. M. Fejer. High-energy femtosecond pulse amplification in a quasi-phase-matched parametric amplifier. *Opt. Lett.*, 23(3):210–212, Feb 1998.

[70] G. D. Miller, R. G. Batchko, W. M. Tulloch, D. R. Weise, M. M. Fejer, and R. L. Byer. 42% -efficient single-pass cw second-harmonic generation in periodically poled lithium niobate. *Opt. Lett.*, 22(24):1834–1836, Dec 1997.

[71] G. W. Ross, M. Pollnau, P. G. Smith, W. A. Clarkson, P. E. Britton, and D. C. Hanna. Generation of high-power blue light in periodically poled $linbo_3$. *Opt. Lett.*, 23(3):171–173, Feb 1998.

[72] M. H. Chou, J. Hauden, M. A. Arbore, and M. M. Fejer. 1.5-μm-band wavelength conversion based on difference-frequency generation in $LiNbO_3$ waveguides with integrated coupling structures. *Opt. Lett.*, 23(13):1004–1006, Jul 1998.

[73] M. A. Arbore, A. Galvanauskas, D. Harter, M. H. Chou, and M. M. Fejer. Engineerable compression of ultrashort pulses by use of second-harmonic generation in chirped-period-poled lithium niobate. *Opt. Lett.*, 22(17):1341–1343, Sep 1997.

[74] G. Imeshev, A. Galvanauskas, D. Harter, M. A. Arbore, M. Proctor, and M. M. Fejer. Engineerable femtosecond pulse shaping by second-harmonic generation with fourier synthetic quasi-phase-matching gratings. *Opt. Lett.*, 23(11):864–866, Jun 1998.

[75] D. H. Jundt. Temperature-dependent sellmeier equation for the index of refraction, n_e, in congruent lithium niobate. *Opt. Lett.*, 22(20):1553–1555, Oct 1997.

[76] M. M. Wefers and K. A. Nelson. Generation of high-fidelity programmable ultrafast optical waveforms. *Opt. Lett.*, 20(9):1047–1049, May 1995.

[77] M. H. Chou, I. Brener, M. M. Fejer, E. E. Chaban, and S. B. Christman. 1.5-μm-band wavelength conversion based on cascaded second-order nonlinearity in $LiNbO_3$ waveguides. *IEEE Photon. Technol. Lett.*, 11(6):653–655, Jun 1999.

[78] K. R. Parameswaran. *Private communication.* 2000.

[79] L. Wang and A. M. Weiner. Programmable spectral phase coding of an amplified spontaneous emission light source. *Opt. Comm.*, 167:(1-6):211–224, Aug 1999.

[80] M. Harwit and N. J. A. Sloane. *Hadamard transform optics.* Academic Press, New York, NY, USA, 1979.

[81] M. A. Arbore, M. M. Fejer, M. E. Fermann, A. Hariharan, A. Galvanauskas, and D. Harter. Frequency doubling of femtosecond erbium-fiber soliton lasers in periodically poled lithium niobate. *Opt. Lett.*, 22(1):13–15, Jan 1997.

[82] I. Brener, M. H. Chou, E. Chaban, K. R. Parameswaran, M. M. Fejer, S. Kosinski, and D. L. Pruitt. Polarization-insensitive wavelength converter based on cascaded nonlinearities in $LiNbO_3$ waveguides. *Electron. Lett.*, 36(1):66–67, Jan 2000.

[83] R. Schiek, Y. Baek, and G. I. Stegeman. Second-harmonic generation and cascaded nonlinearity in titanium-indiffused lithium niobate channel waveguides. *J. Opt. Soc. Am. B*, 15(8):2255–2268, Aug 1998.

[84] C. R. Menyuk, R. Schiek, and L. Torner. Solitary waves due to $\chi^{(2)} : \chi^{(2)}$ cascading. *J. Opt. Soc. Am. B*, 11(12):2434–2443, Dec 1994.

[85] C. N. Ironside, J. S. Aitchison, and J. M. Arnold. An all-optical switch employing the cascaded second-order nonlinear effect. *IEEE J. Quantum Electron.*, 29(10):2650–2654, Oct 1993.

[86] X. Liu, L. J. Qian, and F. Wise. High-energy pulse compression by use of negative phase shifts produced by the cascade $\chi^{(2)} : \chi^{(2)}$ nonlinearity. *Opt. Lett.*, 24(23):1777–1779, Dec 1999.

[87] S. Ashihara, J. Nishina, T. Shimura, and K. Kuroda. Spectrum broadening in femtosecond pulses by cascaded second-order nonlinearities and the influence of temporal walk-off. In *2000 LEOS Annual Meeting Conference Proceeding*, volume 2, pages 517–518, Rio Grande, Puerto Rico, Nov. 2000.

[88] A. M. Weiner. *Private communication.* 1999.

[89] G. P. Agrawal. *Nonlinear fiber optics.* Academic Press, San Diego, CA, USA, 2nd ed. edition, 1995.

[90] C. R. Menyuk. Stability of solitons in birefringent optical fibers. II. Arbitrary amplitudes. *J. Opt. Soc. Am. B*, 5(2):392–402, Feb 1988.

[91] R. DeSalvo, A. A. Said, D. J. Hagan, E. W. Van Stryland, and M. Sheik-Bahae. Infrared to ultraviolet measurements of two-photon absorption and n_2 in wide bandgap solids. *IEEE J. Quantum Electron.*, 27(6):1296–1309, Jun 1991.

[92] L. Torner, D. Mazilu, and D. Mihalache. Walking solitons in quadratic nonlinear media. *Phys. Rev. Lett.*, 77(12):2455–2458, Sep 1996.

[93] K. Gallo, G. Assanto, and G. I. Stegeman. Efficient wavelength shifting over the erbium amplifier bandwidth via cascaded second order processes in lithium niobate waveguides. *Appl. Phys. Lett.*, 71(8):1020–1022, Aug 1997.

[94] C. Conti, S. Trillo, and G. Assanto. Optical gap solitons via second-harmonic generation: Exact solitary solutions. *Phys. Rev. E*, 57(2):R1251–R1254, Feb 1998.

[95] T. Iizuka and Y. S. Kivshar. Optical gap solitons in nonresonant quadratic media. *Phys. Rev. E*, 59(6):7148–7151, Jun 1999.

[96] T. J. Alexander, Y. S. Kivshar, A. V. Buryak, and R. A. Sammut. Optical vortex solitons in parametric wave mixing. *Phys. Rev. E*, 61(2):2042–2049, Feb 2000.

[97] A. G. Kalocsai and J. W. Haus. Nonlinear Schrödinger equation for optical media with quadratic nonlinearity. *Phys. Rev. A*, 49(1):574–585, Jan 1994.

[98] S. Darmanyan, L. Crasovan, and F. Lederer. Double-hump solitary waves in quadratically nonlinear media with loss and gain. *Phys. Rev. E*, 61(3):3267–3269, Mar 2000.

[99] C. Etrich, U. Peschel, F. Lederer, D. Mihalache, and D. Mazilu. Double hump solitary waves in quadratic media with walk-off–domain of existence, stability and decay scenarios. *Opt. and Quantum Electron.*, 30(7-10):881–890, Oct 1998.

[100] K. Koynov and S. Saltiel. Nonlinear phase shift via multistep $\chi^{(2)}$ cascading. *Opt. Comm.*, 152:96–100, 1998.

[101] S. Saltiel, K. Koynov, Y. Deyanova, and Y. S. Kivshar. Nonlinear phase shift resulting from two-color multistep cascading. *J. Opt. Soc. Am. B*, 17(6):959–965, Jun 2000.

[102] S. Saltiel and Y. Deyanova. Polarization switching as a result of cascading of two simultaneously phase matched quadratic processes. *Opt. Lett.*, 24(18):1296–1298, Sep 1999.

[103] Z. Zheng and A. M. Weiner. Coherent control of second harmonic generation using spectrally phase coded femtosecond waveforms. *Chem. Phys.*, (Special Issue):To be published, Jan 2001.

VITA

VITA

Zheng Zheng received his B. Eng degree from Department of Electronic Engineering in Tsinghua University, Beijing, China in 1995, and then he started his Ph. D. study in School of Electrical and Computer Engineering, Purdue University, West Lafayette, IN. He also received his M.S.E.E. from ECE, Purdue Univesity in 1997. His current research interests include optical communications and ultrafast nonlinear optics. Currently, he has coauthored about 12 technical journal articles and conference talks.

He is a student of member of OSA and IEEE/LEOS.

Appendix: Simulation Program

The Matlab programs used in the simulations in Chapter 5 are listed below. There are one main program and several subroutines called by it. Due to the limited width of the page, long lines of commands are cut into several lines of texts in this print-out version.

```
%-------------------------------------------------
%  Title: Calculate the SHG and pump pulse propagation
%
%          Using Split-step Fourier method:
%  Version: 3.1
%  Date: Oct. 15, 00; modified based on shg_main2.m
%  Purpose:
%  Method: The size of the data vector changes as the
%          SH pulse grows longer.
%     Note: All large data vectors are column vectors.
%          The field vector is E
%          From V2.0->2.1: add terms of phase mismatch terms,
%          use shg_walk_5.m
%          also, use shg_par2.m
%-------------------------------------------------

clear;
% Count the simulation time
start_time=clock;

% Load simulation parameters
shg_par2;

% Define the parameters for pulse shapes.

time_step=5e-15;
% Note: T0 is RELATED to the pulsewidth but not
%     the FWHM width.
T0=140e-15;
%Number of initial points
N0=T0/time_step*50;
% convert N0 to a power of 2.
N0=2^(round(log(N0)/log(2))+1)

%Generate the pump pulse
ini_pulse;

% Find out the time walkoff and decide the 'eventual' data size
% Make sure that the time window is at least 2 times the SH
pulsewidth
time_walkoff=DELTA_V*L_crystal;
div_ratio=ceil(2*abs(time_walkoff)/(N0*time_step));
```

```
final_N0=N0*div_ratio;

% Decide the calculation step size
one_large_step=L_crystal/div_ratio;
one_step=one_large_step/2000;

shg_pulse=rand(size(pulse))*max(abs(pulse))*1e-10;

pump_power=zeros(div_ratio*round(one_large_step/one_step),1);
shg_power=pump_power;

pump_pulse_energy0=sum(abs(pulse).^2)*AEFF1
      *epsilon0*C/2*n*time_step;

% Consider the temperature profile
cal_dk;

for zi1=1:div_ratio,

   for zi2=1:round(one_large_step/one_step),
      current_position=
         ((zi1-1)*round(one_large_step/one_step)+zi2-1)*one_step;
      [pulse,shg_pulse]=shg_walk_5(pulse,shg_pulse,
            delta_k((zi1-1)*round(one_large_step/one_step)+zi2),
            N2,ALFA,[BETA2 DELTA_V],N2*0,2*ALFA,[BETA2 0],
            g_SHG,one_step,current_position,time_step);

      % record the current pump and SHG power
     pump_power((zi1-1)*round(one_large_step/one_step)+zi2)=
            sum(abs(pulse).^2)*AEFF1;
      shg_power((zi1-1)*round(one_large_step/one_step)+zi2)=
            sum(abs(shg_pulse).^2)*AEFF2;
   end

   %expand the time scale, when the SH pulse is getting longer
   if zi1==div_ratio
     break;
   else
      clear current_pulse;
      current_pulse=zeros((zi1+1)*N0,1);
      current_pulse(N0+1:(zi1+1)*N0)=pulse;
      clear pulse;
      pulse=current_pulse;
      current_pulse(N0+1:(zi1+1)*N0)=shg_pulse;
      clear shg_pulse;
      shg_pulse=current_pulse;
   end
end

% Plot the result
tmp_start=final_N0/2-500;
```

```
tmp_stop=final_N0/2-200;

figure(1)
plotyy((tmp_start:1:tmp_stop)*time_step,
      abs(pulse(tmp_start:tmp_stop)).^2,(tmp_start:1:tmp_stop)*ti
      me_step,unwrap(angle(pulse(tmp_start:tmp_stop))));
title('pump pulse temporal profile')
figure(2)
plotyy((1:1:final_N0)*time_step,abs(shg_pulse).^2,
      (1:1:final_N0)*time_step,unwrap(angle(shg_pulse)));
title('SHG pulse temporal profile')

pump_spec=fftshift(fft(fftshift(pulse)));
shg_spec=fftshift(fft(fftshift(shg_pulse)));
wavelength_x1=3e8./(3e8/1.56e-6+
      ((1:1:final_N0)-final_N0/2)/(time_step*final_N0)).';
wavelength_x2=3e8./(3e8/0.78e-6+
      ((1:1:final_N0)-final_N0/2)/(time_step*final_N0)).';
figure(3)
tmp_start=final_N0/2-250;
tmp_stop=final_N0/2+250;
tmp_phase1=unwrap(angle(pump_spec(tmp_start:tmp_stop)));
[t_p,t_s]=polyfit((tmp_start:1:tmp_stop)',tmp_phase1,1);
tmp_phase1=tmp_phase1-polyval(t_p,(tmp_start:1:tmp_stop)');
plotyy(wavelength_x1(tmp_start:tmp_stop),
      abs(pump_spec(tmp_start:tmp_stop)).^2,
      wavelength_x1(tmp_start:tmp_stop),tmp_phase1);

tmp_start=final_N0/2-100;
tmp_stop=final_N0/2+100;
figure(4)
tmp_phase2=unwrap(angle(shg_spec(tmp_start:tmp_stop)));
[t_p,t_s]=polyfit((tmp_start:1:tmp_stop)',tmp_phase2,1);
tmp_phase2=tmp_phase2-polyval(t_p,(tmp_start:1:tmp_stop)');
plotyy(wavelength_x2(tmp_start:tmp_stop),
      abs(shg_spec(tmp_start:tmp_stop)).^2,
      wavelength_x2(tmp_start:tmp_stop),tmp_phase2);

% Save results
save tmp pulse shg_pulse pump_power shg_power;
used_time=etime(clock, start_time)/60


%-------------------------------------------------
%  Title: shg_par2.m
%  Version: 2.0
%  Date: 10/15, 00
%  Purpose:  Define the parameters used in SSF program FOR PPLN
%  Note:   Input:
%          Output:  NONE
%          Unite used: LENGTH--METER, POWER-WATT,
%                      TIME-SECOND, FREQUENCY--Hz
```

```
%          For use with shg_walk_3, definition based on thesis
Chap.3
%-------------------------------------------------

% Common constants
C=3e8;
epsilon0=8.854e-12; %Unit: F/m
n=2.14;% LiNbO3, assume n is nearly the same for the pump and SH
WL=1.56e-6;

% LOSS dB/km-> 1/m
ALFA_DB=0.35*1e2; %loss in dB/m
ALFA=log(10^(ALFA_DB/10));
% dispersion, s^2/m
BETA2=100e-27;
% group velocity mismatch (1/vg1-1/vg2) s/m
DELTA_V=-0.37e-9;

% nonlinearity
N2=-2000E-20;% ~-2000e-34 for I^4 assumption;

% Mode sizes
AEFF1=40E-12; % for pump
AEFF2=11E-12; % for SH
% SHG effective overlap area
AEFF3=53.1e-12;

% SHG coupling coefficient
d_eff=16.5e-12*0.5;  % Unit: m/V
g_SHG=4*d_eff*pi/WL/n*sqrt(1/AEFF3);

% Crystal length
L_crystal=6e-2;


%-------------------------------------------------
%  Title: cal_dk.m
%  Version: 1.0
%  Date: Oct. 08, 00
%  Purpose: Define the effective wavevector mismatch
%  Method: The model of the temp distribution is similar
%                    to the one used in JOSAB 98,pp.2255
%  Note:   Input:
%          Output:  NONE
%          Unite used: LENGTH--METER, POWER-WATT,
%                      TIME-SECOND, FREQUENCY--Hz
%-------------------------------------------------

% See the reference for the meaning of these parameters
L_uniform=L_crystal*0.5;
z_Fi=1e-3;
z_ui=L_uniform-z_Fi;
```

```
z_oi=L_uniform+z_Fi;
z_Ni=10e-3;
p_i=4.3;

T_drop=0.009;

% Define the final vector generated
delta_k=pump_power; % size equals the number of steps.

% crystal axis
crystal_z=linspace(0,L_crystal,max(size(delta_k))).';

[zxt1, zxt2]=min(abs(crystal_z-z_ui));
zxt2=zxt2-1;
delta_k(1:zxt2)=T_drop*((z_ui-crystal_z(1:zxt2))/z_Ni).^p_i;
[zxt1, zxt2]=min(abs(crystal_z-z_oi));
zxt2=zxt2+1;
delta_k(zxt2:max(size(delta_k)))=T_drop*
     ((crystal_z(zxt2:max(size(delta_k)))-z_oi)/z_Ni).^p_i;

L_uniform=L_crystal*0.5;
z_Fi=0e-3;
z_ui=L_uniform-z_Fi;
z_oi=L_uniform+z_Fi;
z_Ni=25e-3;
p_i=1.2;

T_drop=0.12;

[zxt1, zxt2]=min(abs(crystal_z-z_ui));
zxt2=zxt2-1;
delta_k(1:zxt2)=delta_k(1:zxt2)
     +T_drop*((z_ui-crystal_z(1:zxt2))/z_Ni).^p_i;
[zxt1, zxt2]=min(abs(crystal_z-z_oi));
zxt2=zxt2+1;
delta_k(zxt2:max(size(delta_k)))=delta_k(zxt2:max(size(delta_k)))
     +T_drop*((crystal_z(zxt2:max(size(delta_k)))-
z_oi)/z_Ni).^p_i;

% curvature is negative
delta_k=-1*delta_k;

%Convert the temp distribution to k-vec distribution
delta_k=2*pi*1.125e2*delta_k+1e-9;

%-------------------------------------------------
%  Title: ini_pulse.m
%  Version: 1.0
%  Date: July 07,99
%  Purpose: Define the initial pulse in SSF program
%  Note:   Input:
%          Output:  NONE
```

```
%          Unite used: LENGTH--METER, POWER-WATT,
%                      TIME-SECOND,FREQUENCY--Hz
%-------------------------------------------------

time_x=(-N0/2:1:N0/2-1).'*time_step;

% Generate the secant hyperbolic pulse with specified energy.
% Modify this following number for different pulse energy
pulse_energy=400e-6/40e6;

pulse=sech(time_x./T0);
pulse=pulse*sqrt(pulse_energy/(sum(abs(pulse).^2)*AEFF1
     *epsilon0*C/2*n*time_step));

%-------------------------------------------------
%  Title: shg_walk_5.m
%               Using Split-step Fourier method: PPLN SHG
%  Version: 3.1
%  Date: Nov. 04, 00
%  Purpose:  Calculate the pulse propagation in ONE STEP
%  Method: consider second order dispersion, nonlinearity
%          and loss, SHG; Use symmetric SSF algorithm.
%  Note: Input:
%               t_dat: field function in time domain, assume
centered.
%               g_shg: SHG coupling coefficient
%               n1 and n2: NL parameter
%               alfa: loss
%               beta2: dispersion parameter
%               step: propagated length
%               dt: the time interval in the time axis for t_dat
%          Output:
%               t_datout: field function in time domain,centered.
%    Note: All vectors like t_dat, t_datout are column vectors.
%
%  Special Note: the unit of the input field now is E
%
%-------------------------------------------------
function [t_datout,t_shg_datout]=shg_walk_5

(t_dat,t_shg_dat,dk,n1,alfa1,beta2_1,n2,alfa2,beta2_2,g_shg,step,
z,dt)
epsilon0=8.854e-12; %Unit: F/m
n=2.14;    % For LiNbO3
WL=1.56e-6;
C=3e8;
AEFF1=40E-12;
AEFF2=11E-12;
AEFF3=53.1e-12;

x_len=max(size(t_dat));
dw=1/dt/x_len*2*pi;
```

```
w=(-1*x_len/2:1:x_len/2-1).'*dw;
w=fftshift(w);

%First estimate the intermediate signal
%Solve the SHG signal first
% Note: Try to save some calculation time

t_shg_datout=fft(fftshift(t_shg_dat));
% Dispersion
t_shg_datout=t_shg_datout.*exp(-j*beta2_2(1)/2*step/2.*w.^2)
      .*exp(-1*alfa2/2*step/2);
% GVM
if beta2_2(2)~=0
   t_shg_datout=t_shg_datout.*exp(-j*beta2_2(2)*step/2.*w);
end
t_shg_datout=fftshift(ifft(t_shg_datout));

% 'NPM' effect;
t_shg_datint=t_shg_datout
   .*exp(-j*n2*2*pi/WL*(abs(t_shg_dat).^2)*epsilon0*C/2*n*step);

% SHG effect
t_shg_datint=t_shg_datint-g_shg*sqrt(AEFF1^2/AEFF2)*(t_dat.^2)
      .*(exp(j*dk*step)-1).*exp(j*dk*z)./dk;

t_shg_datint=fft(fftshift(t_shg_datint));
% Dispersion
t_shg_datint=t_shg_datint.*exp(-j*beta2_2(1)/2*step/2.*w.^2)
      .*exp(-1*alfa2/2*step/2);
% GVM
if beta2_2(2)~=0
   t_shg_datint=t_shg_datint.*exp(-j*beta2_2(2)*step/2.*w);
end

t_shg_datint=fftshift(ifft(t_shg_datint));

%Solve the pump signal first
t_datout=fft(fftshift(t_dat));
% GVD
t_datout=t_datout.*exp(-j*beta2_1(1)/2*step/2.*w.^2)
      .*exp(-1*alfa1/2*step/2);
% GVM
if beta2_1(2)~=0
   t_datout=t_datout.*exp(-j*beta2_1(2)*step/2.*w);
end

t_datout=fftshift(ifft(t_datout));
% NPM effects
t_datint=t_datout
      .*exp(-j*n1*2*pi/WL*(abs(t_dat).^2)*epsilon0*C/2*n*step);

% SHG effect
```

```
t_datint=t_datint+g_shg*sqrt(AEFF2)*t_shg_dat.*conj(t_dat)
      .*(exp(-j*dk*step)-1).*exp(-j*dk*z)./dk;

t_datint=fft(fftshift(t_datint));
% GVD
t_datint=t_datint.*exp(-j*beta2_1(1)/2*step/2.*w.^2)
      .*exp(-1*alfa1/2*step/2);
% GVM
if beta2_1(2)~=0
   t_datint=t_datint.*exp(-j*beta2_1(2)*step/2.*w);
end

t_datint=fftshift(ifft(t_datint));

% Finally solve with the intermediate results
t_datint=(t_datint+t_dat)./2;
t_shg_datint=(t_shg_datint+t_shg_dat)./2;

%Solve the SHG signal first

% Here we also use the intermediate value to increase the
accuracy
t_shg_datout=t_shg_datout
 .*exp(-j*n2*2*pi/WL*(abs(t_shg_datint).^2)*epsilon0*C/2*n*step);

% SHG effect
t_shg_datout=t_shg_datout-g_shg*sqrt(AEFF1^2/AEFF2)*t_datint.^2
      .*(exp(j*dk*step)-1).*exp(j*dk*z)./dk;

t_shg_datout=fft(fftshift(t_shg_datout));
t_shg_datout=t_shg_datout.*exp(-j*beta2_2(1)/2*step/2.*w.^2)
      .*exp(-1*alfa2/2*step/2);
if beta2_2(2)~=0
   t_shg_datout=t_shg_datout.*exp(-j*beta2_2(2)*step/2.*w);
end
t_shg_datout=fftshift(ifft(t_shg_datout));

%Solve the pump signal next

% NPM effect
% Here we also use the intermediate value to increase the
accuracy
t_datout=t_datout.*exp(-j*n1*2*pi/WL*(abs(t_datint).^2)
     *epsilon0*C/2*n*step);
% SHG effect
t_datout=t_datout+g_shg*sqrt(AEFF2)*t_shg_datint.*conj(t_datint)
      .*(exp(-j*dk*step)-1).*exp(-j*dk*z)./dk;

t_datout=fft(fftshift(t_datout));
t_datout=t_datout.*exp(-j*beta2_1(1)/2*step/2.*w.^2)
      .*exp(-1*alfa1/2*step/2);
if beta2_1(2)~=0
```

```
   t_datout=t_datout.*exp(-j*beta2_1(2)*step/2.*w);
end
t_datout=fftshift(ifft(t_datout));
return;
```